UNIVERSIDADE DE BRASÍLIA – UnB
INSTITUTO DE GEOCIÊNCIAS – IG
CURSO DE PÓS-GRADUAÇÃO EM GEOLOGIA

CARACTERIZAÇÃO GEOQUÍMICA E GEOCRONOLÓGICA DO EMBASAMENTO MESOPROTEROZÓICO DA PARTE NORTE DA SERRANIA DE SAN LUCAS (COLÔMBIA)

DISSERTAÇÃO DE MESTRADO Nº 302

Federico Alberto Cuadros Jiménez

Brasília, DF, Setembro de 2012

UNIVERSIDADE DE BRASÍLIA – UnB
INSTITUTO DE GEOCIÊNCIAS – IG
CURSO DE PÓS-GRADUAÇÃO EM GEOLOGIA

CARACTERIZAÇÃO GEOQUÍMICA E GEOCRONOLÓGICA DO EMBASAMENTO MESOPROTEROZÓICO DA PARTE NORTE DA SERRANIA DE SAN LUCAS (COLÔMBIA)

Federico Alberto Cuadros Jiménez

Orientador:
Prof. Dr. Nilson Francisquini Botelho

Banca Examinadora:

Prof. Dr. Nilson Francisquini Botelho (UnB)

Prof. Dr. Massimo Matteini (UnB)

Prof. Dr. Moacir José Buenano Macambira (UFPA)

Brasília, DF, Setembro de 2012

RESUMO

A Serrania de San Lucas (SSL) é o extremo mais setentrional da Cordilheira Central Colombiana e é considerada como parte do Terreno Chibcha, caracterizado por rochas de meio a alto grau do Mesoproterozóico Superior-Neoproterozóico Inferior. Na parte norte da SSL aflora um conjunto de rochas composto por granito-gnaisse e rochas metamáficas que incluem metamonzogabro, anfibolito e granulito retrogradados, intrudidos por um batólito granodiorítico. Altos teores de elementos traço incompatíveis permitem classificar as rochas graníticas gnáissicas na categoria tipo A, enquanto que os padrões nos diagramas multi-elementos indicam uma afinidade com OIB para as rochas metamáficas. No entanto, essas mesmas feições geoquímicas e valores do índice de saturação de alumínio e a razão MgO/TiO_2 no granito-gnaisse sugerem a presença de materiais relacionados a arco e/ou sedimentares na fonte que deu origem aos magmas precursores das rochas félsicas e máficas. Levando em conta essas características e alguns outros exemplos da literatura, estas rochas podem ser relacionadas a um contexto tectônico pós-colisional, tendo sido geradas a partir de magmas com influência de materiais de arco e/ou orogênicos. Análises de U-Pb em zircão sugerem idades de cristalização entre 1.54 e 1.50 Ga para os protólitos do granito-gnaisse e o metamonzogabro. Adicionalmente, valores de $\varepsilon_{Nd}(T)$ entre +2.3 e +4.7 e razões iniciais $^{87}Sr/^{86}Sr$ entre 0.7020 e 0.7037 (este último sendo o caso das rochas metamáficas) sugerem uma origem mantélica para os dois tipos de rochas, as quais possuem um caráter esencialmente juvenil como indicado por valores de T_{DM} entre 1.5 e 1.7 Ga. Uma correlação geoquímica e geocronológica entre as rochas graníticas estudadas e a Suíte Granítica tipo A do Rio Uaupés (~1.52 Ga) na Província Rio Negro do Cráton Amazônico pode ser estabelecida, o que permite inferir um transporte desde o sul para o Terreno Chibcha como indicado por modelos anteriores. Bordas metamórficas em zircões do granito-gnaisse e o metamonzogabro apresentaram idades entre 1180 e 930 Ma consistentes com idades de terrenos metamórficos relacionados no Equador, Venezuela, Perú, México e América Central. Esses terrenos são considerados como parte da margem noroeste de Amazônia durante a sua colisão com Báltica no contexto da Orogenia Grenvilliana/Sveconorueguesa relacionada à conformação final de Rodínia.

Palavras chave: Serrania de San Lucas; Granito Tipo A; Granito Pós-colisional; Rochas Máficas Transicionais; Mesoproterozóico Inferior; Amazônia; Orogenia Grenvilliana/Sveconorueguesa; Terreno Chibcha.

ABSTRACT

The San Lucas Range (SLR) makes up the northernmost end of the Colombian Central Cordillera and is regarded as a part of the Chibcha Terrane, which is characterized by medium- to high-grade Upper Mesoproterozoic-Lower Neoproterozoic rocks. To the north of the SLR, outcrops of granite-gneiss and metamafic rocks including retrograded metamonzogabbro, amphibolite and granulite can be found, all those units being intruded by a granodioritic batholith. High amounts of incompatible trace elements allow classifying the granite-gneissic rocks into the A-type category, while the multi-element diagram patterns of the metamafic rocks indicate an affinity with OIB. However, the same geochemical proxies and values of the aluminum saturation index and MgO/TiO_2 ratios in the granite-gneiss suggest the presence of arc-related/sedimentary materials within the source from which the precursor magmas of both the felsic and mafic rocks were originated. Taking into account these features and some other examples within the literature, these rocks might be related to a post-collisional context, having been generated from magmas influenced by arc-related and/or orogenic components. U-Pb zircon geochronology suggests crystallization ages between 1.54 and 1.50 Ga for the protoliths of the granite-gneiss and the metamonzogabbro. Furthermore, values of $\varepsilon_{Nd}(T)$ between +2.3 and +4.7 and $^{87}Sr/^{86}Sr$ initial ratios from 0.7020 to 0.7037 (the latter being the case of the metamafic rocks) suggest a mantle origin for both rock types, which display an essentially juvenile nature as indicated by values of T_{DM} between 1.5 and 1.7 Ga. A geochemical and geochronological correlation between the studied granitic rocks and the A-type Rio Uaupés Granitic Suite (~1.52 Ga) in the Rio Negro Province of the Amazonian Craton can be established, thus constraining a provenance from southern latitudes for the Chibcha Terrane as stated by earlier models. Metamorphic rims of zircons from both the granite-gneiss and the metamonzogabro yielded ages between 1180 and 930 Ma, which are consistent with ages of related metamorphic terranes in Ecuador, Venezuela, Perú, México and Middle America. These terranes are regarded as part of the northwestern border of Amazonia during its collision with Baltica in the context of the Grenvillian/Sveconorwegian Orogeny related to the final assembly of Rodinia.

Keywords: San Lucas Range; A-type Granite; Post-collisional Granite; Transitional Mafic Rocks; Early Mesoproterozoic; Amazonia; Grenvillian/Sveconorwegian orogeny; Chibcha Terrane.

RESUMEN

La Serranía de San Lucas (SSL) constituye el extremo más septentrional de la Cordillera Central Colombiana y es considerada como parte del Terreno Chibcha, caracterizado por rocas de medio a alto grado del Mesoproterozoico Superior-Neoproterozoico Inferior. En la parte norte de la SSL aflora un conjunto de rocas compuesto por gneiss granítico y rocas metamáficas incluyendo metamonzogabro, anfibolita y granulita retrogradadas, intruídas por un batolito granodiorítico. Altos contenidos de elementos traza incompatibles permiten clasificar las rocas graníticas dentro de la categoría tipo A, mientras que los patrones de diagramas multielementos indican una afinidad con OIB para las rocas metamáficas. No obstante, esas mismas características geoquímicas y valores del índice de saturación de aluminio y la razón MgO/TiO_2 en el gneiss granítico sugieren la presencia de materiales de arco y/o sedimentarios en la fuente que dió origen a los magmas precursores de las rocas félsicas y máficas. Teniendo en cuenta esas características y algunos ejemplos de la literatura, estas rocas pueden ser relacionadas a un contexto tectónico post-colisional, habiendo sido generadas a partir de magmas con influencia de componentes de arco y/o orogénicos. Análisis de U-Pb en zircón sugieren edades de cristalización entre 1.54 y 1.50 Ga para los protolitos del gneiss granítico y el metamonzogabro. Adicionalmente, valores de $\varepsilon_{Nd}(T)$ entre +2.3 y +4.7 y razones iniciales $^{87}Sr/^{86}Sr$ entre 0.7020 y 0.7037 (siendo este último el caso de las rocas metamáficas) sugieren un origen mantélico para ambos tipos de rocas, las cuales poseen un carácter esencialmente juvenil según valores de T_{DM} entre 1.5 y 1.7 Ga. Una correlación geoquímica y geocronológica entre las rocas graníticas estudiadas y la Suite Granítica tipo A del Río Uaupés (~1.52 Ga) en la Provincia Río Negro del Craton Amazónico puede ser establecida, lo que permite inferir un transporte desde el sur para el Terreno Chibcha como había sido ya indicado por modelos anteriores. Bordes metamórficos en zircones del gneiss granítico y el metamonzogabro proporcionaron edades entre 1180 y 930 Ma, las cuales son consistentes con edades de terrenos metamórficos relacionados en Ecuador, Venezuela, Perú, México y Centroamérica. Estos terrenos son considerados como parte de la margen noroeste de Amazonia durante su colisión con Báltica en el contexto de la Orogenia Grenvilliana/Sveconoruega relacionada a la conformación final de Rodinia.

Palabras clave: Serranía de San Lucas; Granito Tipo A; Granito Post-colisional; Rocas Máficas Transicionales; Mesoproterozoico Inferior; Amazonia; Orogenia Grenvilliana/Sveconoruega; Terreno Chibcha.

SUMÁRIO

ÍNDICE DE FIGURAS

ÍNDICE DE TABELAS

CAPÍTULO 1: INTRODUÇÃO

1.1. APRESENTAÇÃO

A serrania de San Lucas (SSL) localiza-se no extremo mais setentrional da Cordilheira Central da Colômbia, no limite entre os vales médio e inferior do rio Magdalena, na margem oeste do mesmo. A SSL tem sido reconhecida por habitantes locais e algumas empresas de mineração nacionais e internacionais como um importante prospecto de mineralizações de ouro e prata, com as primeiras ocorrendo tanto na forma de veios hidrotermais quanto em depósitos aluviais. Também é um dos lugares chave onde o embasamento do Terreno Chibcha pode ser observado diretamente (Restrepo & Toussaint, 1988; Toussaint & Restrepo, 1996; Ordóñez-Carmona *et al*., 2006). Apesar da sua importância econômica e geocientífica, a SSL é ainda uma área virtualmente inexplorada carente de estudos geológicos detalhados, exceto por alguns trabalhos recentes conduzidos por universidades colombianas que tratam temas relacionados com petrografia, geologia estrutural, geoquímica e aspectos relacionados ao minério. Parte da cartografia geológica básica também tem sido melhorada recentemente pelo Serviço Geológico Colombiano (INGEOMINAS). A carência geral de conhecimento geológico detalhado é devida à ausência de infraestrutura civil apropriada que facilite o acesso e à sua instável situação de segurança gerada a partir dos conflitos sociais que ainda existem na região.

Como exemplo, é conhecido que a unidade denominada Gnaisse de San Lucas está longe de ser litologicamente homogênea visto que agrupa vários tipos de rochas metamórficas com diferentes protólitos (*e.g.*, Feininger *et al*., 1973). Porém, esse caráter heterogêneo ainda não foi expresso cartograficamente e a unidade é atualmente mapeada como uma única entidade só ao longo de toda sua extensão. Outro exemplo do escasso conhecimento geológico da região tem a ver com a natureza e origem das suas mineralizações de ouro, para as quais uma classificação clara e um modelo metalogenético quantitativo e robusto ainda não foram propostos.

Este trabalho, embora não dirigido a resolver todos os problemas e incógnitas relacionadas com a geologia da SSL, constitui uma contribuição para o entendimento da geologia e o arcabouço geodinâmico da região, especialmente da sua parte setentrional abrangendo o sul do departamento de Bolívar.

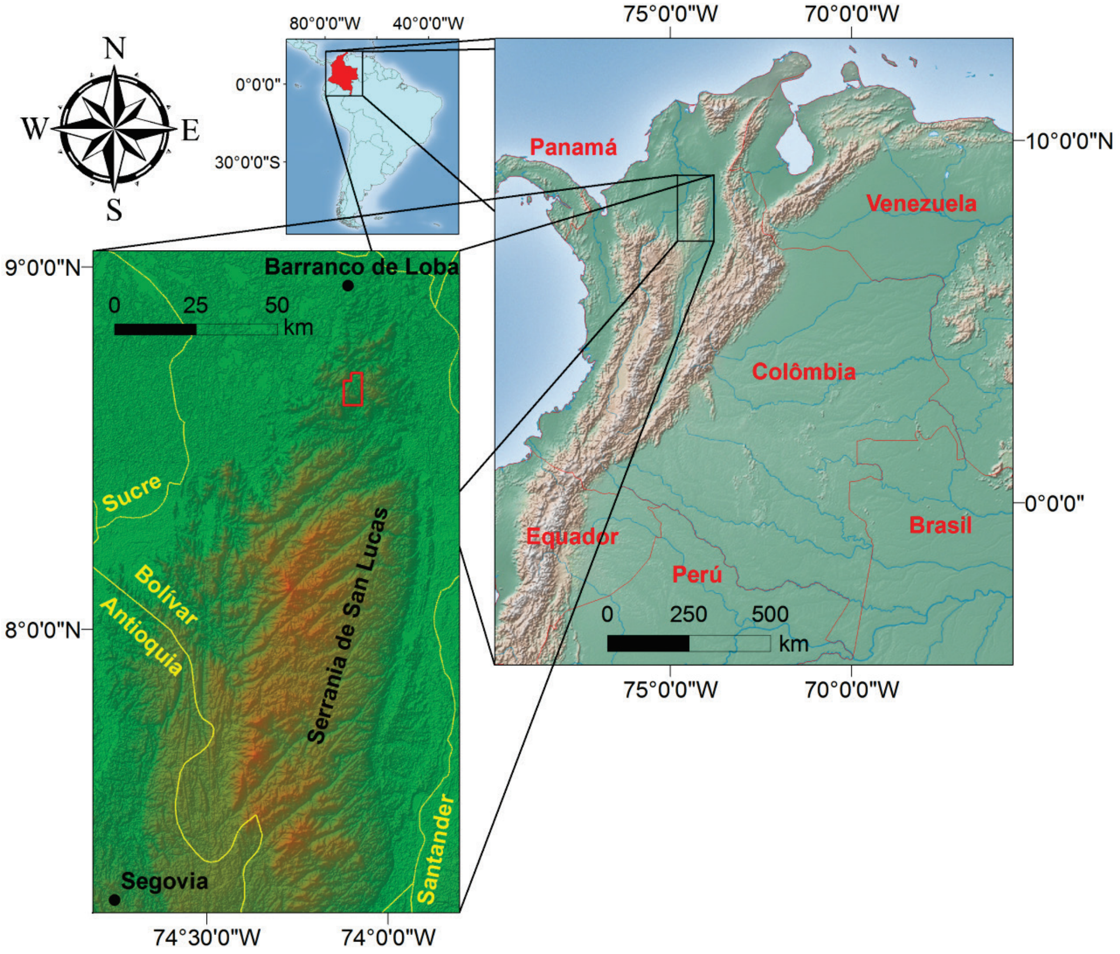

Figura 1 – A área de estudo encontra-se localizada no extremo norte da SSL (retângulo vermelho). A SSL constitui o extremo mais setentrional da Cordilheira Central Colombiana. As linhas amarelas indicam os limites departamentais. Informação geográfica e topográfica tomada de www.naturalearthdata.com e srtm.csi.cgiar.org.

1.2. LOCALIZAÇÃO E ACESSO

A área de estudo encontra-se localizada na Colômbia, no sul do departamento de Bolívar, em jurisdição do corregimento de Pueblito Mejía, ~30 km a sul da zona urbana do município de Barranco de Loba (figura 1). Essa região constitui a parte norte da SSL, a qual por sua vez é a porção mais setentrional da Cordilheira Central Colombiana. Trata-se de uma zona relativamente isolada, de difícil acesso e com estradas em má condição. O acesso desde as principais cidades pode ser conseguido tomando a rodovia principal do Magdalena Meio seguindo a rota Bogotá (ou Medellín)-Barrancabermeja-Aguachica-Pailitas. Em Pailitas, pode continuar-se de carro pela estrada que leva até El Banco, e neste último lugar o rio Magdalena é cruzado de lancha até chegar ao município de Barranco de Loba desde onde se pode chegar por estrada de terra até Pueblito Mejía. Alternativamente, após passar em Aguachica na rodovia do Magdalena Meio, toma-se o desvio que leva até o povoado de Regidor, lugar no qual o rio Magdalena é cruzado de lancha ou de balsa para depois tomar uma estrada de terra que leva diretamente até Pueblito Mejía.

1.3. JUSTIFICATIVA E OBJETIVOS DO TRABALHO

O presente trabalho foi desenvolvido com o interesse de começar a preencher os vazios que existem no conhecimento geológico do extremo setentrional da Cordilheira Central Colombiana. Tradicionalmente, os estudos realizados na região durante a segunda metade do século XX não conseguiam acrescentar o conhecimento geológico além das descrições petrográficas e estratigráficas das unidades que afloram na SSL, deixando sempre de lado as considerações relacionadas com as suas origens e contextos geodinâmicos de geração. Nos anos 90 e na primeira década do século XXI começaram aparecer os primeiros modelos tectônicos modernos para os Andes Colombianos que indicaram a importância da orogenia Grenvilliana na sua evolução geológica (*e.g.*, Toussaint & Restrepo, 1996; Restrepo-Pace *et al*., 1997; Ordóñez-Carmona *et al*., 1999, 2002b, 2006; Cordani *et al*., 2005; Cardona *et al*., 2010a). Este foi um grande avanço, visto que conseguiu articular geologicamente essa parte dos Andes Colombianos junto com o resto da cadeia Andina para a qual foi reconhecida a presença de assinaturas Grenvillianas nos blocos que constituem o seu embasamento (Fuck *et al*., 2008; Ramos, 2009, 2010). Porém, atualmente é difícil enxergar mais para lá da história Neoproterozóica Grenvilliana das Cordilheiras Colombianas, e este trabalho é uma das primeiras tentativas de estabelecer a origem de algumas das unidades que conformam o seu embasamento, e que têm as suas raízes no Mesoproterozóico. Esse novo conhecimento vai contribuir para o refinamento dos atuais modelos de evolução paleocontinental pré-gondwânica.

Por outro lado, a SSL é uma região onde tradicionalmente tem sido reconhecida a presença de mineralizações de ouro de alto teor, sendo que o conhecimento da geologia básica da zona constitui o primeiro passo para encaminhar futuros estudos de pesquisa mineral que permitam identificar e desenvolver projetos de mineração que tragam um avanço econômico para a região e para o país.

Entre os objetivos da pesquisa foi contemplado: 1) fazer uma cartografia geológica a escala de detalhe (1:25000) de uma pequena área do distrito mineiro de Barranco de Loba, especificamente no distrito de Pueblito Mejía; 2) determinar o ambiente tectônico de formação das unidades do embasamento, baseado em análises químicas de elementos maiores, menores e traço e de geoquímica isotópica; e 3) obter idades absolutas por meio de análises geocronológicas para essas unidades e formular modelos conceituais da origem e evolução geológica para a parte setentrional dos Andes Colombianos.

Os resultados do trabalho são apresentados na forma de artigo, que constitui o capítulo 4 e será submetido ao Journal of South American Earth Sciences. Atendendo as normas do programa de Pós-Graduação em Geologia, para dissertações na forma de artigo em inglês, são apresentados, em português, os capítulos de Introdução, Materiais e Métodos e Geologia Regional e um capítulo final com as principais conclusões do trabalho.

CAPÍTULO 2: CONTEXTO GEOLÓGICO REGIONAL

2.1. CONTEXTO ANDINO

A cadeia Andina é um dos principais sistemas de montanhas do mundo, estendendo-se por mais de 8000 km ao longo da margem Pacífica da América do Sul desde Terra do Fogo (Chile e Argentina) até o norte da Colômbia e a Venezuela. Esta faixa é considerada o sistema orogênico gerado pela subducção de crosta oceânica sob uma placa continental mais representativo no presente (Alemán & Ramos, 2000). Gansser (1973) foi pioneiro na subdivisão da cadeia Andina nos segmentos Norte, Central e Sul (figura 2), os quais são diferenciados na base de critérios fisiográficos, litológicos, estruturais, tectônicos, vulcanológicos e sísmicos. Atualmente, é reconhecido que os Andes estão longe de serem gerados por um processo orogênico simples, e que pelo contrário são o resultado de uma complexa interação entre vários fenômenos que incluem colisão, acreção, erosão, extensão, sedimentação, subducção, magmatismo e metamorfismo.

Os Andes do norte, assim como o resto da cadeia, evoluíram começando pela acreção de fragmentos continentais e terrenos à placa sul americana desde o Neoproterozóico, com a grande maioria desses blocos possuindo uma importante assinatura geocronológica Grenvilliana (Fuck *et al*., 2008; Ramos, 2009, 2010). A partir do Mesozóico, esta parte do Andes tem sido caracterizada por eventos metamórficos de baixa temperatura/alta pressão, acreção e obducção de terrenos oceânicos Cretáceos e Paleógenos (Alemán & Ramos, 2000) como resultado de interações com as placas do Caribe e Nazca, gerando uma complexa configuração tectônica que tem influenciado importantes características tais como vulcanismo e sismicidade (figura 3). Isto é expresso por exemplo na terminação da cadeia vulcânica ativa à latitude 4.9ºN e na concentração de hipocentros de tremores profundos nos "ninhos" de Cauca e Bucaramanga nas cordilheiras Colombianas. O primeiro deles é associado à ausência de subducção profunda da microplaca de Coiba causada pelo bloqueio da trincheira sob o segmento Andino setentrional da Colômbia, enquanto que o segundo é associado com quebramento transversal ao mergulho dos segmentos subducidos das placas de Coiba e Caribe (Corredor, 2003; Cortés & Angelier, 2005), embora a colisão entre eles em profundidade também poderia gerar o agrupamento dos sismos observado no ninho de Bucaramanga (Zarifi *et al*., 2007). Adicionalmente, a configuração dos esforços e as

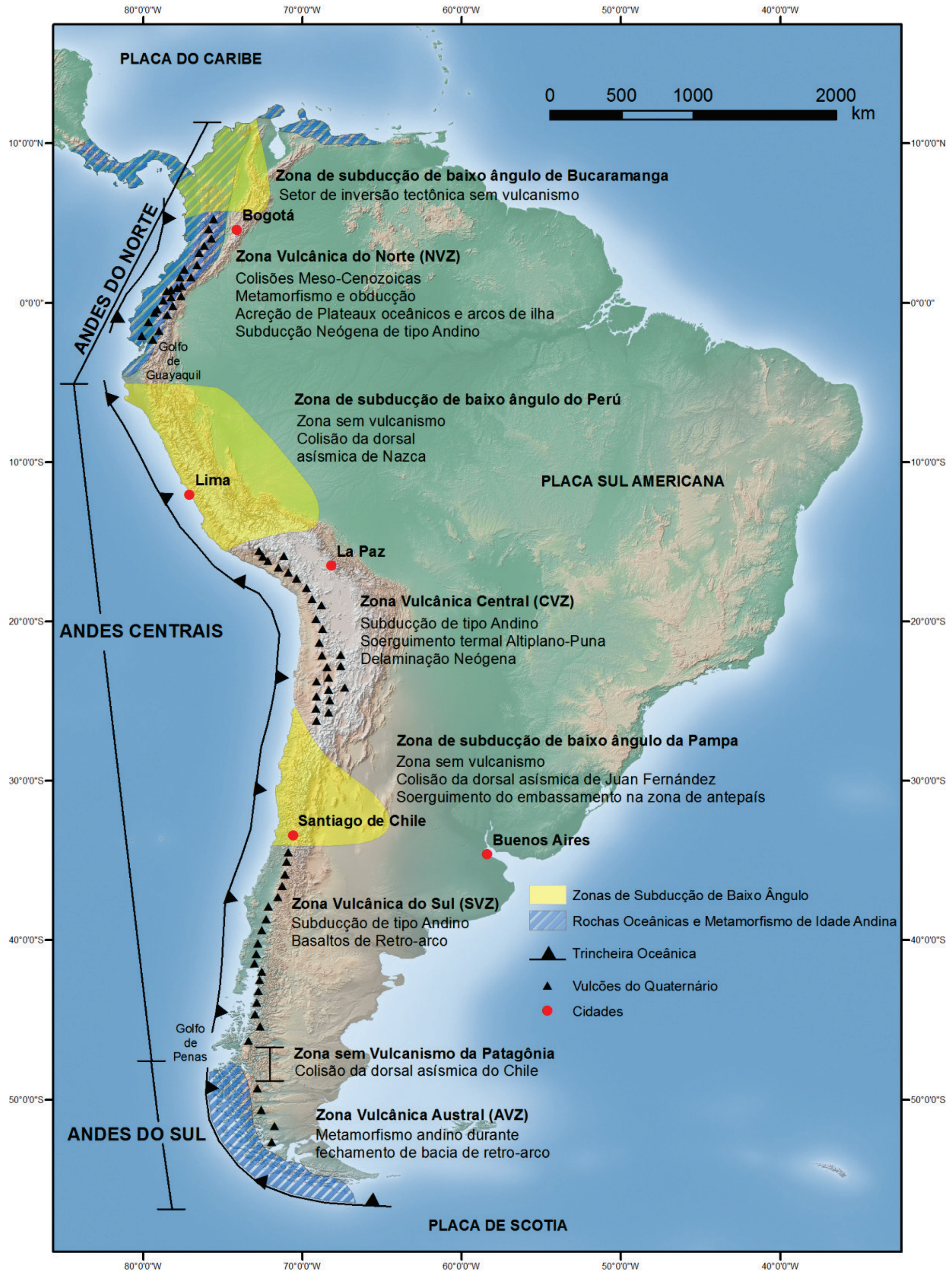

Figura 2 – Principais feições e subdivisões da cadeia Andina. Modificado de Ramos (2009). Informação geográfica tomada de www.naturalearthdata.com.

direções de movimento dos blocos litosféricos desta região que resultam a partir das interações já mencionadas, têm sido traduzidos num trend geral NNE dos principais sistemas de falhas regionais, as quais mostram importantes componentes transcorrentes de movimento. Sistemas de falhas com orientações NW e ENE também

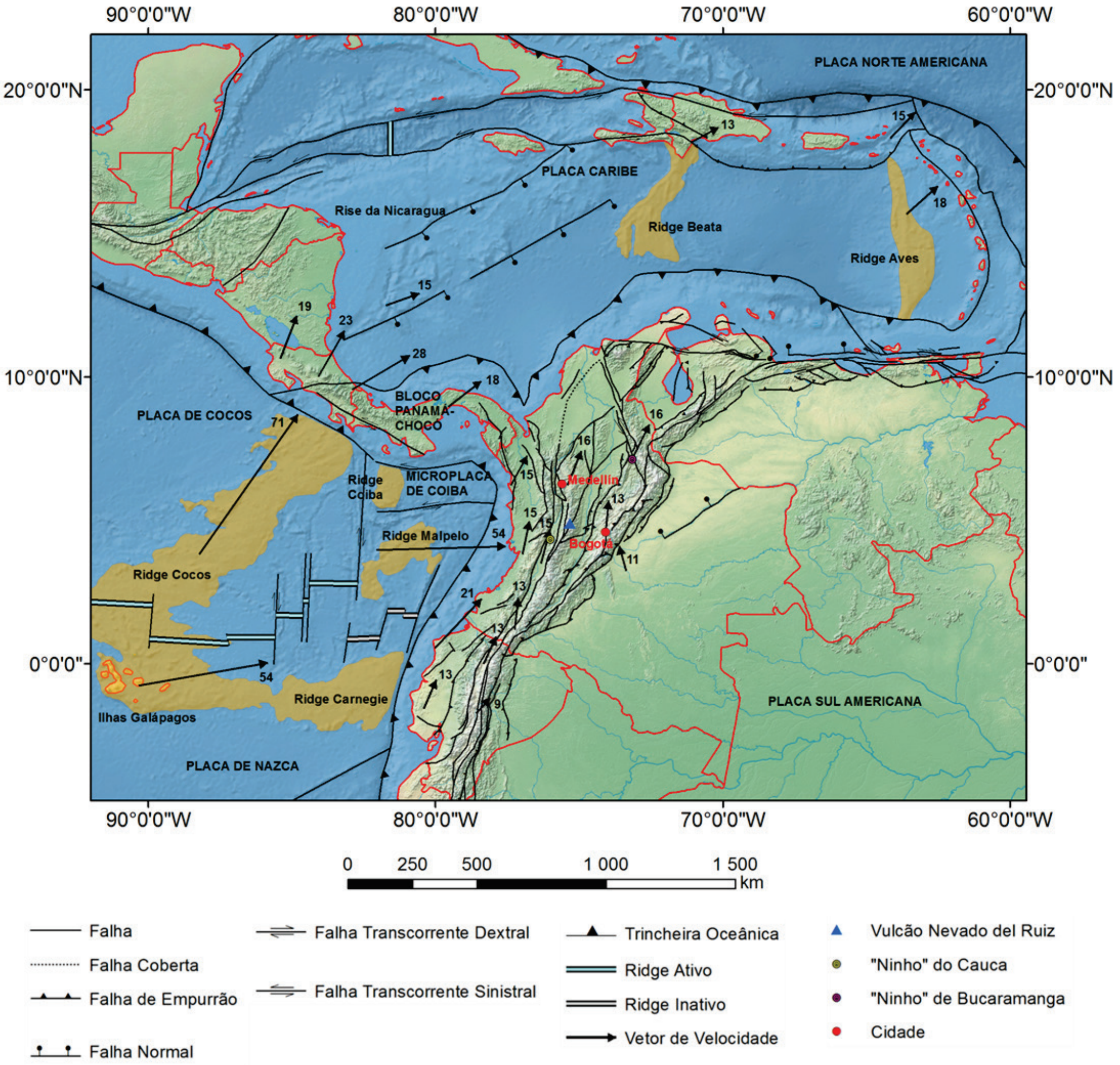

Figura 3 – Configuração tectônica da região Caribe e dos Andes do Norte. Os números dos vetores indicam velocidades em mm/ano medidas em estações de monitoramento por GPS. Não existe atualmente vulcanismo ativo mais para Norte do sistema vulcânico do Nevado Del Ruiz. Modificado de Cortés & Angelier (2005) e INGEOMINAS (2007). Informação geográfica tomada de www.naturalearthdata.com.

existem nos Andes Colombianos, o primeiro deles consistindo em estruturas extensionais pré-Cretáceas reativadas enquanto que o segundo representa estruturas dextrais que resultaram da convergência oblíqua entre a placa de Nazca e os Andes do Norte (Acosta *et al.*, 2007). O movimento geral em direção NE desta parte dos Andes causado por aquela convergência foi responsável pelo começo da zona de subducção do Caribe durante o final do Neógeno (Ramos, 2009).

2.2. SÍNTESE DA GEOLOGÍA DA COLÔMBIA

A história geológica e tectônica da Colômbia é caracterizada dentro do contexto de acreção de terrenos alóctones mencionado anteriormente. Os primeiros modelos

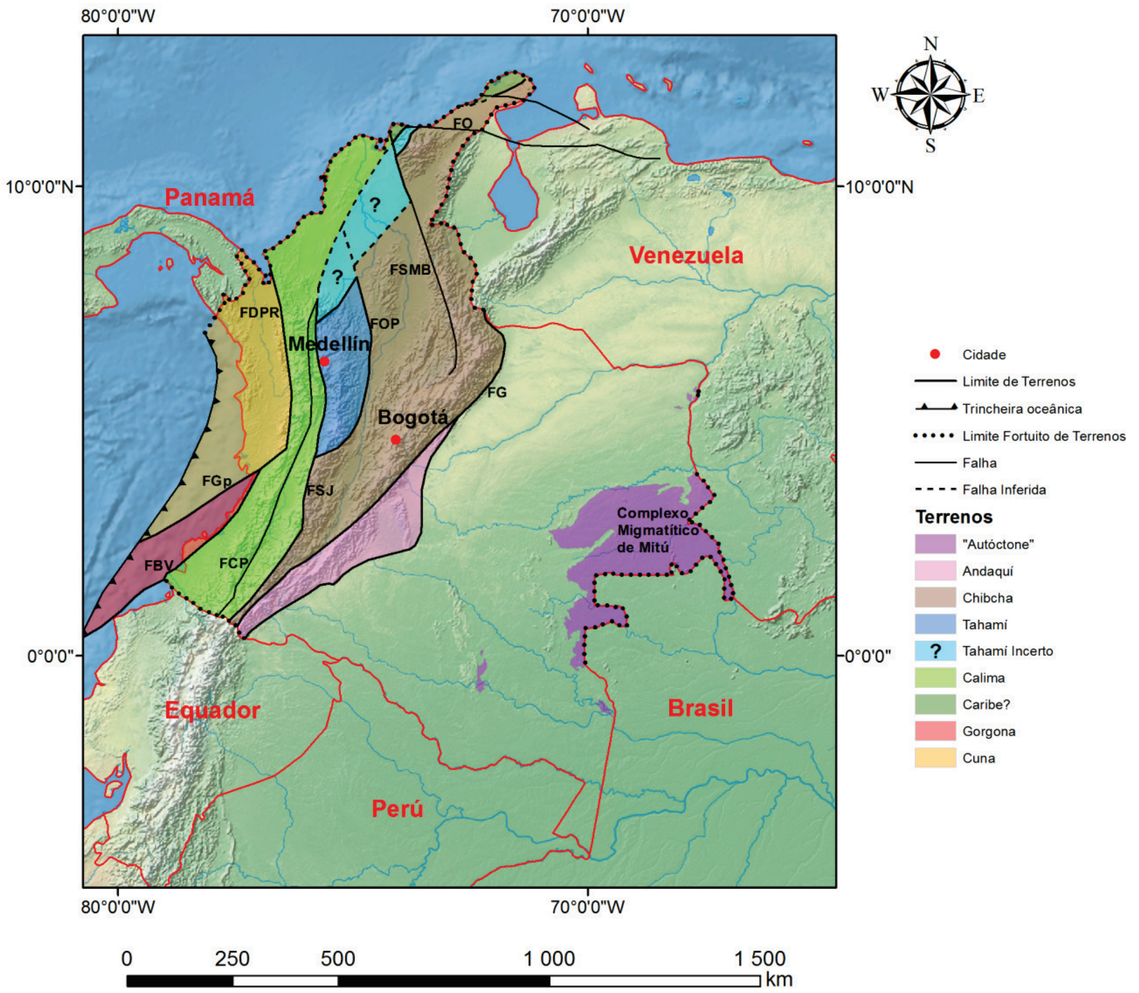

Figura 4 – Terrenos geológicos na Colômbia. **Falhas**: Oca (**FO**), Santa Marta-Bucaramanga (**FSMB**), Otú-Pericos (**FOP**), San Jerónimo (**FSJ**), Guaicáramo (**FG**), Dabeiba-Pueblo Rico (**FDPR**), Cali-Patía (**FCP**), Garrapatas (**FGp**) e Buenaventura (**FBV**). As fronteiras nacionais e linhas do litoral não devem ser percebidas como verdadeiros limites de terrenos, mas foram desenhadas dessa maneira por simplicidade. A faixa entre as falhas Cali-Patía e San Jerónimo corresponde ao Terreno Cauca-Romeral de INGEOMINAS (1985). Os blocos nomeados como "Tahamí Incerto" poderiam estar relacionados ao Terreno Panzenú de Ordóñez-Carmona & Pimentel (2002a). Os blocos "Caribe" do norte da Colômbia são mostrados de maneira independente dada a sua distintiva história geológica relacionada com arcos Cretáceos do Caribe (*e.g.*, Cardona *et al.*, 2010b; Weber *et al.*, 2009; 2010). Os limites do Terreno Gorgona são aqueles indicados por Cediel *et al.* (2003) e Serrano *et al.* (2011). Modificado de Toussaint & Restrepo (1996) e Ordóñez-Carmona *et al.* (2006). Informação geográfica tomada de www.naturalearthdata.com.

abrangentes propostos nesse sentido foram aqueles de INGEOMINAS (1983), McCourt *et al.* (1984) e Restrepo & Toussaint (1988). Este último teve refinamentos posteriores (Toussaint & Restrepo, 1994; 1996) seguindo o conceito de terrenos "suspeitos" sintetizado anteriormente por Coney *et al.* (1980), Jones *et al.* (1983) e Schermer *et al.* (1984). Segundo Toussaint & Restrepo (1988; 1994; 1996), a porção ocidental do território Colombiano consiste em um mosaico de blocos litosféricos que foram acrecionados sucessivamente à margem noroeste do Cráton Amazônico desde o Neoproterozóico (figura 4). A seguir é apresentado um resumo da constituição geológica e história acrecionária de cada terreno com ênfase no Terreno Chibcha, onde a SSL é englobada. Para referências geológicas e geográficas confira a figura 5.

A parte mais oriental da Colômbia encontra-se composta por um "bloco autóctone", que segundo Toussaint & Restrepo (1994; 1996) corresponderia à porção noroeste do Cráton Amazônico coberta quase totalmente por rochas sedimentares do Paleozóico Inferior, Mesozóico e Cenozóico. Os principais afloramentos localizam-se próximos às fronteiras com o Brasil e a Venezuela, definindo a unidade denominada Complexo Migmatítico de Mitú, composto por biotita-gnaisses e migmatitos intrudidos pelo Granito Rapakivi de Parguaza. Essas unidades teriam sido o resultado de eventos tectono-magmáticos ocorridos entre 1.56 e 1.45 Ga que retrabalharam rochas mais antigas do Cráton, com idades entre 1.78 e 1.85 Ga (Priem *et al.*, 1982; Gaudette *et al.*, 1978). Observações similares foram reportadas por Ibáñez-Mejía *et al.* (2011), que descreveram sienogranitos de 1.71-1.77 Ga na região de Araracuara e biotita-anfibólio granitos de 1.53-1.59 Ga da região dos rios Vaupés e Apoporis na Amazônia Colombiana. Unidades vulcânicas, sedimentares e intrusivas mais recentes do Mesoproterozóico, Neoproterozóico e Paleozóico têm sido descritas também na região (*cf.*, Priem *et al.*, 1982; Huguett *et al.*, 1979; Pinson *et al.*, 1962).

O Terreno Andaquí encontra-se representado pelas unidades que afloram no Maciço de Garzón e na Serrania de La Macarena, e que consistem em paragnaisses, migmatitos, granulitos máficos e félsicos, rochas ultramáficas e calci-silicáticas, ortognaisses, mica-xistos e anfibolitos (Trumpy, 1943; Kroonenberg, 1982b; Jiménez-Mejía *et al.*, 2006). Idades de cristalização ígnea e metamorfismo destas rochas variam entre 1280 e 900 Ma, com idades de componentes herdados e T_{DM} Nd entre 1450 e 1970 Ma (Priem *et al.*, 1989; Restrepo-Pace *et al.*, 1997; Cordani *et al.*, 2005; Ibáñez-Mejía *et al.*, 2011). Para este terreno, Ibáñez-Mejía *et al.* (2011) propuseram recentemente um modelo tectônico no qual uma faixa Meso- a Neoproterozóica (o Orógeno de Putumayo) evoluiu começando pelo desenvolvimento de um arco pericratônico fora da margem de Amazônia entre 1.3 e 1.1 Ga, onde os protólitos das unidades metaígneas e metasedimentares deste terreno e outros similares no México teriam sido formados. Posteriormente, um metamorfismo de facies anfibolito e migmatização destas rochas teriam acontecido entre 1.05 e 1.01 Ga gerados como resultado da acreção desses

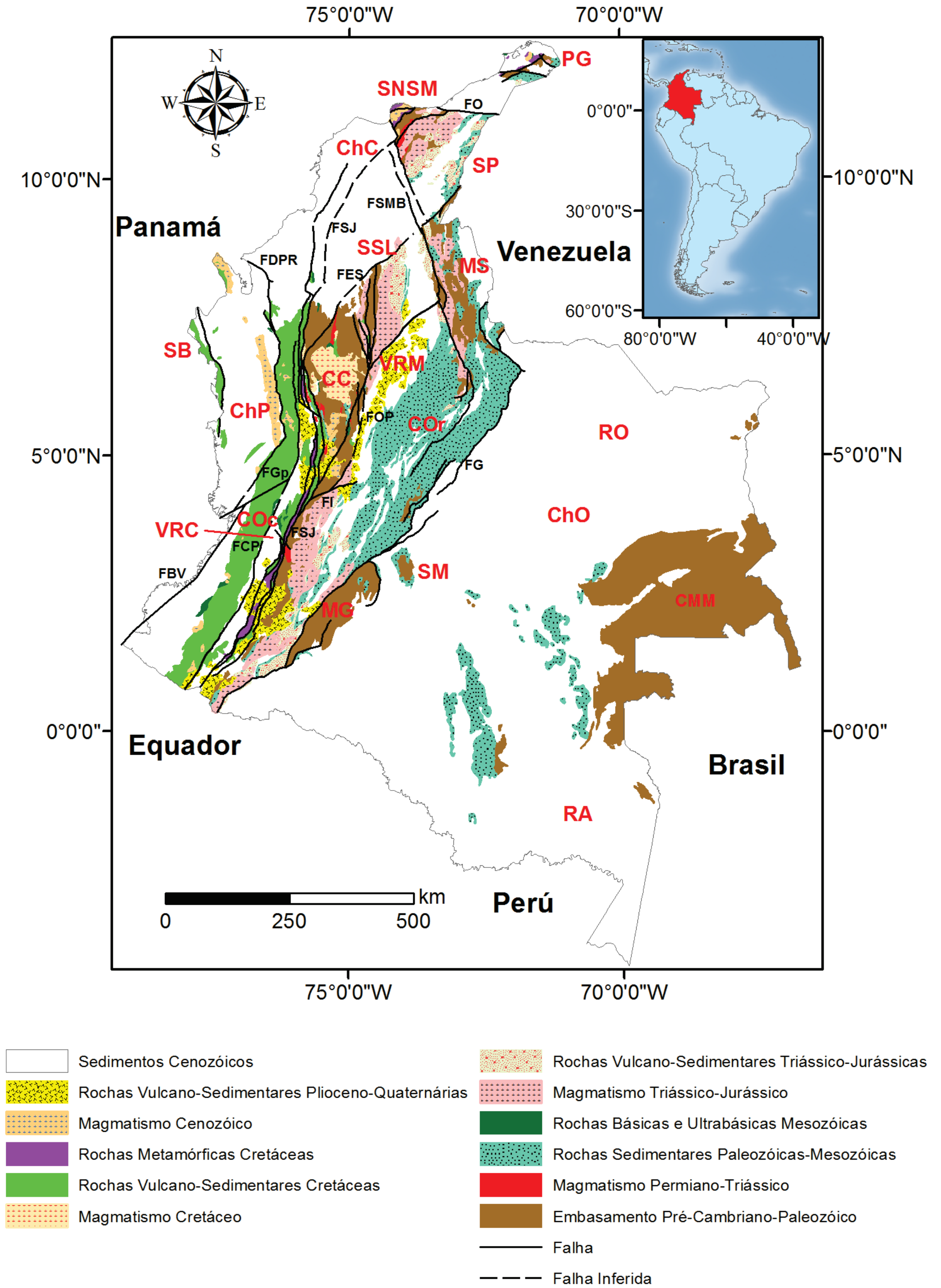

Figura 5 – Mapa geológico simplificado da Colômbia. **Falhas**: Oca (**FO**), Santa Marta-Bucaramanga (**FSMB**), San Jerónimo (**FSJ**), Espíritu Santo (**FES**), Dabeiba-Pueblo Rico (**FDPR**), Otú-Pericos (**FOP**), Garrapatas (**FGp**), Buenaventura (**FBV**), Ibagué (**FI**), Cali-Patía (**FCP**), Guaicáramo (**FG**). **Maciços**: Garzón (**MG**), Santander (**MS**), Complexo Migmatítico de Mitú (**CMM**). **Feições Fisiográficas**: Península da Guajira (**PG**), Serra Nevada de Santa Marta (**SNSM**), Serrania de Perijá (**SP**), Chapadas do Caribe (**ChC**), Serrania de San Lucas (**SSL**), Cordilheira Ocidental (**COc**), Cordilheira Central (**CC**), Cordilheira Oriental (**COr**), Vale do Rio Magdalena (**VRM**), Vale do Rio Cauca (**VRC**), Chapadas do Pacífico (**ChP**), Serrania de Baudó (**SB**), Serrania de La Macarena (**SM**), Chapadas Orientais (**ChO**), Região da Orinoquia (**RO**), Região Amazônica (**RA**). Modificado de INGEOMINAS (2007).

terrenos paraautóctones de arco à borda continental do Cráton Amazônico (evento que marca a acreção do Terreno Andaquí). Por fim, um metamorfismo de facies granulito de *ca*. 990 Ma teria ocorrido como consequência da colisão continental com a província sueco-norueguesa de Báltica durante a constituição final de Rodínia.

O Terreno Tahamí é um bloco litosférico limitado a leste pela Falha Otú-Pericos e a oeste pela Falha San Jerónimo que constitui a parte intermediária-norte da Cordilheira Central Colombiana. Este terreno está composto por xistos de baixo a meio grau, anfibolitos, mármores, gnaisses, granulitos e migmatitos de metamorfismo de baixa pressão intrudidos por plútons principalmente ácidos, tanto sintectônicos quanto post-tectônicos (González, 2001; Vinasco *et al*., 2006). Idades permianas têm sido determinadas para os protólitos dos plútons sintectônicos, enquanto que o posterior metamorfismo destas rochas e das suas encaixantes paraderivadas está em torno de 250-220 Ma, com os plútons mais jovens mostrando pouca ou nenhuma fábrica deformacional (Vinasco *et al*., 2006; Restrepo *et al*., 2011). Um segundo grupo de plútons não deformados é representado por grandes volumes de granodioritos e tonalitos com fases monzograníticas e máficas subordinadas. Estes corpos definem um expressivo cinturão magmático composto por duas faixas com idades de 130-107 Ma e 98-58 Ma (González, 2001; Correa *et al*., 2006; Ordóñez-Carmona *et al*., 2008a; 2011; Leal-Mejía *et al*., 2010; Bayona *et al*., 2012). Na parte noroeste da Cordilheira Central existem rochas metasedimentares de facies anfibolito a granulito intrudidas por tonalitos não deformados. Este conjunto é separado do resto do Terreno Tahamí pela Falha Espíritu Santo e possui idades de ~300 Ma para as rochas metamórficas e ~250 Ma para os tonalitos. Baseado nestas idades e dados de geoquímica isotópica de Nd, Ordóñez-Carmona & Pimentel (2002a) propuseram que este conjunto representa um bloco independente do terreno Tahamí para o qual deram o nome de Terreno Panzenú. A continuação para NNE deste terreno parece estar coberta pelos sedimentos Cenozóicos da Chapada Caribe, nas áreas marcadas como "Tahamí Incerto" da figura 4. Dados geocronológicos de U-Pb de testemunhos do embasamento apresentados por Montes *et al*. (2010) naquela região parecem confirmar esta última hipótese. Por outro lado, a oeste da parte norte da Cordilheira Central afloram xistos e anfibolitos de metamorfismo de média pressão com idades entre 400 e 360 Ma (Restrepo *et al*., 2008b; Restrepo *et al*., 1991) intrudidos por plútons graníticos metamorfizados com idade próxima a 390 Ma (Restrepo *et al*., 1991; Vinasco *et al*., 2007). Segundo Restrepo *et al*. (2008b) estas características indicariam que aquele grupo de rochas constitui um terreno independente o qual denominaram Terreno Anacona. Adicionalmente, para norte deste último terreno, perto da cidade de Medellín, afloram anfibolitos e dunitos serpentinizados que, com base em petrografia, litogeoquímica e geocronologia foram interpretados como parte de um complexo ofiolítico de zona de supra-subducção que poderia ter sido gerado no Triássico para depois ser obductado no continente entre o Triássico Tardio e o Cretáceo (Correa *et al*., 2005; Restrepo, 2008a). Dados geocronológicos dessas unidades indicam perturbações termais causadas pela obducção sobre o Terreno Tahamí (Restrepo *et al*., 2008a). Este terreno teria sido amalgamado junto com o Terreno Calima durante o início do Cretáceo antes de ser acrecionado ao Terreno Chibcha durante o Cretáceo Tardio (Toussaint & Restrepo, 1996). Porém, dados geocronológicos de Kerr *et al*. (1997) de rochas do Terreno Calima restringiriam o momento de amalgamação entre este último terreno e o Tahamí ao Cretáceo Tardio.

Na região entre os terrenos Calima e Tahamí existe uma faixa com trend NNE-SSW contida entre as falhas San Jerónimo e Cali-Patía caracterizada pela presença de vários blocos autóctones e paraautóctones de diversas naturezas e mostrando complexas relações estruturais entre eles. Estes blocos, os quais representam fragmentos litosféricos que existiam entre os terrenos Calima e Tahamí e que ficaram presos entre eles após a sua amalgamação, consistem em rochas máficas, ultramáficas e vulcano-sedimentares do Cretáceo geradas num ambiente oceânico com características relacionadas a subducção e platôs (*e.g.*, Nívia *et al*., 2006; Kerr *et al*., 1997; Moreno-Sánchez & Pardo-Trujillo, 2002). Também existem nessa área unidades gabróicas e ultramáficas isoladas (González, 2001), rochas metamórficas de meia a alta pressão com protólitos vulcano-sedimentares e de tipo MORB (Restrepo *et al*., 2008b; Bustamante & Juliani, 2011; Villagómez *et al*., 2011), blocos continentais retrabalhados, granitóides do Cretáceo Tardio (os quais intruem as unidades anteriores) e rochas vulcano-clásticas e sedimentares do Cenozóico (González, 2001).

O Terreno Calima é composto quase exclusivamente por rochas de afinidade oceânica, principalmente basaltos, tanto maciços quanto em *pillow*, gabros isotrópicos e acamadados, noritos, olivina-noritos, gabro-noritos, dunitos, clinopiroxenitos, tufitos, folhelhos, calcários, grauvacas e cherts do Cretáceo Superior. Em alguns casos as rochas sedimentares apresentam efeitos metamórficos de baixo grau passando para ardósias e filitos (Barrero, 1979; INGEOMINAS-BGS, 1984; INGEOMINAS, 2005).

As rochas máficas e ultramáficas deste Terreno teriam sido geradas num ambiente de platô oceânico associado a uma pluma (Kerr *et al*., 1997; Kerr, 2005), embora uma origem relacionada a uma *slab-window* do Cretáceo Tardio no proto-Caribe também tem sido proposta (Serrano *et al*., 2011). Este terreno encontra-se limitado a leste pela Falha Cali-Patía e a oeste pelas falhas de Dabeiba-Pueblo Rico e Buenaventura. A sua amalgamação junto com o Terreno Tahamí teria ocorrido durante o Cretáceo Tardio segundo considerações geocronológicas de Kerr *et al*. (1997).

O Terreno Gorgona corresponde a um bloco de crosta oceânica localizado na parte sul do litoral Pacífico Colombiano, composto por basaltos, komatiitos, brechas picríticas, gabros e olivina-gabros do Cretáceo Superior acompanhados por rochas sedimentares marinhas do Eoceno Meio a Mioceno (Gansser, 1950; Echeverria, 1980; Kerr *et al*., 1996). Segundo as características texturais, geoquímicas e isotópicas das rochas vulcânicas máficas e ultramáficas da ilha de Gorgona, tanto uma origem relacionada a uma pluma (Kerr *et al*., 1996; Sinton *et al*., 1998; Kerr, 2005) quanto uma *slab-window* no proto-Caribe durante o Cretáceo Tardio (Serrano *et al*., 2011) tem sido propostas para as unidades que compõem o Terreno Gorgona. Este terreno é separado dos terrenos Calima e Cuna pelas falhas de Buenaventura e Garrapatas, respectivamente, e a sua acreção ao primeiro teria ocorrido durante o Eoceno Tardio (Kerr, 2005; Cediel *et al*., 2010; Serrano *et al*., 2011).

O Terreno Cuna teria sido acrecionado ao resto do mosaico de blocos litosféricos dos Andes Colombianos durante o Mioceno ao longo da Falha Dabeiba-Pueblo Rico (Toussaint & Restrepo, 1996; Cediel *et al*., 2010), embora uma idade cretácea tardia também tem sido sugerida para essa acreção (Kerr *et al*., 1997; Kerr, 2005). Este terreno é composto por basaltos maciços e em *pillow*, brechas basálticas, doleritos, gabros, andesitos e tufitos com intercalações de siltitos, arenitos e cherts do Cretáceo Tardio. Rochas vulcânicas de possível idade paleógena também têm sido reportadas na forma de domos que cortam as unidades anteriores ou como fluxos cobrindo as mesmas em inconformidade (Kerr *et al*., 1997; INGEOMINAS, 2005). O conjunto litológico anterior é intrudido por batólitos e stocks de composição tonalítica, granodiorítica e quartzo-diorítica (localmente apresentando texturas porfiríticas) do Eoceno (Sillitoe *et al*., 1982; Botero, 1975; Göbel & Stibane, 1979) com alterações hidrotermais e mineralizações de Au e Cu do Oligoceno (Sillitoe *et al*., 1982). A origem das rochas máficas do Terreno Cuna estaria associada aos mesmos contextos indicados por Kerr *et al*. (1997) e Serrano *et al*. (2011) para as rochas máficas dos terrenos Calima e Gorgona.

O Terreno Chibcha possui características que têm sido mais difíceis de observar visto que se encontra coberto quase totalmente por rochas sedimentares do Paleozóico, Mesozóico e Cenozóico da Cordilheira Oriental, o vale do rio Magdalena e as bacias Cesar-Ranchería e da Guajira. As exposições do embasamento deste terreno ocorrem ao longo da margem oriental da Cordilheira Central, no Maciço de Santander, na Serra Nevada de Santa Marta, na Península da Guajira e na Serrania de San Lucas (Toussaint & Restrepo, 1996; Ordóñez-Carmona *et al*., 2006). Porém, dados paleomagnéticos apresentados por Bayona *et al*. (2006; 2010) sugerem que esses maciços, em grande parte, não constituem uma unidade litosférica só, e sim um mosaico de blocos com idades e histórias tectono-magmáticas similares. O limite oriental do terreno é representado pelo sistema de falhas de Guaicáramo, enquanto que a falha Otú-Pericos na margem oriental da Cordilheira Central marcaria o seu limite ocidental (Restrepo & Toussaint, 1988). A acreção do Terreno Chibcha à margem noroeste da América do Sul teria ocorrido durante o Paleozóico Tardio (Toussaint & Restrepo, 1996).

A Serra Nevada de Santa Marta é constituída por três domínios limitados por falhas ou lineamentos paralelos com direção NE-SW (Gansser, 1955; Tschanz *et al*., 1974). De SE para NW esses domínios correspondem à Província Serra Nevada, composta por rochas metasedimentares pré-cambrianas em fácies granulito cobertas por sedimentos do Paleozóico Tardio, depósitos de ignimbritos triássico-jurássicos e sedimentos marinhos do Cretáceo, além de serem intrudidas por plútons graníticos contemporâneos com os ignimbritos. Posteriormente aparece a Província de Sevilla, constituída por um embasamento de gnaisses máficos e xistos intrudidos por plútons sintectônicos, e a Província Santa Marta, composta por uma faixa interna de xistos em fácies anfibolito e uma faixa externa estruturalmente complexa que agrupa xistos verdes e filitos intrudidos por granitóides do Eoceno. As rochas paraderivadas em facies granulito da Província Serra Nevada têm mostrado idades de metamorfismo entre 1140 e 970 Ma e T_{DM} Nd em torno de 1700 Ma (Ordóñez-Carmona *et al*., 2002b; Restrepo-Pace *et al*., 1997; Cordani *et al*., 2005). O metamorfismo dos paragnaisses da Província de Sevilla foi datado em ~500 Ma (Cardona *et al*., 2006), enquanto que na província Santa Marta, geocronologia de U-Pb em zircão e K-Ar em micas, hornblendas e rocha total nos xistos e gnaisses permite estabelecer uma idade cretácea tardia para o metamorfismo com perturbações termais durante o Eoceno (MacDonald *et al.*, 1971; Tschanz *et al.*, 1974; Cardona *et al.*, 2008; Cardona *et al.*, 2010b).

A Península da Guajira apresenta uma geologia correlacionável com aquela da Serra Nevada de Santa Marta, com maciços isolados de rochas metasedimentares pré-cambrianas de alto grau intrudidas por plútons do jurássico e separadas estruturalmente de sequências metavulcanosedimentares cretáceas intercaladas com rochas ultramáficas intrudidas por magmas do eoceno (MacDonald, 1964; Lockwood, 1965; Alvarez, 1967). As rochas paraderivadas de alto grau mostraram idades metamórficas U-Pb entre 1160 e 915 Ma, enquanto que rochas da Formação Macuira apresentaram idades similares àquelas das rochas metamórficas da Província de Sevilla na Serra Nevada de Santa Marta, com as quais compartilham semelhanças litológicas e estratigráficas (Cardona *et al.*, 2006). As rochas da Formação Macuira são intrudidas por dioritos com idades próximas a 160 Ma, valores negativos de ε_{Nd} e T_{DM} Nd de 1450 Ma (Cardona *et al.*, 2006).

O embasamento do Maciço de Santander é composto por silimanita-cordierita-granada paragnaisses, xistos e migmatitos pré-cambrianos de alto grau cobertos possivelmente em inconformidade por filitos, xistos, metasiltitos, metaarenitos, mármores e metabasitos. Corpos de orto-gnaisses cortam os dois grupos litológicos anteriores. Esse embasamento encontra-se coberto por rochas sedimentares do devoniano médio até o cretáceo, que apresentam fraco ou nenhum metamorfismo, e é intrudido por granitóides do Triássico-Jurássico (Ward *et al.*, 1973). Os paragnaisses de alto grau possuem idades de metamorfismo entre 1110 e 860 Ma (Goldsmith *et al.*, 1971; Cordani *et al.*, 2005) enquanto os ortognaisses possuem idades próximas a 413 Ma, o que indicaria uma idade mínima para as rochas de baixo grau que recobrem discordantemente os paragnaisses de alto grau (Goldsmith *et al.*, 1971). Os granitóides apresentam idades entre 185 e 210 Ma (Goldsmith *et al.*, 1971; Dörr *et al.*, 1995) e produzem efeitos termais que são refletidos em idades aparentes menores das unidades encaixantes.

A margem oriental da Cordilheira Central, a leste da Falha Otú-Pericos, é caracterizada pela presença de rochas metamórficas de médio a alto grau representadas por gnaisses, anfibolitos e mármores com idades entre 890 e 1100 Ma (Ordóñez-Carmona *et al.*, 1999; Restrepo-Pace *et al.*, 1997) cobertos em alguns lugares por rochas sedimentares fracamente metamorfizadas com fósseis de graptolitos ordovicianos

(Harrison, 1929; Botero, 1940; Mojica *et al*., 1988). Estas unidades são intrudidas por batólitos de granitóides geralmente alongados em sentido NS e com idades entre 130 e 214 Ma (Feininger *et al*., 1973; Vesga & Barrero, 1978; Sillitoe *et al*., 1982; McCourt *et al*., 1984; Jaramillo *et al*., 1980).

Na Serrania de Perijá e no Maciço de Quetame, este último localizado para norte da Serrania de La Macarena, afloram metaarenitos e filitos de baixo a meio grau cobertos por rochas sedimentares do Devoniano (Forero, 1970; Renzoni, 1962, 1968; Stibane, 1969; Gröser & Prössl, 1991). Estas rochas poderiam ser correlacionáveis com o embasamento metamórfico pré-devoniano de baixo a médio grau descrito no Maciço de Santander (Ordóñez-Carmona *et al*., 2006).

2.3. GEOLOGIA DA SSL: TRABALHOS ANTERIORES

A SSL corresponde ao extremo setentrional da Cordilheira Central e localiza-se a leste da Falha Otú-Pericos, fazendo então parte do Terreno Chibcha descrito na seção anterior. O mapa geológico regional desta zona pode ser conferido na figura 6.

Entre os primeiros trabalhos realizados na SSL pode ser citado aquele de Bogotá & Aluja (1981), que apresenta a primeira síntese geológica baseada em trabalhos de campo para prospecção de urânio ordenada pelo Governo Colombiano. Eles propuseram modificações ao mapa fotogeológico publicado anteriormente por INGEOMINAS (1977) e descreveram aspectos litológicos, estratigráficos e estruturais da região. Os autores reconheceram gnaisses e anfibolitos de médio a alto grau de possível idade pré-cambriana, mica-xistos e xistos carbonosos do Paleozóico Inferior, rochas sedimentares subaéreas e vulcânicas intermediárias a félsicas do Jurássico Inferior a Médio, atualmente agrupadas dentro da Formação Noreán, que foram intrudidas por corpos dioríticos-granodioríticos do Batólito de Norosí, o qual é considerado a continuação para norte do Batólito de Segovia no Departamento de Antioquia. Calcários, margas e folhelhos de ambiente marinho raso do Cretáceo foram depositados acima das unidades anteriores. Três sistemas de falhas foram destacados na região: sistema NS, que é expressivo na parte ocidental da serrania e é associado às falhas de Palestina e Otú-Pericos, sistemas N55E e N25W ressaltados no domínio central e aparecendo também na porção oriental, embora atenuados devido aos processos geomorfológicos da depressão do vale do rio Magdalena.

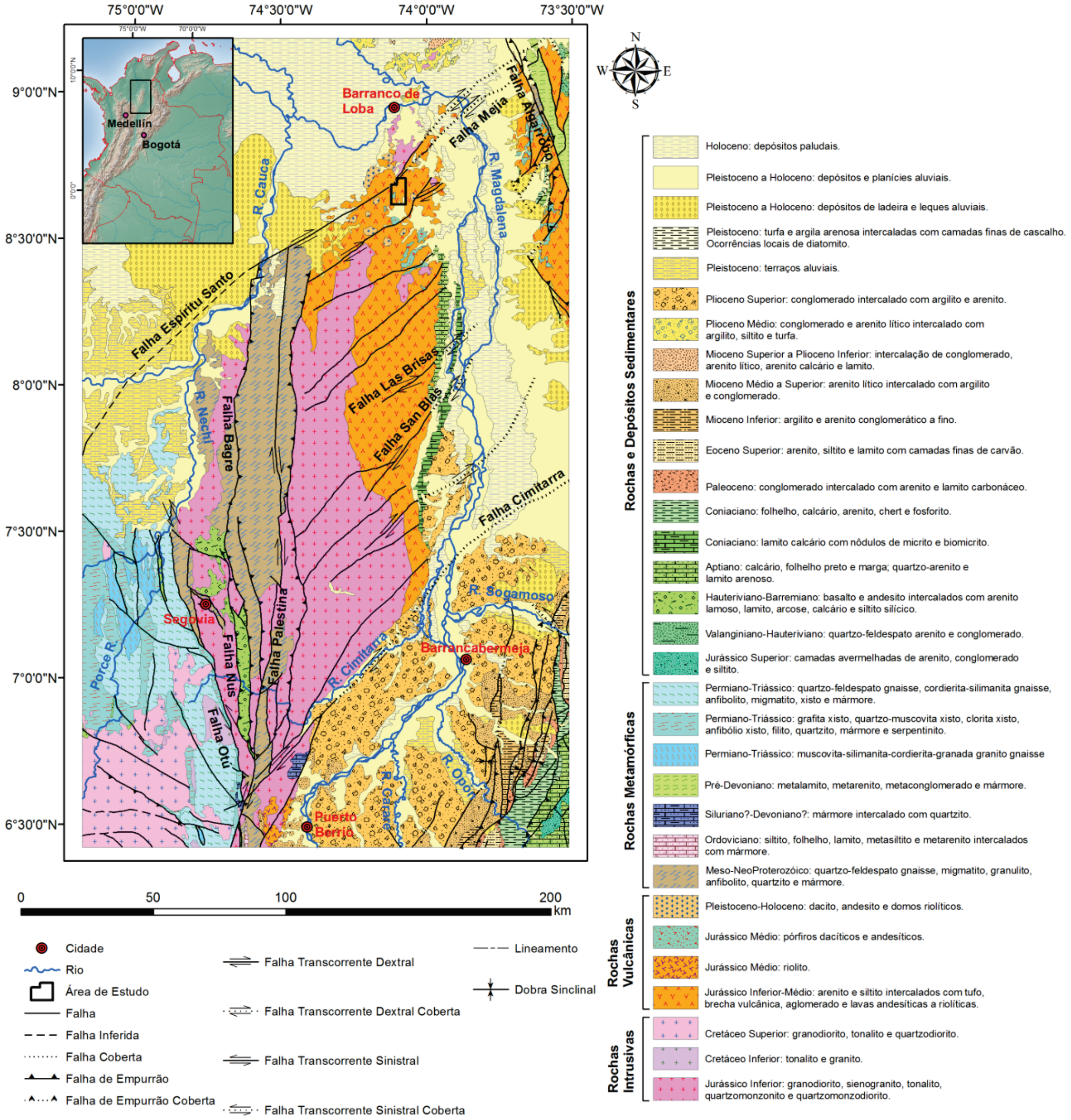

Figura 6 – Mapa geológico regional da SSL. Modificado de INGEOMINAS (2007).

Galvis & De La Espriella (1992) fizeram uma revisão das características litológicas e estruturais da parte norte da SSL. As suas observações são fundamentalmente similares àquelas feitas por Bogotá & Aluja (1981), enfatizando a presença de paragnaisses migmatizados, granitos anatécticos e a ocorrência de supostas rochas vulcânicas e sub-vulcânicas félsicas do Terciário. Entretanto, a idade terciária proposta pelos autores é suportada só na base de feições geomorfológicas, sem datações radiométricas ou relações com rochas fossilíferas que permitam inferências confiáveis da idade.

Ordóñez-Carmona *et al.* (2008b) reportaram a presença de granulitos máficos no município de Barranco de Loba, na parte norte da SSL. Estas rochas ainda possuem ortopiroxênio, mas encontram-se parcialmente retrogradadas para a fácies anfibolito. Embora sem datações radiométricas, estes autores acharam razoável supor uma idade neoproterozóica para estas rochas, na base de correlações com o embasamento metamórfico de alto grau da Serra Nevada de Santa Marta e o Maciço de Garzón (Ordóñez-Carmona *et al.*, 1999). Posteriormente, Ordóñez-Carmona *et al.* (2009) reportaram uma idade U-Pb em zircão de 1501 Ma para os Gnaisses de San Lucas, a qual foi interpretada como o momento da cristalização do protólito ígneo dessas rochas. Adicionalmente, datações com o mesmo método em zircões dos granodioritos do Batólito de Norosí apresentaram uma idade próxima de 184 Ma para a cristalização destes magmas.

INGEOMINAS e a Universidade Industrial de Santander (UIS) apresentaram em 2006 os resultados de um projeto de mapeamento cobrindo a SSL e partes dos vales médio e inferior do rio Magdalena. Litologicamente, os Gnaisses de São Lucas são descritos como quartzo-feldespato gnaisses e hornblenda-gnaisses com paragêneses minerais indicando um metamorfismo em fácies anfibolito, zona da silimanita. O Batólito de Norosí foi descrito como uma suíte intrusiva do Jurássico Médio contendo monzogranitos e granodioritos com enclaves máficos. As suas características químicas e isotópicas permitiram classificar aquelas rochas dentro da série calci-alcalina de alto potássio, com feições de granitoides tipo I e S. As rochas vulcânicas e vulcano-clásticas da Formação Noreán foram descritas como dacitos, riolitos, tufitos latíticos soldados, lavas riolíticas porfiríticas e andesitos calci-alcalinos de alto potássio, com raras ocorrências de basaltos acompanhando essas unidades.

Análises de U-Pb ID-TIMS em frações de zircões de granulitos da parte norte da SSL permitiram estimar idades médias ^{207}Pb/^{206}Pb entre 1140 e 1170 Ma, com duas frações apresentando idades de 1215 e 1781 Ma, interpretadas como a idade do metamorfismo Grenvilliano destas rochas (INGEOMINAS-UIS, 2006). Adicionalmente os mesmos granulitos apresentaram T_{DM} Nd de 1.6 Ga, enquanto que diques de gabros foliados próximos ao povoado de Pueblito Mejía apresentaram idades modelo de 0.6 Ga (INGEOMINAS-UIS, 2006). Para amostras de *stocks* associados ao Batólito de Norosí, conjuntos de análises de feldspato potássico e rocha total apresentaram idades errócronas Rb-Sr de 166.9 ± 6 Ma com razões ^{87}Sr/^{86}Sr iniciais de 0.70717. Análises similares de outro *stock* da mesma unidade mostraram uma idade de 185 ± 46 Ma com razões ^{87}Sr/^{86}Sr iniciais de 0.7067 (INGEOMINAS-UIS, 2006). Três datações K-Ar de riolitos, anfibólio-xistos e quiastolita-xistos revelaram idades de 194 ± 6 Ma, 86 ± 3 Ma e 92 ± 5 Ma, respectivamente. A primeira idade foi interpretada como o momento de solidificação da lava, enquanto que as idades cretáceas tardias dos xistos indicariam eventos de cisalhamento e exumação, associados à atividade da Falha Palestina. (INGEOMINAS-UIS, 2006).

Mesz (2008) realizou análises químicas de elementos maiores e traço e de geoquímica isotópica nas rochas do Batólito de Norosí e em algumas das unidades metamórficas encaixantes na parte norte da SSL. Datações K-Ar de biotita de granodiorito mostraram idades entre 190 e 200 Ma. A química de elementos maiores indicou um caráter metaluminoso e uma tendência calci-alcalina para estas rochas, com os elementos traço mostrando padrões compatíveis com origem em zona de subducção. Dados isotópicos de Nd e Sr revelaram valores de $\varepsilon_{Nd}(T)$ entre -6 e -4 e uma média da razão $^{87}Sr/^{86}Sr$ inicial de 0.707, valores que sugerem um importante componente crustal para a fonte do magma que gerou o batólito. Valores de T_{DM} Nd variaram entre 1000 e 1200 Ma, o que indicaria um envolvimento do embasamento Grenvilliano na origem do Batólito de Norosí. Rochas Grenvillianas já tinham sido reconhecidas em setores próximos na Cordilheira Central e maciços similares (e.g., Kroonenberg, 1982a, 1982b; Ordóñez-Carmona *et al.*, 1999; 2006).

Na consideração do potencial econômico, análises isotópicas de enxofre em sulfetos de veios com mineralizações de ouro encaixados tanto nas rochas metamórficas quanto nos granitóides do norte da SSL deram valores de $\delta^{34}S_{CDT}$ entre -0.1 e +3.1‰, indicando uma origem do enxofre a partir de um reservatório manto-derivado. Estimações com base em pares isotópicos de galena e pirita permitiram obter temperaturas de formação/equilíbrio dos sulfetos entre 343 e 556ºC. Estas temperaturas contrastam com aquelas estimadas a partir de microtermometria de inclusões fluidas em veios com direção N80W/78NE encaixados nos Gnaisses, que apresentaram valores menores de 200ºC para inclusões do sistema aquoso (INGEOMINAS-UIS, 2006). Porém, os autores não deixam claro se estes veios pertencem ao mesmo sistema no qual foram feitas as análises isotópicas de enxofre e se eles são associados também a mineralizações de ouro.

Ordóñez-Carmona *et al.* (2008c) descreveram algumas feições estruturais dos veios auríferos localizados na parte norte da SSL. Eles observaram um importante controle estrutural nos veios exercido por estruturas tectônicas com características de deformação transtensional progressiva num regime rúptil a transicional. Os principais trends dos veios correspondem àqueles de falhas e juntas pré-existentes com disposições N5-20E e N55-70W. O primeiro deles é considerado coetâneo com estruturas extensionais de veios que sofreram deslocamentos contemporâneos a tardios produzidos por estruturas de cisalhamento do segundo sistema NWW. Estes domínios teriam sido posteriormente afetados por movimentos transcorrentes sinistrais de estruturas regionais representadas por lineamentos NW-SE.

Na parte sul ocidental da SSL, Londoño *et al.* (2009) descreveram as mineralizações auríferas do distrito mineiro Bagre-Nechí o qual consiste, para sul, em veios de quartzo e sulfetos com disposições N5E/45SE e N20W/52SW encaixados em granitóides do Batólito de Segovia, enquanto que, para norte, os veios correspondem a estruturas N25E/40NW que cortam quartzo-dioritos e migmatitos, estes últimos associados ao Gnaisse de San Lucas. Levando em conta aspectos tais como baixa proporção modal de sulfetos, estruturas internas bandadas, encaixantes deformadas em regimes rúpteis a dúcteis, deformação contemporânea com aquela das encaixantes, presença de ouro livre e proximidade à Falha Otú-Pericos que teve uma antiga cinemática transcorrente dextral, e ao distrito mineiro de Segovia-Remedios, os autores propõem classificar os veios mineralizados do distrito Bagre-Nechí como parte de um depósito de ouro orogênico, sem desconsiderar a possibilidade de relação com outros contextos metalogenéticos.

CAPÍTULO 3: MÉTODOS ANALÍTICOS

3.1. GEOQUÍMICA DE ELEMENTOS MAIORES E TRAÇO

As análises em rocha total foram realizadas pela AcmeLabs Ltd. seguindo as rotinas analíticas 4A e 4B. A primeira delas consistiu na determinação de elementos maiores e menores por meio de ICP-AES de 0.2 g de amostra moída e homogeneizada após fusão com metaborato/tetraborato de lítio e digestão em HNO_3 diluído. As perdas por ignição foram medidas por diferença em peso após queima a 1000ºC, enquanto que as análises de carbono e enxofre totais foram feitas por meio da rotina 2A em forno Leco. Na rotina 4B, as concentrações dos ETR e elementos refratários foram determinadas com ICP-MS aplicando a mesma preparação usada na rotina 4A. Adicionalmente, uma fração separada de 0.5 g foi dissolvida em água régia e analisada por ICP-MS. Os resultados dos elementos maiores e menores foram reportados como porcentagens em peso dos óxidos com limites médios de detecção (LMD) de 0.01 % em peso (exceto para o Cr_2O_3 e o Fe_2O_3 que tiveram LMD de 0.002 e 0.04 % em peso, respectivamente; todo o ferro nas amostras foi reportado como Fe_2O_3). O LMD para as análises 2A Leco foi 0.02 % em peso. Para os elementos traço, os LMD obtidos foram 0.01 ppm (Tb, Tm e Lu), 0.02 ppm (Pr, Eu e Ho), 0.03 ppm (Er), 0.05 ppm (Sm, Gd, Dy e Yb), 0.1 ppm (La, Ce, Cs, Hf, Nb, Rb, Ta, U, Y, Zr e Cu), 0.2 ppm (Th), 0.3 ppm (Nd), 0.5 ppm (Ga e Sr) e 1 ppm (Ba, Sn e Zn).

3.2. GEOCRONOLOGIA DE U-Pb

O método e arranjo dos equipamentos usados nas análises isotópicas de U-Pb foram baseados naqueles apresentados por Bühn *et al.* (2009). As análises foram realizadas no laboratório de geocronologia da Universidade de Brasília usando um espectrômetro de massa Thermo Finnigan Neptune Multicollector ICP-MS. A entrada da substância mineral no espectrômetro foi conseguida por meio de ablação com um laser de estado sólido New Wave 213 µm Nd-YAG. As condições de análise variaram segundo as características das amostras com o objetivo de otimizar os sinais isotópicos; o diâmetro do feixe variou entre 10 e 30 µm com uma energia entre 0.5 e 1.2 J/cm^2 e frequência de 10 Hz.

Grãos de zircão separados a mão, concentrados com ajuda de uma bateia a partir de amostras de rocha britada ou de saprólito, foram colocados em tubos plásticos de 9 mm de diâmetro preenchidos com resina. Os grãos foram posteriormente polidos usando pasta de diamante de 3 e 1 μm de diâmetro e limpados com ultrassom em HNO_3 a 3% e água purificada. Posteriormente, imagens de catodoluminiscência (CL) foram adquiridas para ajudar a posicionar corretamente o feixe do laser de acordo com a estrutura interna dos minerais durante a fase de ablação.

O preparado com os grãos foi inserido numa câmara com um fluxo de He entre 0.35 e 0.45 l/min. A remoção do ^{204}Hg no fluxo de He foi conseguida passando o gás através de tubos de vidro contendo partículas de quartzo cobertas com ouro; isto foi feito para minimizar a interferência isobárica com o ^{204}Pb e permitir a aplicação das correções do Pb comum.

Depois de passar no plasma de argônio, o material vaporizado foi transportado até a zona do detector que consistiu em seis contadores de íons multicanal (MICs). Para a análise do padrão e as amostras, os sinais foram coletados num bloco único com 40 ciclos de 1.049 s cada, começando as leituras dos sinais só após os últimos terem atingindo a máxima intensidade no início da ablação.

A técnica de *bracketing* entre padrões foi aplicada por meio das leituras da análise de um ponto no padrão e um “branco” a cada quatro ou oito pontos analisados nas amostras, com o objetivo de considerar o erro causado pela deriva instrumental do espectrômetro. O padrão internacional usado foi o zircão GJ-1, fornecido pelo ARC National Key Centre for Geochemical Evolution and Metallogeny of Continents (GEMOC) na Austrália. As suas idades de referência segundo Jackson *et al*. (2004) são: 608.6 ± 1.1 Ma (idade ^{207}Pb/^{206}Pb), 600.4 ± 1.8 Ma (idade ^{206}Pb/^{238}U) e 602.1 ± 3.0 Ma (idade ^{207}Pb/^{235}U).

A redução dos dados foi conseguida usando uma planilha elaborada no mesmo laboratório de geocronologia, avaliando as razões isotópicas dos 40 ciclos com um critério de rejeição baseado num nível de confiança 2σ. As razões isotópicas corrigidas junto com as suas idades calculadas associadas foram plotadas usando a rotina ISOPLOT 3.71 (Ludwig, 2009).

3.3. GEOQUÍMICA ISOTÓPICA DE Nd E Sr

As análises de Sm-Nd e Sr-Sr foram realizadas no laboratório de geocronologia da Universidade de Brasília. Os procedimentos aplicados são os mesmos descritos por Gioia & Pimentel (2000). As amostras de rocha foram moídas e homogeneizadas para separar 50-100 mg de material homogêneo o qual foi dosado com soluções ^{149}Sm e ^{150}Nd e posteriormente atacado com 1 ml de HNO_3 e 4 ml de HF em bombas de teflon com revestimento de aço. Após dissolução, as amostras foram secadas e atacadas de novo com a mesma mistura ácida durante quatro dias a 190ºC, o qual foi seguido por uma nova fase de secagem e posterior dissolução com 2 ml de HNO_3 concentrado. Depois de secar, o resíduo foi dissolvido mais uma vez com 6 ml de HCl (6N) para ser novamente secado e por fim dissolvido em 2 ml de HCl (2.5N).

A separação dos ETR foi feita numa coluna primária de quartzo de 15 cm altura contendo 12 cm de resina catiônica Bio-Rad AG 50W-X8 200-400 *mesh* em solução aquosa. A amostra em solução foi eluida através da coluna usando HCl. Os ETR foram coletados na fração entre 1 e 15 ml do HCl 6N após eluição com 32 ml de HCl 2.5 N. A coluna foi regenerada com 15 ml de HCl 6N e armazenada em solução com ácido diluído. O HCl 2.5N foi padronizado mediante titrimetria usando $NaCO_3$ (anidro) como base e alaranjado de metila como indicador.

Para conseguir separar o Sm do Nd, a solução de ETR em 200 μl de HCl 0.18N foi passada através de uma coluna secundária de Savillex® de 10 cm de altura contendo 6.5 cm de resina LN-Spec (resina liquida HDEHP 270-150 *mesh* em teflon coberto com di-etilexil ácido fosfórico). A fração de Nd foi coletada em 4 ml de HCl 0.3N após 10 ml iniciais de HCl 0.18N. Com a coleta do Nd completada, 2 ml de HCl 0.3N foram descartados para depois obter o Sm em 4 ml de HCl 0.4N com uma velocidade de fluxo de ~1 ml/30 min. A regeneração da resina foi feita usando 6 ml de HCl 6N, e a coluna foi condicionada novamente com 3 ml de água purificada seguida de duas rodadas com 3 ml de HCl 0.18N.

A fração coletada na coluna secundária foi evaporada junto com duas gotas de H_3PO_4 0.025N. O resíduo foi dissolvido em 1 μl de HNO_3 destilado a 5% e colocado num filamento duplo de Re. O espectrômetro de massa usado foi um Finnigan MAT 262 com sete coletores em modo estático.

As incertezas nas razões $^{147}Sm/^{144}Nd$ e $^{143}Nd/^{144}Nd$ foram menores do que 0.2% (2σ) e 0.0045% (2σ), respectivamente, com base na análise do padrão internacional BHVO-1. A razão $^{143}Nd/^{144}Nd$ foi normalizada usando $^{146}Nd/^{144}Nd = 0.7219$. A constante de decaimento radioativo usada foi $6.54 \times 10^{-12}\ a^{-1}$ (Lugmair & Marti, 1978).

Para a separação do Sr, 200 mg de rocha pulverizada foram dissolvidos em 4 ml de HF e 1 ml de HNO_3 em bombas de teflon. Após secagem, uma nova dissolução foi feita com 6 ml de HNO_3 a qual foi seguida de secagem e dissolução com 6 ml de HCl 6N. Mais uma fase de secagem foi realizada antes de dissolver o resíduo resultante em 3ml de HCl 2.5N. Esta última solução foi centrifugada para depois coletar 1ml de sobrenadante e passá-lo através de uma coluna de troca catiônica com resina AG 50W X8 peneira 200-400. A eluição foi conseguida usando 37 ml de HCl 2.5N e coletando o Sr nos primeiros 15 ml de solução a qual foi posteriormente evaporada para obter o elemento na forma de sais. Estes sólidos foram colocados junto com 1µl de H_3PO_4 num filamento de Ta do mesmo espectrômetro usado nas análises de Sm-Nd. Com base em análises do padrão internacional NBS987, as incertezas das razões medidas de $^{87}Sr/^{86}Sr$ foram menores do que 0.0036% (2σ). A razão $^{87}Rb/^{86}Sr$ foi calculada a partir das concentrações de Rb e Sr obtidas nas análises litogeoquímicas de rocha total usando a fórmula:

$$^{87}\mathrm{Rb}\Big/{}^{86}\mathrm{Sr} = \frac{\mathrm{Rb} * \mathrm{Ab.}\,^{87}\mathrm{Rb} * \mathrm{A.w.Sr}}{\mathrm{Sr} * \mathrm{Ab.}\,^{86}\mathrm{Sr} * \mathrm{A.w.Rb}}$$

Onde:

Rb=concentração de Rb obtida nas análises de elementos traço.

Ab.^{87}Rb=abundância do ^{87}Rb (igual a 27.835%; Steiger & Jäger, 1977).

A.w.Sr=peso atômico do Sr recalculado para cada amostra a partir das abundâncias de ^{84}Sr, ^{86}Sr, ^{87}Sr e ^{88}Sr, e segundo as razões constantes $^{86}Sr/^{88}Sr=0.1194$ e $^{84}Sr/^{86}Sr=0.056584$ (Steiger & Jäger, 1977).

Sr=concentração do Sr obtida nas análises de elementos traço.

Ab.^{86}Sr=abundância do ^{86}Sr recalculada para cada amostra a partir das razões $^{87}Sr/^{86}Sr$ medidas no laboratório e das razões constantes $^{86}Sr/^{88}Sr$ e $^{84}Sr/^{86}Sr$ de Steiger & Jäger (1977).

A.w.Rb=peso atômico do Rb (igual a 85.46776 u.m.a.).

A constante de decaimento radioativo usada foi aquela de Nebel *et al.* (2011) com um valor de $1.393 \times 10^{-11}\ a^{-1}$.

CAPÍTULO 4: "GEOCHEMICAL AND GEOCHRONOLOGICAL CONSTRAINTS ON THE NATURE AND GEODYNAMICS OF THE MESOPROTEROZOIC BASEMENT OF THE NORTHERN PORTION OF THE SAN LUCAS RANGE (COLOMBIA)"

Federico A. Cuadros[a,1], Nilson F. Botelho[a], Oswaldo Ordóñez-Carmona[b]

[a]: Instituto de Geociências, Universidade de Brasília (IG-UnB), Brazil.
[b]: Facultad de Minas, Universidad Nacional de Colombia-Sede Medellín- (UNALMED), Colombia.

ABSTRACT

The San Lucas Range (SLR) is located at the northernmost end of the Central Cordillera of Colombia and is considered to be a part of the Chibcha Terrane, characterized by medium- to high-grade rocks yielding Late Mesoproterozoic-Early Neoproterozoic metamorphic ages. Granite-gneiss and metamafic rocks including metamonzogabbro, amphibolite and granulite crop out in the northern portion of the SLR, with a Lower Jurassic granodioritic batholith intruding all of the above mentioned units. Geochemical features in terms of major and trace element contents and U-Pb zircon geochronology suggest protolith crystallization of both felsic and mafic rocks in a post-collisional context between 1.54 and 1.50 Ga. In addition, positive $\varepsilon_{Nd}(T)$ values and initial $^{87}Sr/^{86}Sr$ ratios less than 0.7045 indicate a mantle origin for this bimodal association, with T_{DM} values between 1.5 and 1.7 Ga suggesting a juvenile character. A correlation between the studied rocks and the A-type Rio Uaupés Granitic Suite in the Rio Negro Province of the Amazonian Craton can be established, thus constraining a provenance from southern latitudes for the Chibcha Terrane as stated by earlier models. Metamorphic rims of zircons from both felsic and mafic rocks yielded ages between 1180 and 930 Ma, which are consistent with ages of related metamorphic terranes in Ecuador, Venezuela, Perú, México and Middle America. The latter are regarded as having been part of the northwestern border of Amazonia during its collision with Baltica in the context of the Grenvillian/Sveconorwegian orogeny related to the final assembly of Rodinia.

Keywords: San Lucas Range; A-type Granite; Post-collisional Granite; Transitional Mafic Rocks; Early Mesoproterozoic; Amazonia; Grenvillian/Sveconorwegian orogeny; Chibcha Terrane.

---

[1] Corresponding author.
e-mail address: facuadros@unb.br (F. A. Cuadros).

4.1. INTRODUCTION

The SLR is located at the northern end of the Central Cordillera of Colombia and has been long recognized by local inhabitants and some national and international mining companies as an important mineral prospect concerning Au and Ag mineralizations, with the former associated either to hydrothermal lodes or alluvial deposits. It is also one of the key places where the basement of the Chibcha (or Eastern Colombian) Terrane can be observed directly (Restrepo & Toussaint, 1988; Toussaint & Restrepo, 1996; Ordóñez-Carmona *et al.*, 2006). Despite its economic and geoscientific importance, the SLR remains as a virtually unexplored area devoid of detailed geological studies except for some recent works by Colombian universities, dealing with petrographic, structural, geochemical and ore-related aspects, and geological mapping by the Colombian Geological Service (INGEOMINAS). This general low amount of detailed knowledge is mainly the result of the lack of proper civil infrastructure in the region, which makes difficult to get access to the area and carry out the field work, as well as its unstable situation concerning security and social issues.

As an example, it has been recognized that the unit known as the San Lucas Gneiss is far from being lithologically homogeneous, as it groups several metamorphic rock types having different protoliths (*e.g.*, Feininger *et al.*, 1973). Nevertheless, this heterogeneous character has not come yet into a cartographic expression and the unit remains currently mapped as a whole entity along its entire extension. Another example of the poor geological understanding of this area has to do with the nature and origin of its gold mineralizations, for which a clear classification and a robust, quantitative data-supported metallogenetic model has not been stated yet.

The researches carried out in the SLR during the second half of the 20th century did not take the geological knowledge of the region beyond the petrographic and stratigraphic descriptions of its units, with few or no considerations about their genesis or geodynamic settings of formation having been made. During the 1990s and the first decade of the 21st century the first modern tectonic models for the Colombian Andes, particularly for the eastern and northern flanks of the Central Cordillera, began to be published, stressing the importance of the Grenvillian orogeny on its geological evolution (*e.g.*, Toussaint & Restrepo, 1996; Restrepo-Pace *et al.*, 1997; Ordóñez-Carmona *et al.*, 1999, 2002b, 2006; Cordani *et al.*, 2005; Cardona *et al.*, 2010a). This was a major breakthrough since it allowed articulating geologically that portion of the

Colombian Andes with the rest of the Andean chain, for which a Grenvillian geochronological signature has been recognized in the blocks that constitute its basement (*e.g.*, Fuck *et al*., 2008; Ramos, 2009; 2010).

At present, it is difficult to unravel the pre-Neoproterozoic geological history of the Colombian cordilleras, and this study constitutes one of the first attempts to assess the origin of some of the units that make up their basement. This work, although not intended to solve all of the problems and unknowns dealing with the regional geology of the SLR, does provide an insight into the nature and geodynamic evolution of one small part of the Range, namely its northernmost portion in the municipality of Barranco de Loba, south of the Bolívar department.

4.2. GEOLOGICAL SETTING

4.2.1. Regional framework

The geological evolution of the Colombian territory has been described within the context of terrane accretion models which state that the western portion of the country consists of a mosaic of allochthonous lithospheric blocks docked to the northwestern border of the Amazonian Craton (INGEOMINAS, 1983; McCourt *et al*., 1984; Restrepo & Toussaint, 1988). One of those blocks corresponds to the Chibcha Terrane, with its basement being almost entirely covered by Phanerozoic sedimentary rocks and displaying restricted exposures along the eastern flank of the Central Cordillera, the Quetame and Santander Massifs in the Eastern Cordillera, the Perijá Range, the Sierra Nevada de Santa Marta Massif and the Guajira Peninsula (Toussaint & Restrepo, 1996; Ordóñez-Carmona *et al*., 2006). A common characteristic linking these provinces is the presence of amphibolite to granulite facies, mainly paraderived metamorphic rocks that have yielded Grenvillian U-Pb ages between 1200 and 890 Ma for their metamorphism and resulted from reworking of pre-existent crustal materials as old as 1800 Ma (*e.g.*, Restrepo-Pace *et al*., 1997; Ordóñez-Carmona *et al*., 1999, 2002b, 2006; Cordani *et al*., 2005; Cardona *et al*., 2006; Cardona *et al*., 2010a). Locally, this basement is unconformably overlain by low-grade metasedimentary rocks displaying Ordovician-Silurian faunas and palynomorphs and unmetamorphosed sedimentary strata ranging from Devonian to Cenozoic in age (*e.g.*, Harrison, 1930; Botero, 1940; Mojica *et al*., 1987; Gröser & Prössl, 1991; Ward *et al*., 1973), which allows constraining a low-grade metamorphic event that took place during Late Silurian-Early Devonian times.

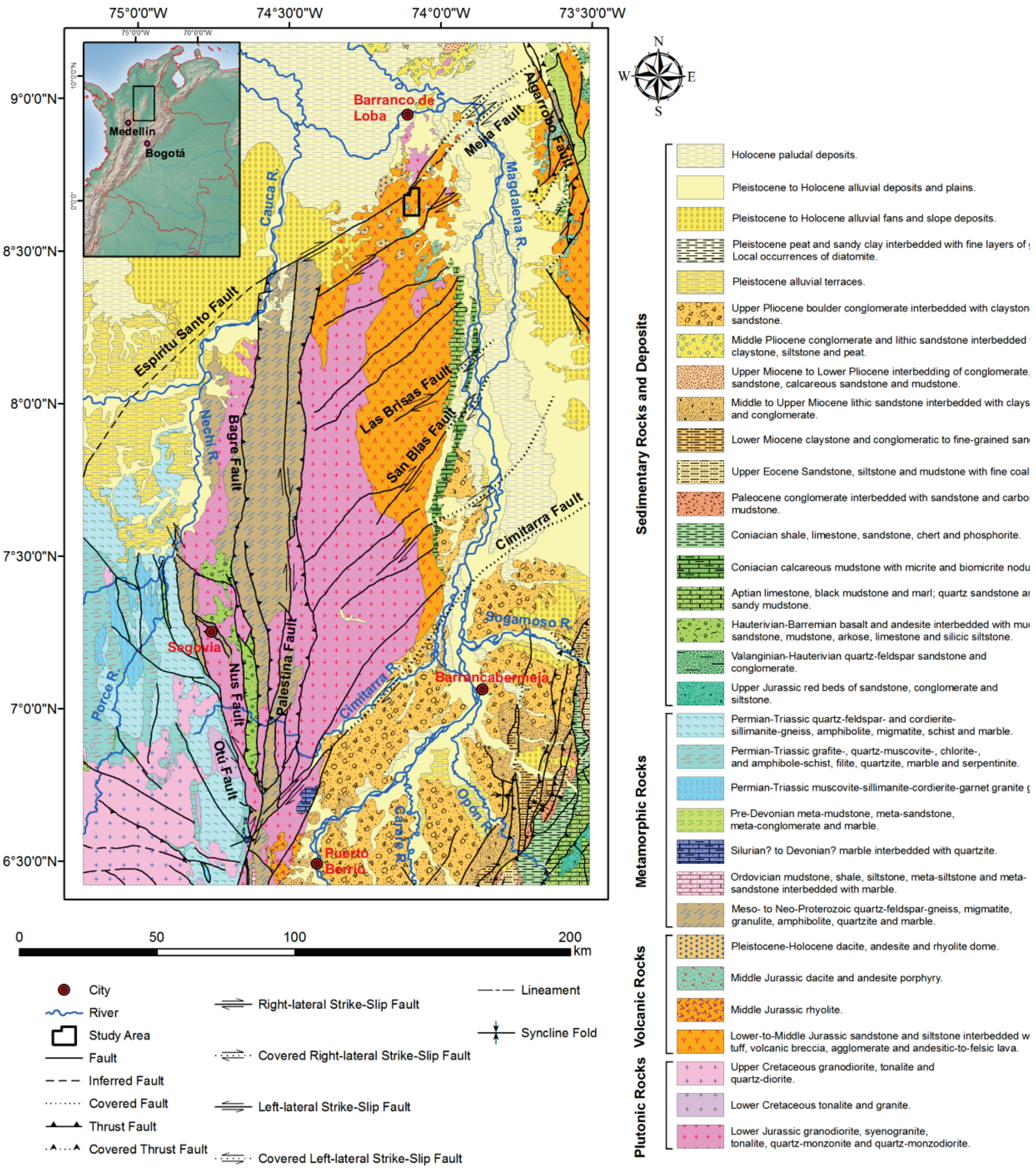

Figure 1 – Regional geological map of the SLR. Modified from INGEOMINAS (2007).

Early to Middle Jurassic volcaniclastic rocks intermediate to felsic in composition were deposited mainly on the western margin of the Chibcha Terrane. These rocks, as well as the pre-Devonian metamorphic basement, were intruded by quartz-dioritic to monzogranitic batholiths that have yielded ages between 130 and 214 Ma (Feininger *et al.*, 1973; Vesga & Barrero, 1978; Sillitoe *et al.*, 1982; McCourt *et al.*, 1984; Jaramillo *et al.*, 1980; Dörr *et al.*, 1995; Cardona *et al.*, 2006) and host important prospects of Au, Ag Cu and Mo mineralizations. The Chibcha Terrane is thought to be separated from the Amazonian Craton to the east by the faults of the Guaicáramo system, while the western boundary between it and the Tahamí Terrane is marked by the Otú-Pericos

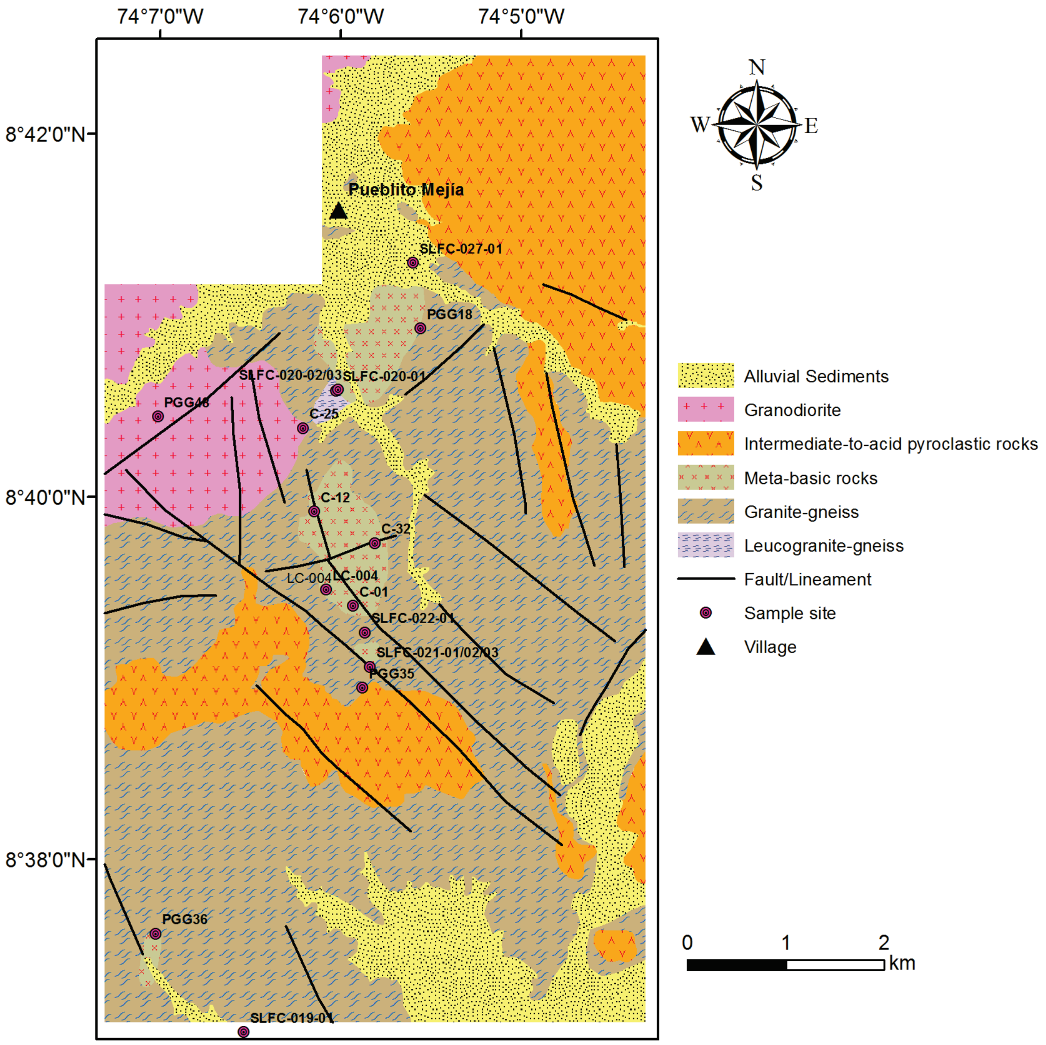

Figure 2 – Geological map of the area of study displaying the location of samples. Position in theSLR as shown in figure 1. Some samples were taken outside this area (see table 1 and table 2).

Fault. The docking of the Chibcha Terrane onto its current position could have taken place during the Late Paleozoic (Restrepo & Toussaint, 1988; Toussaint & Restrepo, 1996).

The SLR is located at the northern end of the Central Cordillera, east to the Otú-Pericos Fault (figure 1), and thus making part of the western border of the Chibcha Terrane. Orthoderived quartz-feldspar gneisses, amphibolites and retrograded mafic granulites grouped into the unit known as the San Lucas Gneiss make up the basement of this region, for which a ID-TIMS ^{207}Pb/^{206}Pb age in zircon close to 1150 Ma has been obtained (INGEOMINAS-UIS, 2006), although Ordóñez-Carmona *et al.* (2009) reported a LA-ICPMS U-Pb age in zircon of *ca.* 1500 Ma. The San Lucas Gneiss is overlain on its northern portion by volcaniclastic rocks composed of tuffs, breccias, agglomerates, sandstones and siltstones of the Noreán Formation, for which an Early to

Middle Jurassic age has been assigned based on stratigraphic relations to other fossil-bearing rocks further south (Bogotá & Aluja, 1981). Granodioritic rocks of the Norosí Batholith, which corresponds to the northern extension of the Segovia Batholith in the department of Antioquia (González, 2001), intrude the former units and have yielded crystallization ages between 160 and 200 Ma (INGEOMINAS-UIS, 2006; Mesz, 2008; Ordóñez-Carmona *et al*., 2009).

Next, the field and petrographic descriptions of the units found within the area of study are presented. For geographical and geological references see figure 1 and figure 2.

Figure 3 – **A**: Banded granite gneiss displaying alternate felsic and mafic layers. **B**: Metamafic intrusive rock cross-cutting banding/foliation of the gneiss.

Figure 4 – **A**: Ptygmatic folding in migmatized (stromatic) mafic rocks. **B**: Diatexitic migmatite derived from mafic rock. Some of melanosome can be seen as rafts of schollen within massive to vein-like leucosome at the center of the picture.

4.2.2. Local geology

4.2.2.1. Granite-gneiss

This group makes up the bulk of the area of study and comprises medium-to-coarse grained rocks ranging from monzo- to syenogranitic in composition. They are leucocratic and display a compositional banding/foliation manifested as alternate light and dark layers, the former being quartz- and feldspar-rich, while the latter are often enriched in biotite and/or amphibole (figure 3A). Locally, the rocks are enriched in potassic feldspar, which imprints a characteristic pinkish color on the rock massifs. In thin section, the mineral paragenesis consists of quartz, microcline, plagioclase, biotite and hornblende, with chlorite commonly replacing the two latter minerals as a result of retrograde reactions in rims and along cleavage planes (figure 5C). Masses of chlorite and/or biotite and hornblende relicts are arranged as narrow strips that give the rock a banded appearance. Opaque minerals commonly consist of magnetite and ilmenite, with small grains of pyrite being rare and apparently derived from hydrothermal alteration along with sericite, clays and epidote. Zircon, allanite and apatite are the most common accessory minerals in these rocks, with titanite associated to chloritized biotite crystals. The texture is mainly relict aphyric, xenoblastic and equigranular, with grain boundaries ranging from lobate to curved. Metamorphic growth is evidenced by poikiloblastic textures of feldspar crystals engulfing small rounded quartz grains (figures 5A and 5D). The quartz commonly displays sutured boundaries, polygonization textures, oriented stretched grains, undulose extinction and local micro-graphic and myrmekitic textures (figures 5A and 5B).

4.2.2.2. Metamafic rocks

Rocks from this group display a fairly similar mineralogy but with variable modal proportions and degrees of recrystallization. They are seen intruding the granite-gneiss cross-cutting its banded structure (figure 3B). Their occurrence is more restricted than that of the granite gneiss, and its recognition is in some instances hindered by migmatization processes that imprint a more leucocratic and, sometimes, even layered aspect, causing confusion with the quartz-feldspathic rocks (figure 4).

In outcrop, one of the rock types (petrographically classified as leuco-norite but referred to as metamonzogabbro hereafter; see section 4.4.1) displays dark tones which turn a little lighter when weathered. However, in thin section the color index of these

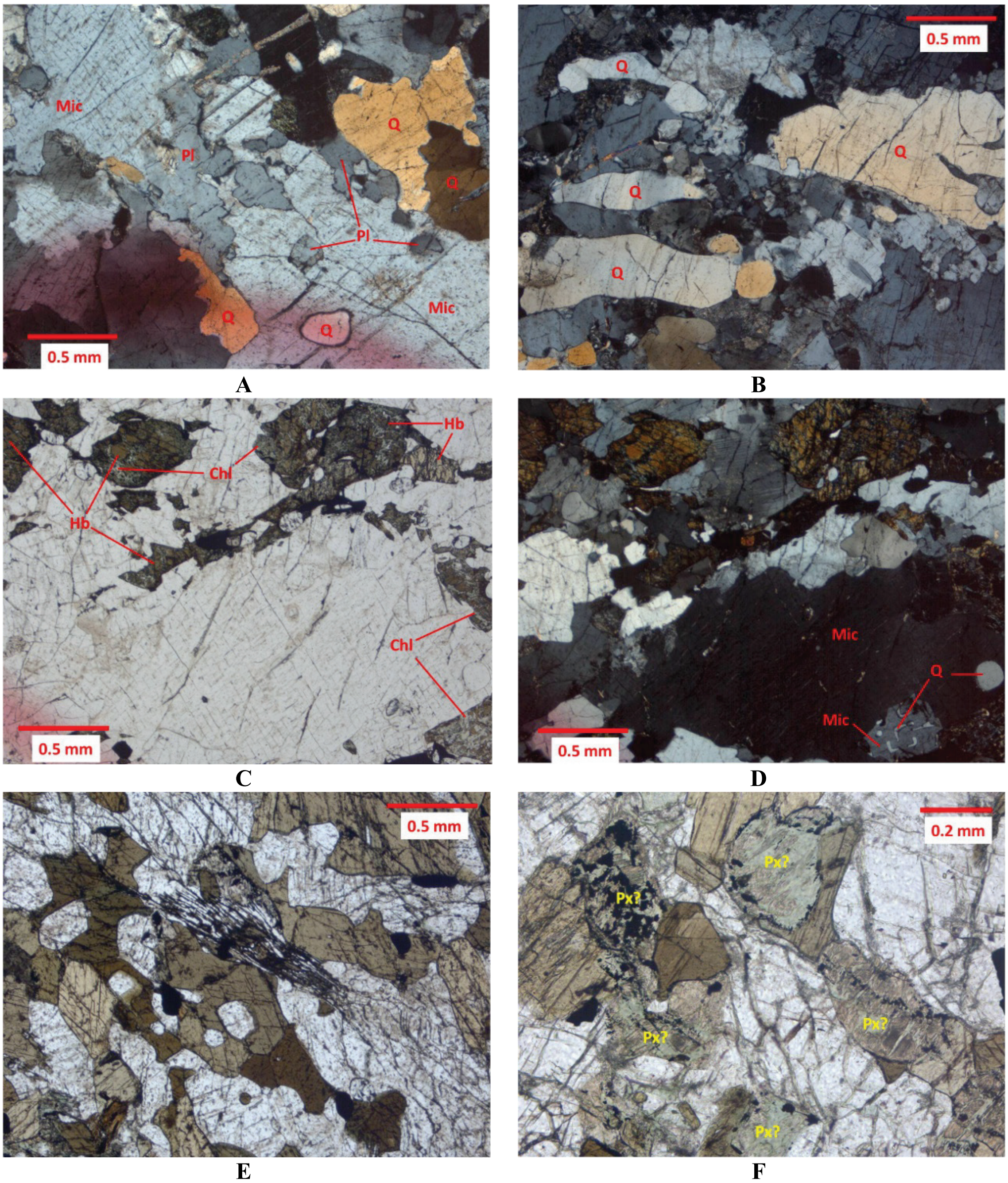

Figure 5 – Photomicrographs of studied rocks. **A**: (CPL) Poikiloblastic microcline engulfing smaller rounded crystals of plagioclase and quartz. Notice the sutured grain boundaries in microcline and quartz (granite-gneiss). **B**: (CPL) Oriented quartz grains in granite-gneiss. **C**: (PPL) Granite-gneiss displaying chlorite forming along cleavage planes and around borders in hornblende. **D**: (CPL) Same field as in C, showing a large poikiloblastic microcline crystal engulfing a rounded quartz grain and a smaller potassic feldspar crystal displaying micro-graphic intergrowth with quartz in the lower portion of the picture. **E**: (PPL) Hornblende-plagioclase amphibolite. Notice the poikiloblastic texture of the hornblende engulfing smaller crystals of plagioclase. A symplectic intergrowth between biotite and quartz can be seen at the center of the picture. Relicts of granoblastic texture (triple joints of crystals) are observed at the left and lower fields of the picture. **F**: (PPL) Possible chloritized pyroxene relicts in hornblende-plagioclase amphibolite. Opaque minerals in and around these relicts are mainly magnetite and ilmenite, but pyrite and minor chalcopyrite were also observed. **Abbreviations**: **Q**=quartz, **Pl**=plagioclase, **Mic**=microcline, **Hb**=hornblende, **Chl**=chlorite, **Px**=pyroxene, **CPL**=cross-polarized light view, **PPL**=plane-polarized light view.

rocks hardly attains 30%. The mineral paragenesis consists of plagioclase, hornblende, biotite, orthopyroxene, clinopyroxene, apatite and Fe-Ti oxides. Hornblende and biotite are commonly sub- to euhedral, display intergrowth relationships and have a tendency to occur at the interstitial spaces between plagioclase grains (figures 7C and 7D). Locally, the ferromagnesian minerals display retrogradation to chlorite, with pyroxenes being more susceptible to this. In particular, the orthopyroxene is the most susceptible phase, always appearing as internally fragmented crystals with accumulation of fine-grained opaque masses along the cracks. Locally, orthopyroxene displays poikiloblastic texture engulfing small lamellae of biotite (figure 7A). Hornblende, in turn, displays poikiloblastic and partial corona textures engulfing both clino- and orthopyroxene crystals (figure 7B). Potassic feldspar is found in low amounts and quartz, which is generally absent, is sometimes found as tiny interstitial crystals or within myrmekitic intergrowths. The textures are xenoblastic and equigranular, preserving what could have been a magmatic cumulate texture, with plagioclase as the cumulus phase and clinopyroxene, hornblende, biotite, apatite and Fe-Ti oxides as the intercumulus phases, although some tiny euhedral crystals of the latter minerals can also be found within larger plagioclase crystals. Despite the poikiloblastic texture shown by some orthopyroxene crystals, it is likely that the mineral had also been part of the magmatic paragenesis, forming the preferred nucleation sites for later metamorphic orthopyroxene. Recrystallization is also recognized by local triple junctions of mafic minerals (figure 7B) and anhedral shapes of the plagioclase which displays sutured grain boundaries. Weak compositional zoning and wedge-shaped twining lamellae are also observed in the latter mineral. Fine-to-medium grained apatite is fairly abundant, making up to 1-2% of the modal composition.

A second rock type is represented by amphibolites which have color indexes between 40 and 50%. One subtype of amphibolite is basically composed of anhedral plagioclase and poikiloblastic hornblende. Although the xenoblastic texture is widespread in this rock, granoblastic texture relicts are locally preserved (figure 5E). There are some instances in which small chloritized grains are observed, which could probably be pyroxene relicts (figure 5F). Less abundantly, some symplectic intergrowths between biotite and quartz can be found in this amphibolite subtype (figure 5E). Fine-grained apatite appears as the main accessory mineral in the rock. Another subtype of amphibolite has a smaller grain size and plagioclase, hornblende and

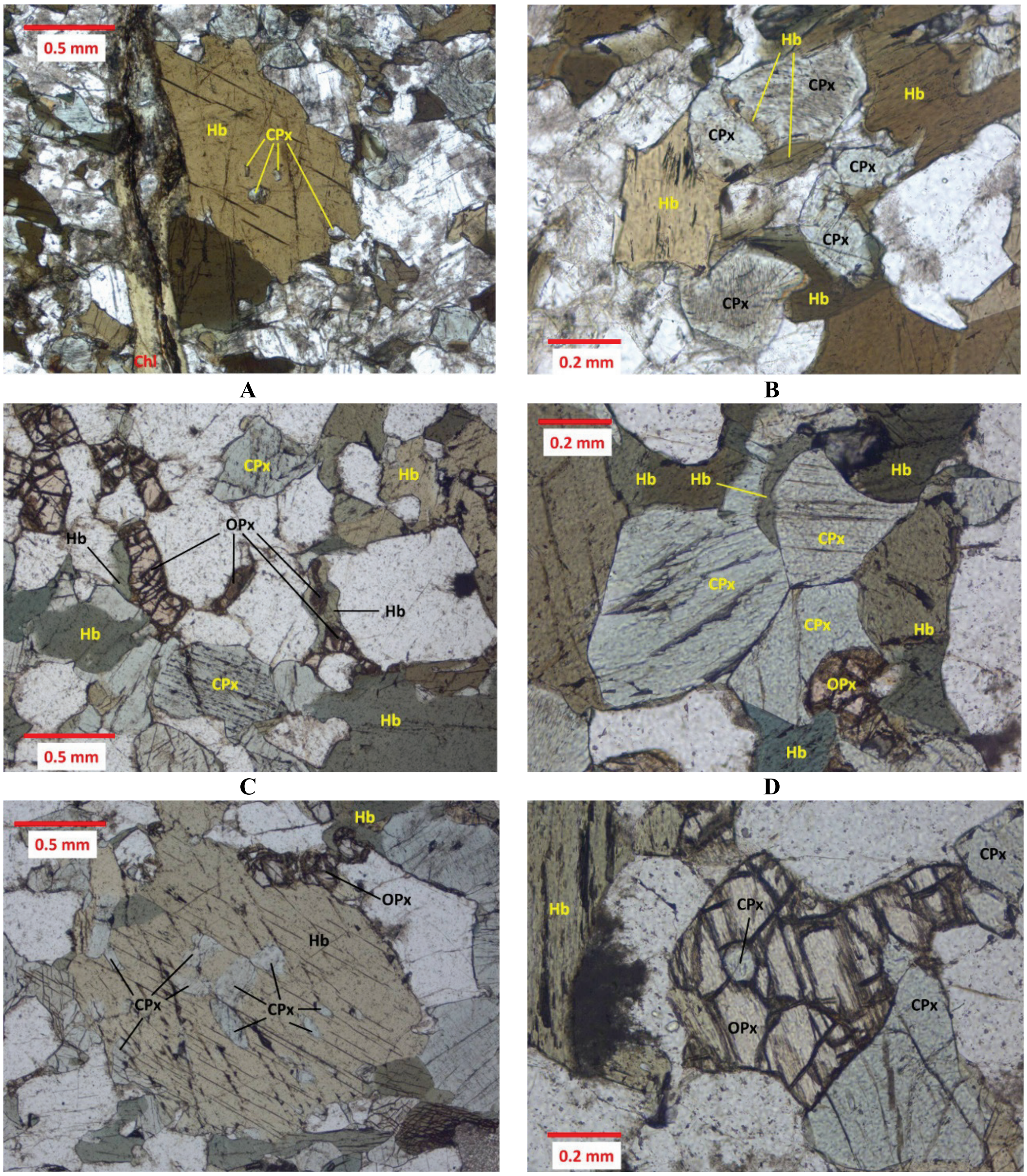

Figure 6 – Photomicrographs of studied rocks. **A**: (PPL) Poikiloblastic hornblende engulfing smaller clinopyroxene crystals in hornblende-plagioclase-clinopyroxene amphibolite. A chlorite vein is seen cutting the rock vertically at center-left portion of the picture. **B**: (PPL) Same rock as in A. Corona-like textures of hornblende around clinopyroxene crystals. **C**: (PPL) Corona-like textures of hornblende around clino- and orthopyroxene crystals in retrograded mafic granulite. **D**: (PPL) Relict granoblastic texture of clinopyroxene in retrograded mafic granulite. Hornblende forms corona-like textures around clino- and orthopyroxene. **E**: (PPL) Poikiloblastic hornblende engulfing clinopyroxene in retrograded mafic granulite. Hornblende is also forming corona-like textures around orthopyroxene at the upper portion of the picture. **F**: (PPL) Poikiloblastic orthopyroxene engulfing a clinopyroxene crystal in retrograded mafic granulite. **Abbreviations**: **Hb**=hornblende, **Chl**=chlorite, **CPx**=clinopyroxene, **OPx**=orthopyroxene, **PPL**=plane-polarized light view.

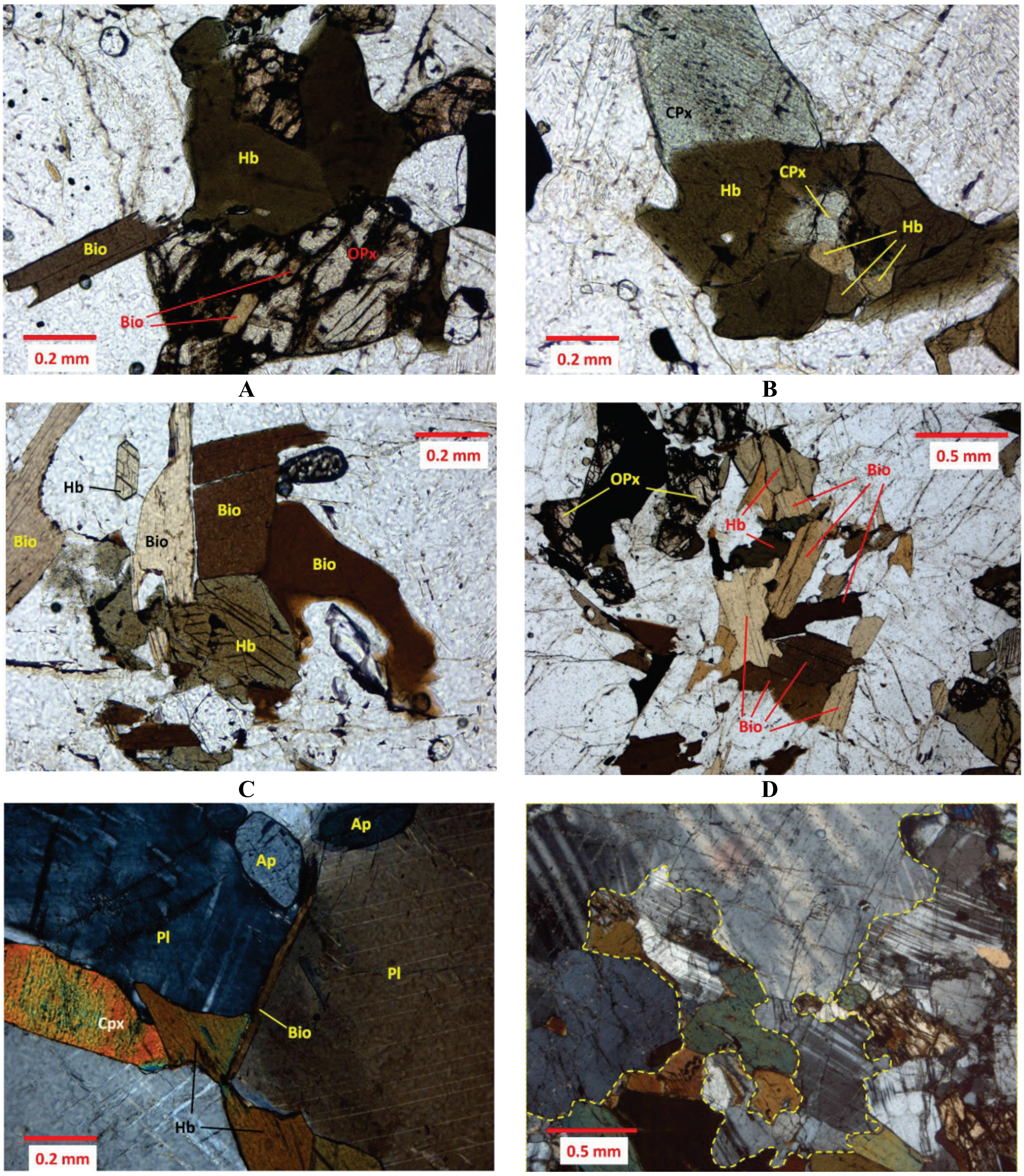

A B C D E F

Figure 7 – Photomicrographs of studied rocks. **A**: (PPL) Poikiloblastic orthopyroxene engulfing small biotite laths (metamonzogabbro). **B**: (PPL) Poikiloblastic hornblende engulfing a clinopyroxene grain and displaying granoblastic texture at the lower portion of the picture (metamonzogabbro). **C**: (PPL) Intergrowth between hornblende and biotite forming a triple junction. A small euhedral crystal of hornblende is shown at the upper-left corner of the picture (metamonzogabbro). **D**: (PPL) Intergrown crystals of subhedral biotite and anhedral hornblende in metamonzogabbro. **E**: (CPL) Small biotite lamella grown interstitially between two plagioclase grains along with hornblende and clinopyroxene (metamonzogabbro). **F**: (CPL) Migmatized granulite. The migmatitic front (leucosome) composed in this view by coarse-grained plagioclase can be seen at the upper-half of the picture, separated by a yellow discontinuous line from the paleosome composed by hornblende, plagioclase, clinopyroxene, orthopyroxene. Small hornblende "rafts" can be observed within the leucosome at the left portion of the picture. **Abbreviations**: **Hb**=hornblende, **Bio**=biotite, **CPx**=clinopyroxene, **OPx**=orthopyroxene, **PL**=plagioclase, **Ap**=apatite, **CPL**=cross-polarized light view, **PPL**=plane-polarized light view.

clinopyroxene as essential minerals. The general texture of the rock is xenoblastic, with hornblende displaying a poikiloblastic texture defined by rounded clinopyroxene inclusions within its interior or defining partial corona textures around the latter (figures 6A and 6B). Some hornblende crystals seem also to be part of the engulfed phases, which possibly indicates the existence of a pre-metamorphic generation of hornblende as deduced also from small hornblende inclusions in poikiloblastic orthopyroxenes of the metamonzogabbro (see above). Chlorite hydrothermal veinlets are commonly found cutting these rocks.

The third rock type consists of retrograded mafic granulite composed of plagioclase, hornblende, clinopyroxene and orthopyroxene, with null or too little amounts of Fe-Ti oxides. The general texture of the rock is xenoblastic with curved grain boundaries. Although poikiloblastic texture can be found in some orthopyroxenes (figure 6F), poikiloblastic and partial corona textures of hornblende engulfing both clino- and orthopyroxene can also be observed (figures 6C - 6E). Relicts of granoblastic texture are widespread (figure 6D) and plagioclase is commonly equigranular, anhedral and displays wedge-shaped twining lamellae.

When migmatized, the metamafic rocks mentioned above display melanosomes which are very similar to the original high-grade rocks (*i.e.*, coinciding with the paleosome). In one of the samples a stromatic-phlebitic structure can be observed in a migmatized granulite, which in thin section consists of coarse-grained layers composed of quartz, plagioclase and biotite (leucosome) cutting the original mafic paleosome of generally smaller grain size (figure 7F). "Rafts" of the original minerals belonging to granulite are in some instances preserved within the leucosome (figures 8A and 8B). In the latter case, those minerals display accentuated alteration and corrosion, being this more evident in the orthopyroxene which transforms into chlorite and Fe oxides along grain boundaries and internal cracks.

4.2.2.3.Leucogranite-gneiss

This group of rocks is rather rare in the studied area, having been found in one single outcrop; therefore this unit was not studied in detail. These rocks display a foliation defined by a parallel arrangement of biotite strips and strong folding. Local hydrothermal alteration is evidenced by coarse grained epidote and potassic feldspar around siliceous veinlets. This gneiss seems to be intruded by the metamonzogabbro described above. In thin section, it displays xenoblastic texture and is composed of quartz, plagioclase, potassic feldspar and biotite, with widespread epidote formed by hydrothermal alteration. Mineralogically, the rock displays a granodioritic-tonalitic composition, with a color index no greater than 5%. Recrystallization is evidenced by poikiloblastic texture of some potassic feldspar and plagioclase grains and sutured grain boundaries in quartz and feldspar. Myrmekitic textures are common, and the quartz can also be observed displaying polygonization and undulose extinction. Biotite displays irregular-to-lamellar habits and moderate-to-strong chloritization along cleavage planes.

4.2.2.4. Volcanic rocks

Since the Mesozoic volcanic processes were not part of the main focus of this work, these rocks were not characterized in detail and only a general mention is given here. These rocks range from intermediate to rhyolitic in composition, and are represented mainly by tuffs, breccias, agglomerates and ignimbrites indicative of explosive activity. Lavic rocks, although present, seem to be subordinate to the former group. The texture is commonly porphyritic, with the coarse-grained population composed of phenocrysts and crystal and rock fragments. The groundmass is commonly hyalocrystalline and in some instances very small oriented feldspar laths define a trachytoid texture. Phenocrysts are composed of clinopyroxene and plagioclase in the more mafic members, while plagioclase and quartz dominate the more silicic rocks. Fragments commonly include plagioclase, quartz and pumice, although zircon and chloritized mafic minerals are sometimes observed. The volcanic rocks are deposited on the metamorphic basement described above, and dacitic dykes can also be found cutting those rocks at some locations.

4.2.2.5. Granodiorite

This unit, which intrude all the metamorphic and volcanic rocks described above, commonly display mafic enclaves at hand specimen scale which are indicative of magma mingling. It is coarse-grained, undeformed and have quartz, plagioclase, potassic feldspar, biotite and hornblende as essential minerals. Zircon and apatite constitute the accessory mineral assemblage. The general texture is aphyric, subidiomorphic and equigranular, although some porphyritic-like textures can be locally seen with medium-grained quartz composing the groundmass between larger subhedral-to-euhedral crystals of feldspars, biotite and hornblende (figure 8D). Plagioclase commonly occurs as large crystals displaying oscillating zoning and moderate to strong argillization and sericitization. Potassic feldspar crystals tend to be subhedral and are

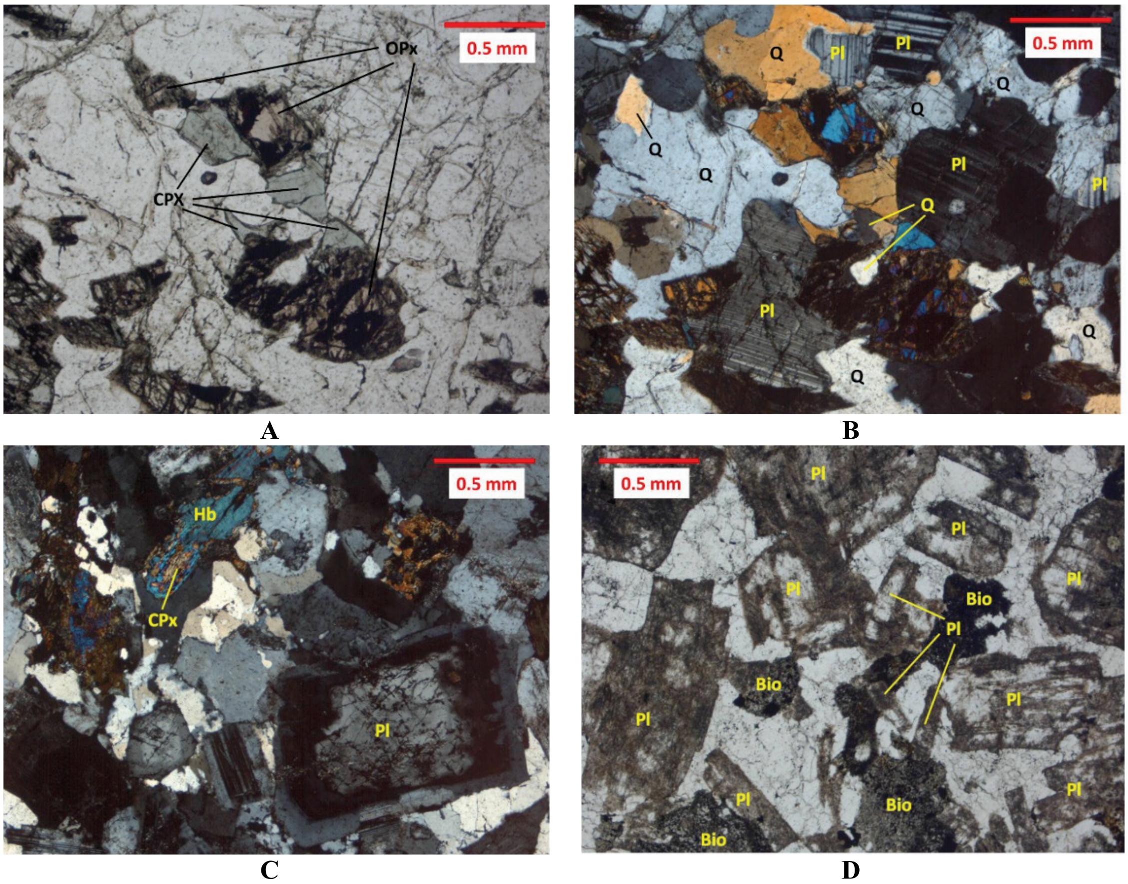

Figure 8 – Photomicrographs of studied rocks. **A** (PPL) and **B** (CPL): Clino- and orthopyroxene “rafts” within quartz and plagioclase leucosome in migmatized granulite. Breakdown of the orthopyroxene can be recognized by the numerous opaque grains forming within it. **C**: (CPL) Clinopyroxene core preserved within hornblende crystal in granodiorite. To the right, a large, euhedral plagioclase crystal displaying oscillating zoning can be observed. **D**: (PPL) Argillized euhedral plagioclase crystals and chloritized biotite in granodiorite. The clear matrix between larger crystals corresponds to fine-grained anhedral quartz defining a rather porphyritic texture in the rock. Notice the numerous small opaque grains (probably ilmenite) formed as an alteration product of the biotite. **Abbreviations**: **Hb**=hornblende, **Bio**=biotite, **Q**=quartz, **CPx**=clinopyroxene, **OPx**=orthopyroxene, **PL**=plagioclase, **CPL**=cross-polarized light view, **PPL**=plane-polarized light view.

easily recognized by their perthitic blebs and weaker alteration. Hornblende can be subhedral or skeletal with inclusions of opaques, quartz and apatite. This mineral often displays chloritization and colorless cores of clinopyroxene (figure 8C) with fairly irregular boundaries, which indicates an unequilibrated reaction rim. Biotite is generally skeletal and poikilitic, engulfing smaller crystals of plagioclase, opaques and apatite. It displays variable chloritization, and as a result of this alteration numerous small opaque grains (probably ilmenite) accumulate internally within the chlorite. It is common to observe intergrowths between hornblende and biotite, which indicates equilibrium crystallization between these minerals. Local hydrothermal alteration is recognized by formation of epidote and muscovite associated to the biotite. The quartz constitutes a late phase characterized by small anhedral grains grown interstitially between larger crystals of other minerals. Myrmekitic intergrowths with plagioclase are quite common. Opaque minerals constitute 1-2% of the modal composition and consist of anhedral grains of magnetite displaying exsolution lamellae of ilmenite.

4.2.2.6.Gold-bearing quartz veins

They are widespread within the studied area and consist of variable proportions of pyrite, galena, chalcopyrite and sphalerite accompanied by quartz as main gangue mineral, and subordinated feldspar, chlorite and calcite. At the locality of Culo-Alzao (further south of the area of study), massive chalcopyrite engulfs hessite (Ag_2Te) cores rimmed by tetradymite (Bi_2Te_2S) coronas. The latter telluride can also be seen filling thin cracks in the chalcopyrite. The texture of the ore ranges from massive to brecciated and the vein thickness varies between a few centimeters up to 1 m. Small gold grains a few micrometers in size and fineness between 590 and 670 (with silver as main companion) can be found within the sulfides (mainly pyrite). Associated hydrothermal alterations correspond to sericitization and silicification within the proximal zones near the veins (typically a few meters wide), while chloritization and epidotization dominate the distal alteration assemblages. The veins display a remarkable structural control, following both regional and local structures trending NNE-SSW and ESE-WNW. They correspond in several instances to shear-zone fillings and are found cutting all the above mentioned metamorphic, volcanic and plutonic units.

4.3. ANALYTICAL METHODS

4.3.1. Major and trace element geochemistry

Chemical analyses of rock powder were performed by AcmeLabs Ltd. following 4A and 4B routines. The former involved ICP-AES analysis of major and minor elements after lithium metaborate/tetraborate fusion and dilute HNO_3 digestion. In routine 4B trace elements were analyzed by ICP-MS following the same preparation as in 4A and digestion in aqua regia of an additional separate split.

4.3.2. U-Pb geochronology

The methodology and equipment set-up used for U-Pb geochronology closely followed those presented by Bühn *et al.* (2009) to whom the reader is referred for further details. Geochronological U-Pb analyses were carried out at the geochronology laboratory of the University of Brasília, using a Thermo Finnigan Neptune multicollector inductively coupled plasma mass spectrometer. The input of mineral substance into the spectrometer was achieved by means of the laser ablation technique, using a New Wave 213µm Nd-YAG solid state laser. The sampling conditions of the latter varied according to the sample characteristics as to optimize isotope signals, with a beam diameter of 10-30 µm and a laser energy ranging from 0.5 to 1.2 J/cm2 at a frequency of 10 Hz. The samples were inserted into a He-flushed laser chamber maintaining the gas flux between 0.35 and 0.45 l/min. Removing of ^{204}Hg from the He flux was attained by passing the gas through glass tubes containing gold-coated quartz particles intended to minimize the isobaric interference with ^{204}Pb, thus allowing the application of common lead corrections where necessary. After passing through argon-sustained plasma, the ablated material was then conveyed to the detector arrangement which for this study consisted of six ion counters or multichannel ion counters (MICs). For standard and sample analysis, the signals were collected in a single block with 40 cycles of 1.049 s each, starting the reading of the signals after the latter had attained their maximum following the onset of ablation.

The standard-sample bracketing technique was applied by analyzing one standard point and one blank every four or eight sample points, thus accounting for instrumental drift. The international standard used here was the GJ-1 zircon, provided by the ARC National Key Centre for Geochemical Evolution and Metallogeny of Continents (GEMOC), Australia. Its reference ages after Jackson *et al*. (2004) are: ^{207}Pb/^{206}Pb age = 608.6 ± 1.1 Ma, ^{206}Pb/^{238}U age = 600.4 ± 1.8 Ma, ^{207}Pb/^{235}U age = 602.1 ± 3.0 Ma. Data reduction was achieved using a spreadsheet set up at the geochronology laboratory of the Brasília University; this spreadsheet allows evaluating the isotope ratios of the 40 cycles on a 2σ rejection basis. The corrected ratios and associated calculated ages were then displayed using Isoplot 3 (Ludwig, 2009).

4.3.3. *Nd and Sr isotope geochemistry*

All the Sm, Nd and Sr isotope analysis were performed at the Geochronology Laboratory of the University of Brasília. The analytical procedures applied in this study for measuring the ^{147}Sm/^{144}Nd and ^{143}Nd/^{144}Nd isotope ratios were the same as those described by Gioia & Pimentel (2000). Rock samples were ground down to powder and added with ^{149}Sm and ^{150}Nd spike solutions. Separation of Sm from Nd was accomplished by using cation exchange columns, after which obtained fractions were evaporated with two drops of 0.025N H_3PO_4. The residue was dissolved in 1 µl of 5% distilled HNO_3 and loaded onto a double Re filament assembly. The mass spectrometer used was a Finnigan MAT 262 with 7 collectors with analyses accomplished in static mode. Uncertainties for $^{147}Sm/^{144}Nd$ and $^{143}Nd/^{144}Nd$ ratios were better than ±0.2% (2σ) and ±0.0045% (2σ), respectively, based on analysis of BHVO-1 international rock standard. The $^{143}Nd/^{144}Nd$ ratio was normalized using $^{146}Nd/^{144}Nd=0.7219$ and the employed decay constant was 6.54×10^{-12} y^{-1} (Lugmair & Marti, 1978).

For the Sr isotope analyses, the methodology employed was that of Gioia *et al.* (1999). After acid digestion and separation in cation exchange columns, the Sr-bearing fractions were deposited along with 1 µl of H_3PO_4 onto a Ta filament of a Finnigan MAT 262 mass spectrometer. Based on analysis of the NBS987 international standard, $^{87}Sr/^{86}Sr$ ratio uncertainties were better than ±0.0036 % (2σ). The $^{87}Rb/^{86}Sr$ ratio was calculated from the Rb and Sr concentrations reported in the trace element whole-rock analysis using the formula:

$$ {}^{87}\mathrm{Rb}\big/{}^{86}\mathrm{Sr} = \frac{\mathrm{Rb} * \mathrm{Ab.}\,{}^{87}\mathrm{Rb} * \mathrm{A.w.Sr}}{\mathrm{Sr} * \mathrm{Ab.}\,{}^{86}\mathrm{Sr} * \mathrm{A.w.Rb}} $$

Where:

Rb = Rb concentration from trace element analysis.

Ab.^{87}Rb = abundance of ^{87}Rb (equal to 27.835 % according to Steiger & Jäger; 1977).

A.w.Sr = atomic weight of Sr recalculated for each sample from ^{84}Sr, ^{86}Sr, ^{87}Sr and ^{88}Sr abundances as calculated from $^{86}Sr/^{88}Sr=0.1194$ and $^{84}Sr/^{86}Sr=0.056584$ ratios (Steiger & Jäger, 1977).

Sr = Sr concentration from trace element analysis.

Ab.^{86}Sr = abundance of ^{86}Sr recalculated for each sample from its $^{87}Sr/^{86}Sr$ ratio results and Steiger & Jäger (1977) $^{86}Sr/^{88}Sr$ and $^{84}Sr/^{86}Sr$ ratios.

A.w.Rb = atomic weight of Rb (equal to 85.46776 a.m.u.).

The Rb decay constant employed was that from Nebel *et al.* (2011) with a value of 1.393×10-11 y^{-1}.

4.4. RESULTS

4.4.1. Geochemistry

Results of major and trace element analysis are summarized in table 1. Granite-gneiss displays high SiO_2 values ranging between 65 and 73 wt.% and total alkalis (Na_2O+K_2O) between 7.2 and 8.7 wt.%. When plotted in the P-Q diagram of Debon & Le Fort (1982) these rocks show compositions between adamellite (or monzogranite, as preferred by Le Maitre *et al.*, 2002) and more alkaline granite (figure 9B) reflecting enrichments in Na_2O and K_2O which grant an alkali-calcic (or nearly so) character to this unit (figure 10B). Samples 021-03 and JS-020 have a metaluminous character as evidenced by Shand's A/NK values > 1 and A/CNK < 1 (Manniar & Piccoli, 1989), while samples 021-01 and 021-02 fall within the field of peraluminous rocks (figure 10A). Positive values of feldspathoid-silica saturation index (Frost & Frost, 2008) for these rocks imply a silica-saturated character, which is evident from the abundant quartz observed during petrographic analysis. In general, the granite-gneiss is enriched in REE and incompatible trace elements (table 1; figure 12A). Owing to this behavior, the granite-gneiss plots in the within-plate granite field of the Nb vs. Y diagrams of Pearce *et al.* (1984; figure 10D). This feature, along with the high values of Ga/Al and Zr+Nb+Y+Ce (figure 10E) allows classifying the protolith of the granite-gneiss as an A-type granite following the geochemical criteria of Whalen *et al.* (1987). Location of these samples within the anomalous and normal granite fields of El Bouseily & El Sokkary (1975) indicate that the high amounts of incompatible elements are not likely to be the result of strong magmatic differentiation (figure 11C). The granite-gneiss also displays high Fe* values, falling within or at the boundary of the field of ferroan granites (figure 10C); this is an important characteristic of most A-type granites (Frost *et al.*, 2001). When plotted in the ASI vs. MgO diagram of Bilal & Giret (1999) the granite-gneiss shows a distribution of the samples which is intermediate between alkaline-anorogenic and calc-alkaline orogenic trend groups (figure 11A). In terms of MgO/TiO_2 ratio, these rocks display values between 0.93 and 1.75 and define a nearly linear arrange in the TiO_2 vs. MgO diagram (figure 11B). However, the highest MgO/TiO_2 ratio of 1.75 which belongs to sample 021-03 could also be related to slight Mg enrichment caused by metasomatic fluids; this is consistent with that sample falling within the "anomalous granite" field of figure 11C, where granites disturbed by metasomatic processes usually plot (El Bouseily & El Sokkary, 1975). The MgO/TiO_2

Table 1 – Major and trace element whole-rock data. Samples JS-020 and LC-004 are from Mesz (2008) and were included here for comparative purposes. These samples were analyzed by X-ray fluorescence. Major oxide values are in weight percent, while trace elements are reported in ppm.

	Granite-gneiss				Amphibolite	Metamonzogabbro			Granodiorite	
Element	**021-01**	**021-02**	**021-03**	**JS-020**	**005-01**	**020-02**	**020-03**	**LC-004**	**029-01**	**030-02**
SiO_2	72.31	73.19	64.90	68.58	50.49	56.19	53.77	48.56	62.85	61.61
TiO_2	0.50	0.28	0.83	0.55	1.69	1.34	1.53	1.50	0.66	0.70
Al_2O_3	12.36	12.76	14.11	14.15	14.00	19.33	19.05	14.35	15.28	15.67
Fe_2O_3	3.30	2.99	5.87	4.29	10.63	5.85	7.17	15.33	5.58	6.01
MnO	0.03	0.02	0.07	0.06	0.23	0.08	0.11	0.27	0.08	0.10
MgO	0.76	0.26	1.45	0.92	7.27	2.57	2.80	3.91	2.67	2.66
CaO	0.70	0.35	3.58	2.50	7.84	6.64	7.40	7.23	4.87	5.01
Na_2O	2.34	2.56	3.18	3.21	4.06	4.85	5.02	3.41	2.93	3.19
K_2O	5.73	6.09	4.03	4.45	0.90	1.79	1.31	1.10	3.16	3.08
P_2O_5	0.09	0.03	0.20	0.16	0.60	0.42	0.50	0.50	0.12	0.14
Cr_2O_3	0.00	0.00	0.01	0.00	0.04	0.00	0.00	0.00	0.01	0.01
LOI	1.60	1.10	1.50		1.90	0.70	1.10		1.50	1.60
TOT/C	0.12	0.04	0.19		0.11	0.02				
TOT/S			0.05							
Sum	99.73	99.65	99.70	98.86	99.69	99.74	99.72	96.14	99.73	99.75
A/CNK	1.09	1.12	0.88	0.97					0.89	0.89
$FeO^t/(FeOt+MgO)$	0.80	0.91	0.78	0.81	0.57	0.67	0.70	0.78	0.65	0.67
La	111.40	96.20	60.10		27.20	19.10	22.50		23.70	22.90
Ce	210.60	197.00	125.40	169.30	66.00	42.50	53.60	40.30	46.90	49.00
Pr	22.87	23.50	15.33		8.93	5.48	7.46		5.96	5.84
Nd	76.60	82.40	58.50	72.99	36.30	21.90	31.70	28.33	23.20	22.80
Sm	13.86	16.44	11.93	13.17	7.55	4.42	6.77	6.22	4.44	4.52
Eu	1.19	2.02	1.95		2.18	1.38	1.66		0.87	0.96
Gd	13.17	14.84	11.66		7.21	3.98	6.27		4.51	4.41
Tb	2.22	2.44	1.87		1.03	0.57	0.95		0.69	0.68
Dy	13.90	13.79	11.34		5.66	3.08	5.17		3.91	4.23
Ho	2.88	2.89	2.28		1.11	0.57	0.97		0.85	0.83
Er	8.87	8.28	6.30		3.26	1.68	2.94		2.53	2.51
Tm	1.41	1.22	0.94		0.43	0.23	0.43		0.37	0.39
Yb	9.00	7.76	5.80		2.89	1.53	2.64		2.41	2.46
Lu	1.35	1.14	0.88		0.42	0.22	0.39		0.38	0.37

Table 1 – (continued).

	Granite-gneiss				Amphibolite	Metamonzogabbro			Granodiorite	
Element	**021-01**	**021-02**	**021-03**	**JS-020**	**005-01**	**020-02**	**020-03**	**LC-004**	**029-01**	**030-02**
Ba	473.00	798.00	782.00	1084.70	315.00	511.00	374.00	424.50	729.00	729.00
Be	1.00	4.00	5.00				3.00			
Cs	0.50	1.10	0.70		0.20	0.60	0.20		1.30	1.80
Ga	17.30	21.40	20.50	20.80	20.30	20.80	24.00	19.80	16.10	17.00
Hf	11.40	15.60	11.00		4.70	3.90	2.40		6.30	4.50
Nb	21.10	18.10	18.80	25.20	17.60	10.60	15.00	13.10	6.20	6.30
Rb	237.40	221.40	113.90	133.80	7.80	48.40	16.40	12.11	93.30	101.10
Sc	6.00	4.00	13.00		24.00	11.00	18.00		16.00	18.00
Sn	10.00	6.00	2.00		1.00		1.00		2.00	
Sr	76.70	93.00	200.90	231.30	401.40	657.50	646.60	367.40	282.10	327.70
Ta	2.10	1.50	1.40		0.90	0.90	1.30		0.70	0.50
Th	70.00	26.90	7.70	8.90	0.60	1.60	1.40	2.30	6.40	4.90
U	10.30	3.70	3.40		0.40	0.60	0.50		1.90	1.50
V	27.00		56.00	37.10	171.00	116.00	264.00	197.20	125.00	126.00
Y	84.00	76.70	60.80	57.40	31.40	17.00	29.00	32.90	25.10	24.70
Zr	319.40	524.10	393.60	340.70	187.50	147.90	92.20	79.40	218.70	166.60
Ni	5.30	1.60	12.60	5.40	58.10	7.40	3.10	4.90	10.30	9.00
Pb	5.20	4.50	1.90	18.80	0.60	2.90	2.20	11.30	3.30	7.40
Zn	56.00	45.00	62.00	69.00	66.00	38.00	59.00	98.00	33.00	44.00

SAMPLE LOCATIONS:
021-01: 8° 38' 53.6791" N; 74° 05' 37.7262" W
021-02: 8° 38' 53.6791" N; 74° 05' 37.7262" W
021-03: 8° 38' 53.6791" N; 74° 05' 37.7262" W
JS-020: 8° 58' 14.4091" N; 74° 02' 2.9000" W
020-02: 8° 40' 25.2415" N; 74° 05' 48.8510" W
020-03: 8° 40' 25.2415" N; 74° 05' 48.8510" W
LC-004: 8° 39' 19.1760" N; 74° 05' 52.3556" W
005-01: 8° 35' 47.1669" N; 74° 05' 58.1928" W
029-01: 8° 43' 9.8463" N; 74° 05' 45.8482" W
030-02: 8° 47' 20.0881" N; 74° 05' 59.8303" W

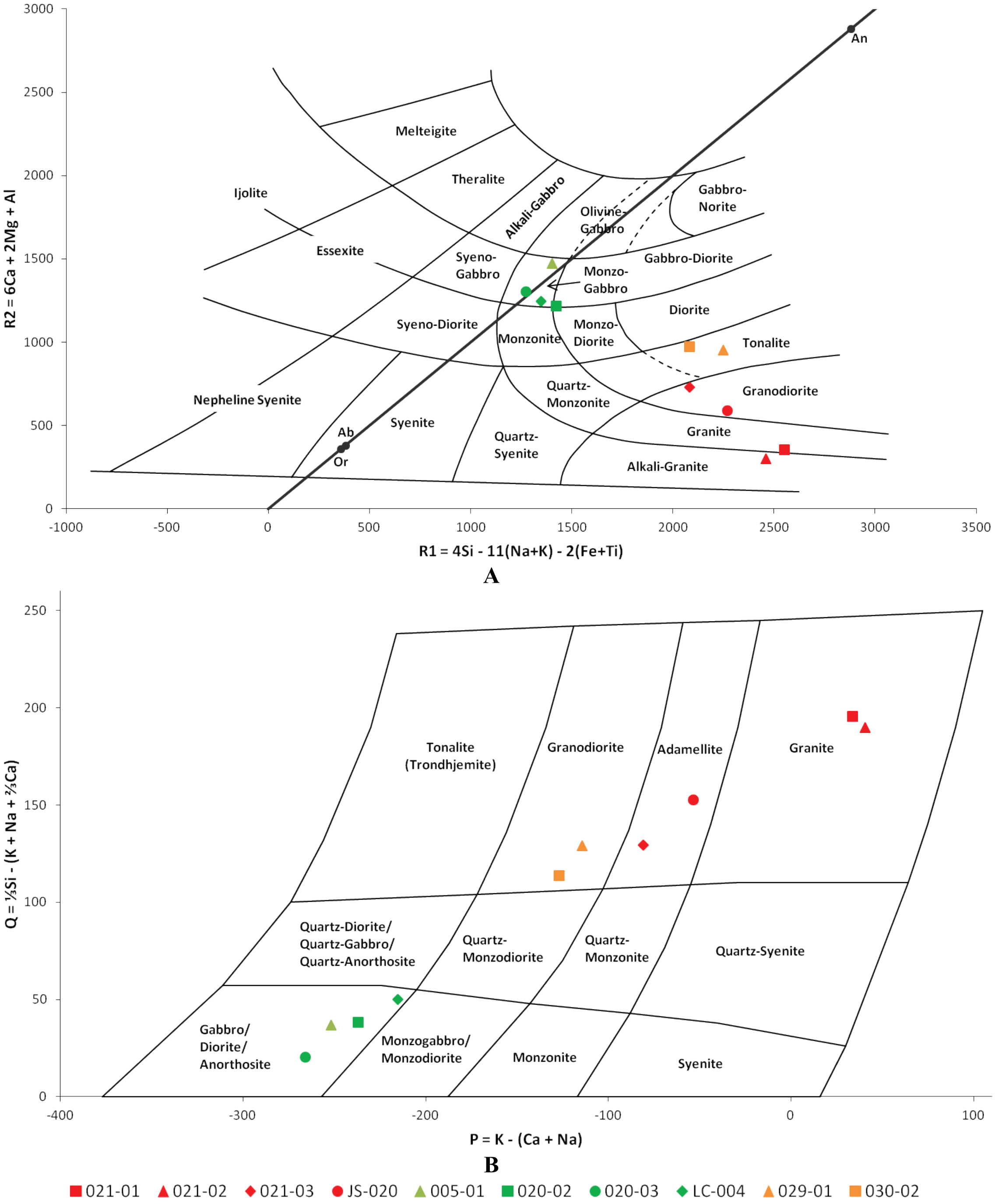

Figure 9 – **A**: Projection of whole-rock compositions on the R1-R2 space of De La Roche *et al.* (1980) showing the transitional nature and relatively homogeneous chemistry of the metamafic rocks. **B**: P-Q space of Debon & Le Fort (1982) displaying the compositional variation of the granitic rocks. Color key: red=granite-gneisses; green=metamafic rocks; orange=granodiorites.

figures also suggest a transitional tectonic setting between anorogenic and subduction-related according to the criteria of Bilal & Giret (1999). Major element-based discriminant functions of Agrawal (1995) yield D_1, R_1, D_2 and R_2 values ranging between -0.47 and 1.46, -1.24 and 1.60, -2.22 and 1.47 and -1.59 and 2.00, respectively, which indicates a post-orogenic setting of formation for the granite-gneiss, except for

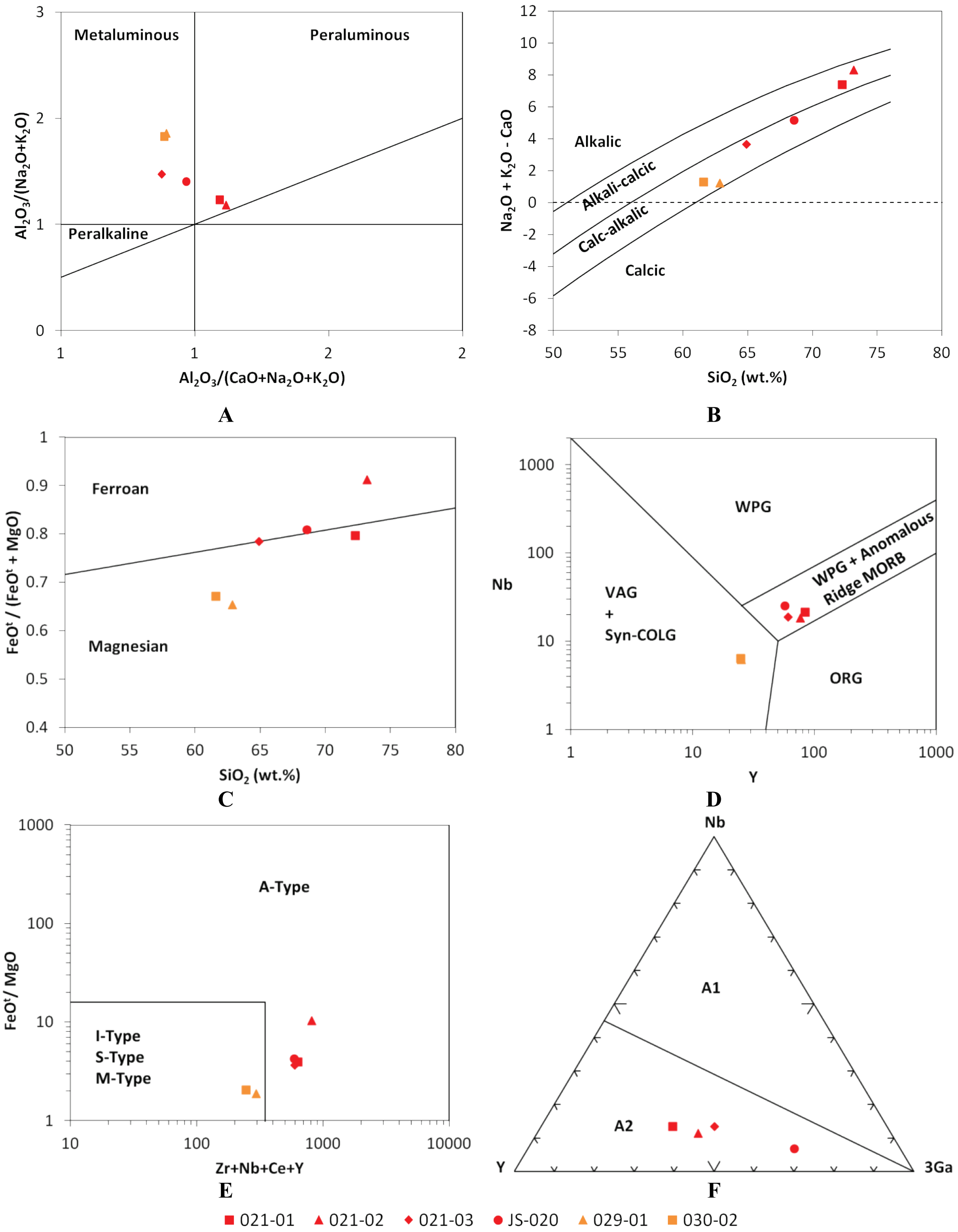

Figure 10 – Major and trace element geochemical characteristics of granitic rocks. **A**: Diagram of Shand's A/NK vs A/CNK of Maniar & Piccoli (1989). All of the samples display positive feldspathoid-silica saturation index (FSSI; Frost & Frost, 2008). **B**: Modified alkali-lime index (MALI=Na_2O+K_2O-CaO) vs. SiO_2 diagram of Frost *et al.* (2001). Granite-gneiss tends to be alkali-calcic in nature, while granodiorite is essentially calc-alkalic. **C**: Diagram of $Fe^*=FeO^t/(FeO^t+MgO)$ vs. SiO_2 of Frost *et al.* (2001) showing the ferroan and magnesian affinities of the granite-gneiss and granodiorite, respectively. **D**: Nb vs. Y tectonic discrimination diagram of Pearce *et al.* (1984) suggesting a within-plate environment of formation for the protolith of the granite gneiss. Notice that post-collisional granites also plot near the triple junction between the WPG, VAG+Syn-COLG and ORG fields (Pearce, 1996). **E**: FeO^*/MgO vs. Zr+Nb+Ce+Y diagram of Whalen *et al.* (1987) suggesting an A-type nature for the protolith of the granite-gneiss. **F**: The A-type granite-gneiss is further classified into the A_2 subtype, according to the Y-Nb-3Ga ternary diagram of Eby (1992). Color key as in figure 9.

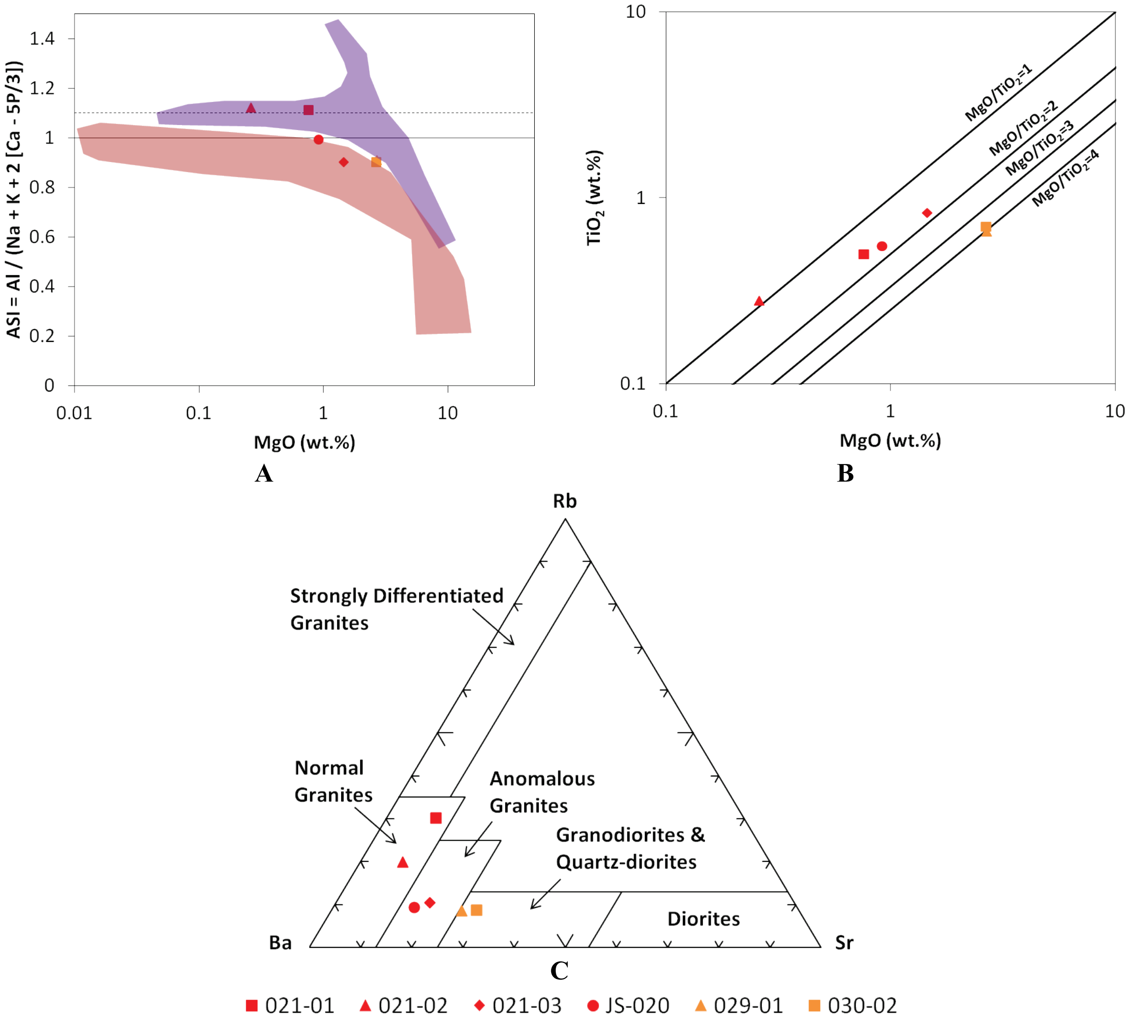

Figure 11 – Major and trace element geochemical characteristics of granitic rocks. **A**: ASI vs. MgO diagram. Upper shaded field: Calc-alkaline differentiation trends of Hercynian orogenic suites from France and I- and S-type granite suites from the Lachland Fold Belt, Australia; Lower shaded field: differentiation trends of alkaline anorogenic suites from Niger and Kerguelen Islands. Fields drawn after Bilal & Giret (1999). **B**: TiO_2 vs. MgO diagram of Bilal & Giret (1999). **C**: Ba-Rb-Sr ternary diagram of El Bouseily & El Sokkary (1975) showing a moderately differentiated character for all the analyzed samples. Color key as in figure 9.

sample 021-02 which is classified within the anorthosite/rapakivi group of anorogenic suites. The latter classification is probably related to the slightly higher amount of K_2O displayed by this sample. The granite-gneiss displays enrichment in REE (La and Lu normalized values of 245-455 and 35-53, respectively) with a moderately fractionated pattern ($[La/Lu]_N$ between 7 and 9) and a conspicuous negative europium anomaly (Eu/Eu* of 0.27-0.5). The fractionation is more pronounced for the LREE, while HREE define a nearly flat pattern (figure 12A). Incompatible trace element patterns normalized to the ocean ridge granite of Pearce *et al*. (1984) reveal an enriched nature for the granite-gneiss (particularly in LILE) with slightly negative anomalies of Nb, Ta, Zr and

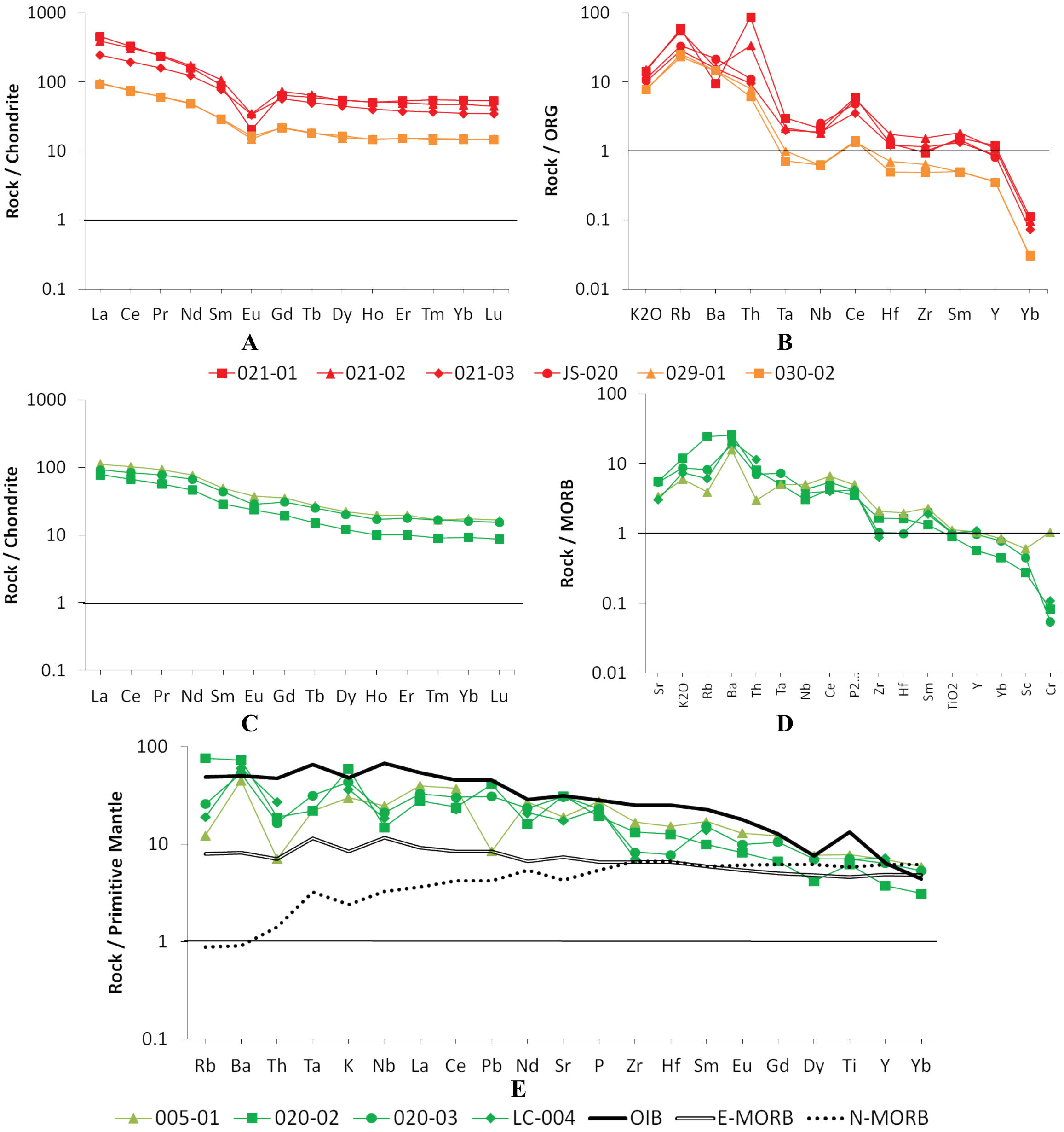

Figure 12 – REE and trace element patterns for both granitic and mafic rocks. **A**: REE patterns of granite-gneiss and granodiorite. Chondrite normalization values are from Evensen *et al.* (1978). **B**: Trace element patterns of granite-gneiss and granodiorite. Normalization to the Ocean Ridge Granite of Pearce *et al.* (1984). **C**: REE patterns of metamafic rocks. Chondrite normalization values are from Evensen *et al.* (1978). **D**: Trace element patterns of metamafic rocks normalized to MORB of Pearce (1982). **E**: Trace element patterns of metamafic rocks. Normalization values and mean ocean-island basalt (OIB), enriched mid-ocean ridge basalt (E-MORB) and normal mid-ocean ridge basalt (N-MORB) patterns are from Sun & McDonough (1989). Color key as in figure 9.

Hf (figure 12B). These patterns are similar to those of within-plate granites of attenuated continental lithosphere from Skaergaard and Mull (Pearce *et al.*, 1984).

The granodiorite has SiO_2 and Na_2O+K_2O contents close to 62 and 6 wt.%, respectively, which along with a CaO amount of *ca.* 5 wt.% reflect a calc-alkalic nature for these rocks (figure 10B). Using the cationic classification of Debon & Le Fort

(1982) leads to a confirmation of the petrographically assessed granodioritic nature of this group (figure 9B). A/CNK values of ~0.89 allow classifying these rocks as metaluminous (figure 10A), while a positive feldspathoid-silica saturation index indicates a silica-saturated character (Frost & Frost, 2008). Relatively low values of Fe* (close to ~0.65) implies that the granodiorite falls within the field of magnesian granitoids (figure 10C) corresponding mainly to the domain of cordilleran granites (Frost *et al.*, 2001). The moderate contents in REE and incompatible trace elements of the granodiorite are manifested in the Nb vs. Y (Pearce *et al.*, 1984) and FeO^t/MgO vs. Zr+Nb+Ce+Y (Whalen *et al.*, 1987) diagrams, which allow designating a convergent margin environment of formation of these rocks, as well as either a M-, S- or I-type nature (figure 10). The MgO/TiO_2 values of 3.80 and 4.05 (figure 11B) indicate a high-K calc-alkaline character and association to an orogenic setting and a mixed, crust/mantle source (Bilal & Giret, 1999). Ba, Rb and Sr contents of these rocks are consistent with a granodioritic nature displaying moderate degrees of differentiation (figure 11C) and Agrawal's (1995) discriminating functions allocate this unit to a late-orogenic setting ($-5.78 < D_1 < -5.13$, $6.94 < R_1 < 7.77$, $-2.75 < D_2 < -2.38$, $2.02 < R_2 < 2.37$). Granodiorite REE patterns indicate both moderate enrichment and fractionation with normalized La and Lu contents of 94-97 and ~15, respectively, and a $(La/Lu)_N$ ratio of ~6.5 (figure 12A). In addition, a flat HREE pattern and a subdued negative Eu anomaly are observed, the latter being characterized by Eu/Eu* values of ~0.6. Incompatible trace element patterns are characterized by Nb and Ta negative anomalies and LILE enrichments. The lines shown in figure 12B display an affinity to those of volcanic arc granites from Jamaica and Chile published by Pearce *et al.* (1984). Given the metaluminous character, the moderately fractioned REE and flat HREE patterns and the incompatible element characteristics, the granodiorite more likely represents an I-type granitoid generated within a volcanic arc environment.

The metamafic rocks yielded fairly uniform geochemical results, with SiO_2 varying between 49 and 56 wt.% and Na_2O+K_2O between 4.5 and 6.6 wt.%. When the R1-R2 cationic classification scheme of De La Roche *et al.* (1980) is implemented, the samples display a tendency to cluster within the monzogabbro field, half way between the alkalic and subalkalic domains (figure 9A). This moderate enrichment in alkalis is manifested in the presence of some quantities of potassic feldspar and an andesine composition of the plagioclase. Because of these enrichments in Na_2O, K_2O and Al_2O_3

(the latter being the case of the leucocratic plagioclase-rich samples), series classification diagrams (*e.g.*, Kuno, 1966; Irving & Baragar, 1971; Jensen, 1976; Peccerillo & Taylor, 1976) turn out to be misleading, and were therefore not considered. It is worthwhile to notice that the analyzed samples have relatively high P_2O_5 values (close to 0.5-0.6 wt.%), which is manifested in abundant apatite as accessory mineral. Enriched REE patterns for these rocks (normalized La and Lu values of 78-111 and 9-17, respectively) are characterized by moderate degrees of fractionation ($[La/Lu]_N$ between 6 and 9), subtle to almost null Eu anomalies (Eu/Eu* between 0.77 and 1) and a rather flat HREE distribution (figure 12C). The incompatible trace element patterns normalized to primitive mantle (figure 12E) indicate a general affinity with an OIB composition, with some elements above and below the mean value. In general, negative anomalies of Rb, Th, Ta, Nb, Zr and Hf are outstanding. For the amphibolite (sample 005-01), radiogenic elements such as Th and Pb display markedly low normalized values similar to those of E-MORB. Normalization to MORB of Pearce (1982) indicates no substantial anomalies of Nb and Ta, and slight to moderate ones of Zr and Hf. All samples are depleted in Cr, except for sample 005-01 which displays contents similar to that of MORB (figure 12D). This pattern resembles that of transitional to alkalic within-plate basalts from Gregory Rift and Azores (Pearce, 1982) and dolerites and gabbros associated to A-type granites from Corsica (Bonin, 2007).

4.4.2. U-Pb geochronology

Results of LA-ICPMS U-Pb analysis of zircon from two granodiorites, three granite-gneisses and two metamonzogabbros are summarized in table 2. Both core and rim of grains were analyzed where possible with the aid of CL images (see appendix I).

4.4.2.1. Granodiorite

Zircons from this unit are relatively small (70-100 μm) and commonly display euhedral to subhedral habits with well-developed prismatic and bi-pyramidal forms. They are generally colorless with small black-colored opaque inclusions being common. CL imaging reveals that, although not conspicuous, grains display oscillatory zoning (OZ) and are quite rich in inclusions which sometimes display elongated shapes parallel to crystal faces defined by the OZ. Lighter, irregularly bordered patches within which OZ can be observed are a common feature occurring mainly at the apexes (pyramidal areas) of these zircons (figure 13). This texture is similar to that related to complex

Table 2 – LA-ICPMS U-Pb zircon data of the studied samples. “C” and “R” in the spot names stand for “core” and “rim”, respectively. Common lead (Pb$_c$) corrections were applied in the calculation of isotope ratios and ages by using measured ^{204}Pb. Reported errors are 2σ.

Spot	**U ppm**	**Th ppm**	**Th/ U**	**^{206}Pb$_c$ (%)**	**^{206}Pb/ ^{204}Pb**	**^{207}Pb/ ^{235}U**	**error (%)**	**^{206}Pb/ ^{238}U**	**error (%)**	**^{207}Pb/ ^{206}Pb**	**error (%)**	**err. corr. (ρ)**	**^{207}Pb/ ^{235}U age (Ma)**	**error (Ma)**	**^{206}Pb/ ^{238}U age (Ma)**	**error (Ma)**	**^{207}Pb/ ^{206}Pb age (Ma)**	**error (Ma)**	**conc. (%)**
Sample 028-01 (granodiorite)																			
Z14	60	27	0.45	0.67	2734.5	0.2681	6.5	0.0287	2.0	0.0678	6.1	0.3152	241.2	13.8	182.2	3.7	862.9	122.0	21
Z16	43	14	0.33	2.60	709.4	0.2105	6.1	0.0263	2.2	0.0581	5.6	0.3622	194.0	10.7	167.2	3.7	533.3	118.8	31
Z19	168	71	0.42	0.22	9345.0	0.1731	2.5	0.0257	1.6	0.0488	2.0	0.6321	162.1	3.8	163.9	2.6	136.5	45.7	120
Z21	53	21	0.40	0.91	2023.9	0.1844	5.2	0.0267	2.2	0.0501	4.7	0.4244	171.9	8.2	169.8	3.7	200.5	105.9	85
Z26	24	8	0.34	1.95	1519.3	0.3136	13.2	0.0275	2.3	0.0826	13.0	0.1722	277.0	31.4	175.2	4.0	1259.1	234.2	14
Z27	171	52	0.31	0.16	11643.2	0.2123	3.4	0.0272	2.2	0.0567	2.6	0.6394	195.5	6.0	172.7	3.7	480.0	56.5	36
Z28	29	11	0.40	0.98	1885.4	0.1773	6.4	0.0268	1.7	0.0480	6.1	0.2618	165.7	9.7	170.2	2.8	101.3	138.9	168
Z30	160	70	0.44	1.57	939.0	0.1814	4.2	0.0285	1.3	0.0463	4.0	0.3216	169.3	6.5	180.8	2.4	10.8	92.5	1671
Z31	53	19	0.36	8.77	208.8	0.7163	3.2	0.0359	2.0	0.1447	2.4	0.6394	548.5	13.7	227.4	4.9	2283.9	40.7	10
Z32	793	108	0.14	0.13	13652.8	0.2084	2.1	0.0297	1.8	0.0509	1.1	0.8678	192.2	3.7	188.7	3.4	236.2	24.1	80
Z33	63	31	0.50	0.46	4032.4	0.1866	3.9	0.0273	1.8	0.0496	3.5	0.4593	173.7	6.2	173.4	3.1	177.4	79.1	98
Z35	135	91	0.67	0.26	6992.4	0.1967	3.5	0.0299	1.5	0.0477	3.1	0.4433	182.3	5.8	189.9	2.9	85.4	71.9	222
Z36	50	26	0.52	0.72	2549.3	0.2512	9.1	0.0290	2.0	0.0629	8.8	0.2258	227.5	18.3	184.1	3.7	703.7	177.7	26
Z39	87	32	0.37	0.29	11591.9	0.2254	3.9	0.0299	2.4	0.0547	3.0	0.6325	206.4	7.2	189.8	4.6	400.4	65.5	47
Z41	58	27	0.47	0.98	1887.8	0.6181	3.3	0.0289	1.8	0.1550	2.7	0.5640	488.7	12.6	183.8	3.4	2402.1	45.1	8
Z43	108	52	0.48	0.87	4296.6	0.1944	4.0	0.0233	3.0	0.0605	2.6	0.7573	180.4	6.6	148.6	4.4	620.0	54.9	24
Z47	68	28	0.42	0.50	3692.5	0.2057	3.4	0.0282	1.7	0.0528	2.9	0.5066	190.0	5.8	179.5	3.0	321.6	64.6	56
Z50	107	22	0.20	0.51	3627.7	0.2841	6.6	0.0368	4.0	0.0560	5.2	0.6123	253.9	14.7	233.1	9.3	451.5	111.4	52
Z52	275	164	0.60	0.19	14832.2	0.2102	2.7	0.0288	1.8	0.0529	2.0	0.6578	193.7	4.7	183.0	3.2	326.5	45.0	56
Z53	231	130	0.56	0.18	10385.1	0.2016	3.0	0.0291	2.1	0.0502	2.1	0.7102	186.5	5.1	185.1	3.9	204.1	48.5	91
Sample 030-01 (granodiorite)																			
Z5	10	3	0.29	8.30	216.7	2.9825	2.7	0.0678	1.6	0.3192	2.0	0.6292	1403.2	20.1	422.7	7.2	3566.0	30.4	12
Z6	194	101	0.52	0.48	9242.6	0.2036	6.4	0.0292	2.8	0.0505	5.7	0.4340	188.2	10.9	185.7	5.1	218.6	127.9	85
Z7	310	81	0.26	6.52	281.4	0.2756	7.2	0.0347	4.7	0.0576	5.2	0.6715	247.2	15.6	219.9	10.8	515.0	109.4	43
Z9	136	62	0.45	0.14	12783.5	0.2403	2.2	0.0281	1.6	0.0619	1.5	0.7392	218.7	4.3	178.9	2.9	671.8	31.2	27
Z10	40	15	0.37	0.80	2298.6	0.1944	6.4	0.0269	1.8	0.0524	6.1	0.2889	180.4	10.5	171.1	3.1	304.0	133.1	56
Z11	78	41	0.53	0.29	10211.4	0.2144	3.8	0.0287	2.4	0.0543	2.9	0.6333	197.2	6.8	182.1	4.3	382.1	64.9	48
Z12C	145	91	0.63	0.37	5032.8	0.2049	5.0	0.0304	1.7	0.0489	4.6	0.3493	189.3	8.5	193.2	3.3	140.7	105.6	137
Z12R	129	16	0.13	1.60	1146.2	0.2426	5.0	0.0313	2.5	0.0562	4.4	0.4899	220.6	9.9	198.6	4.9	461.8	93.8	43
Z13	111	51	0.46	0.15	12291.4	0.2044	3.2	0.0287	1.7	0.0516	2.7	0.5295	188.8	5.5	182.5	3.1	268.7	61.3	68
Z15	859	126	0.15	0.26	7023.9	0.2119	5.2	0.0323	3.7	0.0476	3.6	0.7132	195.1	9.1	204.7	7.4	80.6	83.5	254
Z16R	98	32	0.33	0.36	6743.9	0.2094	4.5	0.0305	2.2	0.0498	3.9	0.4958	193.1	7.9	193.6	4.3	186.8	88.6	104
Z17	88	51	0.58	0.45	4091.8	0.1950	3.7	0.0283	2.0	0.0499	3.1	0.5543	180.9	6.1	180.1	3.6	190.6	69.6	95
Z18	65	32	0.50	0.31	5988.0	0.1969	4.5	0.0275	2.5	0.0519	3.7	0.5684	182.5	7.5	174.9	4.4	282.6	82.1	62
Z19	57	20	0.35	0.40	4576.7	0.2147	3.8	0.0276	2.1	0.0564	3.1	0.5640	197.5	6.8	175.6	3.7	467.7	68.1	38
Z21C	137	76	0.55	0.34	5413.7	0.2176	3.8	0.0299	1.3	0.0528	3.5	0.3551	199.9	6.8	189.8	2.5	320.8	78.4	59
Z21R	167	70	0.42	0.21	8771.2	0.2175	4.0	0.0296	3.0	0.0533	2.6	0.7570	199.8	7.2	188.1	5.6	340.1	57.5	55
Z22	99	38	0.38	0.27	6806.6	0.2063	2.6	0.0275	1.4	0.0545	2.2	0.5269	190.4	4.5	174.7	2.4	389.9	48.6	45

Table 2 – (continued).

Spot	U ppm	Th ppm	Th/ U	$^{206}Pb_c$ (%)	$^{206}Pb/^{204}Pb$	$^{207}Pb/^{235}U$	error (%)	$^{206}Pb/^{238}U$	error (%)	$^{207}Pb/^{206}Pb$	error (%)	err. corr. (ρ)	$^{207}Pb/^{235}U$ age (Ma)	error (Ma)	$^{206}Pb/^{238}U$ age (Ma)	error (Ma)	$^{207}Pb/^{206}Pb$ age (Ma)	error (Ma)	conc. (%)
Z25	94	48	0.51	0.34	5419.7	0.1990	3.8	0.0277	2.2	0.0521	3.1	0.5827	184.3	6.3	176.0	3.8	291.8	68.3	60
Z26	82	34	0.42	0.40	4622.1	0.2651	4.1	0.0286	1.8	0.0671	3.7	0.4440	238.8	8.8	182.1	3.3	841.5	75.3	22
Z27	113	46	0.40	0.60	5478.8	0.2000	3.9	0.0287	1.8	0.0505	3.5	0.4528	185.1	6.6	182.6	3.2	216.7	79.2	84
Z28	117	58	0.50	1.04	1766.5	0.2163	6.4	0.0277	2.3	0.0567	6.0	0.3597	198.8	11.5	175.9	4.0	480.4	126.4	37
Z29	290	27	0.09	0.10	17590.9	0.2068	2.3	0.0304	1.6	0.0493	1.7	0.6842	190.9	4.0	193.3	3.0	160.6	38.8	120
Z30	143	77	0.54	0.43	4328.8	0.2042	3.4	0.0292	1.0	0.0507	3.2	0.3063	188.7	5.8	185.6	1.9	227.4	72.7	82
Z31	81	39	0.49	0.40	5629.9	0.1844	3.4	0.0265	1.9	0.0505	2.8	0.5618	171.9	5.4	168.5	3.2	218.2	64.5	77
Z32	76	37	0.49	12.22	149.6	0.3437	2.5	0.0378	1.7	0.0659	1.5	0.7517	299.9	6.4	239.2	4.6	804.0	31.2	30
Z33	129	70	0.54	0.39	4712.6	0.1993	2.1	0.0282	1.0	0.0513	1.9	0.4462	184.6	3.6	179.3	1.7	252.4	43.6	71
Sample 017-05 (granite-gneiss)																			
Z2C	173	27	0.16	0.02	72954.2	2.7958	3.9	0.2244	3.7	0.0903	1.0	0.9669	1354.4	28.5	1305.3	44.1	1432.8	18.7	91
Z2C	2302	100	0.04	1.88	172.8	0.4965	2.6	0.0518	2.2	0.0696	1.3	0.8661	409.3	8.7	325.4	7.1	915.1	25.9	36
Z3C	1560	243	0.16	0.62	2887.6	1.0722	3.0	0.0890	2.9	0.0873	0.9	0.9545	739.8	15.7	549.9	15.1	1367.8	17.1	40
Z4C	746	41	0.05	0.43	4089.5	1.4982	2.7	0.1282	2.5	0.0848	0.9	0.9441	929.6	16.3	777.6	18.7	1310.0	17.1	59
Z4C	61	5	0.08	0.21	7431.4	5.4249	3.7	0.3356	2.7	0.1173	2.5	0.7357	1888.8	30.9	1865.2	43.6	1914.8	43.8	97
Z5C	498	70	0.14	0.01	170239.6	3.3873	3.3	0.2603	3.2	0.0944	0.9	0.9614	1501.5	25.9	1491.4	42.6	1515.7	17.3	98
Z5R	225	21	0.09	0.03	50468.0	1.8460	2.6	0.1767	2.4	0.0758	1.0	0.9251	1062.0	17.1	1049.1	23.5	1088.5	19.8	96
Z6C	2111	251	0.12	0.28	5952.2	2.7124	3.4	0.2245	2.4	0.0876	2.4	0.7135	1331.9	25.2	1305.7	28.9	1374.2	45.5	95
Z7C	1184	135	0.11	0.19	9180.1	1.7769	5.2	0.1302	4.7	0.0990	2.2	0.9041	1037.0	33.2	788.8	34.7	1605.4	40.7	49
Z7C	2003	231	0.12	0.19	9222.3	1.0695	5.5	0.0919	5.3	0.0844	1.6	0.9569	738.5	28.6	567.0	28.6	1301.2	30.8	44
Z9C	127	12	0.09	0.17	9989.6	2.6623	3.9	0.2123	3.2	0.0909	2.2	0.8243	1318.1	28.4	1241.3	36.3	1445.1	41.5	86
Z10C	73	14	0.20	0.24	6668.0	3.1039	5.4	0.2427	4.6	0.0928	2.8	0.8547	1433.6	40.8	1400.7	58.1	1482.9	52.3	94
Z12C	1424	45	0.03	0.59	3090.0	0.6358	3.4	0.0573	2.2	0.0805	2.5	0.6657	499.7	13.2	359.1	7.8	1209.3	48.5	30
Z13C	725	91	0.13	0.03	177490.6	1.4916	2.6	0.1275	2.1	0.0849	1.5	0.8084	927.0	15.5	773.4	15.1	1312.8	29.0	59
Z13C	942	17	0.02	0.10	16975.7	1.6062	2.4	0.1495	2.0	0.0779	1.4	0.8236	972.6	15.0	898.1	16.6	1145.1	26.9	78
Z14C	405	60	0.15	0.12	13958.9	2.3441	4.9	0.2016	4.6	0.0843	1.9	0.9238	1225.8	34.5	1183.8	49.1	1300.4	36.2	91
Z14C	529	11	0.02	0.03	46588.2	3.2678	2.9	0.2538	2.6	0.0934	1.4	0.8797	1473.4	22.6	1458.2	33.6	1495.4	26.2	98
Z15C	828	37	0.04	0.03	59903.5	3.3042	2.8	0.2621	2.4	0.0914	1.5	0.8525	1482.0	21.5	1500.8	31.7	1455.3	27.4	103
Z16C	1555	236	0.15	1.27	1331.5	2.4226	2.9	0.1850	2.4	0.0950	1.6	0.8332	1249.3	20.6	1094.5	24.3	1527.1	29.6	72
Z17C	311	5	0.02	0.07	15954.8	1.9197	2.6	0.1833	1.8	0.0760	1.9	0.6726	1088.0	17.3	1085.0	17.6	1094.0	38.3	99
Z18C	1389	228	0.16	0.17	10538.2	1.0024	3.8	0.0932	3.4	0.0780	1.6	0.9074	705.0	18.9	574.2	18.7	1147.8	31.0	50
Z18C	528	13	0.03	0.04	43489.9	3.3020	3.3	0.2598	2.9	0.0922	1.5	0.8895	1481.5	25.4	1489.0	38.9	1470.9	28.3	101
Z19C	342	26	0.08	0.01	111708.3	3.2858	2.8	0.2537	2.2	0.0939	1.7	0.7930	1477.7	21.5	1457.5	28.8	1506.8	31.8	97
Z20C	3416	590	0.17	0.27	6498.9	1.8082	2.5	0.1465	2.0	0.0895	1.5	0.7932	1048.4	16.0	881.2	16.1	1415.6	28.4	62
Z21C	1787	154	0.09	3.31	83.0	0.8618	3.6	0.0844	3.2	0.0740	1.4	0.9088	631.1	16.7	522.5	16.4	1042.2	29.0	50
Z22C	970	140	0.14	0.13	13680.5	0.7492	3.7	0.0724	3.4	0.0750	1.5	0.9127	567.8	15.9	450.7	14.6	1069.4	29.9	42
Z22C	123	3	0.03	0.17	9973.2	2.2892	3.4	0.1957	2.7	0.0848	2.0	0.8066	1209.0	23.7	1152.4	28.9	1311.4	38.4	88
Z24C	632	88	0.14	0.02	72632.0	3.2814	2.9	0.2606	2.4	0.0913	1.5	0.8441	1476.6	22.1	1492.7	32.2	1453.6	29.0	103
Z24C	834	39	0.05	0.03	57891.0	2.0741	3.2	0.1982	2.9	0.0759	1.5	0.8879	1140.3	22.0	1165.6	30.6	1092.3	29.6	107

Table 2 – (continued).

Spot	U ppm	Th ppm	Th/ U	^{206}Pb$_c$ (%)	^{206}Pb/ ^{204}Pb	^{207}Pb/ ^{235}U	error (%)	^{206}Pb/ ^{238}U	error (%)	^{207}Pb/ ^{206}Pb	error (%)	err. corr. (ρ)	^{207}Pb/ ^{235}U age (Ma)	error (Ma)	^{206}Pb/ ^{238}U age (Ma)	error (Ma)	^{207}Pb/ ^{206}Pb age (Ma)	error (Ma)	conc. (%)
Z25C	522	69	0.13	0.24	7215.7	1.3723	4.1	0.1145	3.5	0.0870	2.0	0.8684	877.2	23.7	698.5	23.4	1359.7	38.4	51
Z25R	86	11	0.12	0.29	5873.3	2.0835	4.3	0.1954	2.9	0.0773	3.1	0.6850	1143.4	28.8	1150.6	30.7	1129.8	60.4	102
Z26R	552	72	0.13	0.04	82325.5	1.6723	2.5	0.1677	1.9	0.0723	1.7	0.7431	998.1	16.0	999.3	17.4	995.2	34.1	100
Z27C	412	66	0.16	0.03	55360.2	3.5384	2.4	0.2738	1.9	0.0937	1.6	0.7698	1535.9	19.1	1560.2	25.9	1502.5	29.1	104
Z28C	1853	258	0.14	1.33	1323.6	1.3242	3.6	0.1175	3.2	0.0818	1.6	0.8968	856.4	20.8	716.0	22.1	1239.7	30.8	58
Z29C	662	42	0.06	0.03	49366.1	2.3993	2.5	0.2072	2.1	0.0840	1.3	0.8464	1242.4	17.8	1214.0	23.5	1291.9	25.8	94
Z29R	148	34	0.23	0.14	12521.3	1.6679	3.9	0.1661	3.4	0.0728	1.8	0.8862	996.4	24.2	990.7	31.3	1008.9	35.7	98
Sample 022-01 (granite-gneiss)																			
Z01C	291	45	0.16	0.01	203325.6	3.0022	1.1	0.2191	1.0	0.0994	0.5	0.9021	1408.2	8.4	1277.1	11.6	1612.5	8.9	79
Z02C	428	108	0.25	0.02	184838.2	2.3663	1.3	0.2041	1.0	0.0841	0.7	0.8264	1232.5	9.0	1197.1	11.4	1295.0	13.8	92
Z03C	250	31	0.12	1.89	838.3	4.0345	1.2	0.2872	1.0	0.1019	0.6	0.8426	1641.2	9.4	1627.4	14.2	1658.9	11.4	98
Z07C	551	159	0.29	0.01	212350.7	3.2488	2.3	0.2467	2.0	0.0955	1.2	0.8645	1468.9	17.9	1421.4	25.6	1538.2	21.9	92
Z09C	190	46	0.24	0.02	74517.8	3.3427	2.1	0.2589	2.0	0.0936	0.6	0.9638	1491.1	16.4	1484.3	26.9	1500.7	10.6	99
Z10C	337	70	0.21	0.07	72757.4	2.9592	2.2	0.2389	2.0	0.0898	1.0	0.8832	1397.2	16.7	1380.9	24.4	1422.3	19.8	97
Z12C	489	100	0.20	0.02	109185.2	2.4507	2.7	0.2072	2.6	0.0858	0.8	0.9582	1257.6	19.6	1213.9	29.0	1333.3	15.1	91
Z18R	762	81	0.11	0.01	173808.1	1.7724	3.1	0.1487	2.9	0.0864	1.2	0.9187	1035.4	20.1	893.8	24.0	1347.9	23.7	66
Z24C	544	152	0.28	0.01	212806.0	3.4153	2.3	0.2536	2.2	0.0977	0.7	0.9552	1507.9	18.2	1457.2	29.1	1580.0	12.9	92
Z26C	630	179	0.28	0.01	205242.4	3.2970	2.3	0.2494	2.1	0.0959	1.0	0.9000	1480.3	18.1	1435.6	27.1	1545.1	19.1	93
Z28C	339	52	0.15	0.01	172799.2	3.0441	1.6	0.2340	1.5	0.0943	0.7	0.9027	1418.8	12.3	1355.5	17.8	1515.0	13.1	89
Z29C	181	40	0.22	0.06	41971.8	2.9033	1.7	0.2326	1.5	0.0905	0.8	0.8785	1382.8	13.0	1348.3	18.5	1436.3	15.7	94
Z29R	67	6	0.09	0.09	18459.9	1.7582	2.3	0.1652	1.9	0.0772	1.2	0.8444	1030.2	14.6	985.8	17.5	1125.8	24.0	88
Z30C	329	55	0.17	0.02	102979.4	2.7233	1.6	0.2218	1.5	0.0891	0.7	0.8954	1334.8	12.1	1291.2	17.1	1405.6	13.9	92
Z32C	539	66	0.12	0.03	89619.6	2.4352	2.2	0.2143	2.0	0.0824	0.9	0.9136	1253.0	15.6	1251.5	22.7	1255.6	17.3	100
Z33C	196	29	0.15	0.02	91588.1	2.9761	1.6	0.2366	1.5	0.0912	0.6	0.9373	1401.5	12.1	1369.2	18.5	1451.1	10.6	94
Z33C	253	34	0.13	0.01	135473.3	3.4445	1.8	0.2629	1.7	0.0950	0.7	0.9163	1514.6	14.2	1504.9	22.3	1528.2	13.7	98
Z34C	287	62	0.21	0.02	96022.8	3.3827	2.1	0.2637	1.9	0.0930	1.0	0.8882	1500.4	16.4	1508.7	25.1	1488.7	18.2	101
Z35C	232	42	0.18	0.02	93881.9	3.3158	1.7	0.2537	1.4	0.0948	1.0	0.8219	1484.8	13.4	1457.7	18.5	1523.7	18.4	96
Z36C	172	23	0.14	0.03	55591.6	3.0306	1.6	0.2388	1.2	0.0921	1.0	0.7909	1415.4	12.0	1380.2	15.5	1468.6	18.2	94
Z37C	191	50	0.26	0.03	53720.6	1.9008	1.8	0.1727	1.4	0.0798	1.0	0.8098	1081.4	11.6	1027.2	13.5	1192.1	20.2	86
Z39C	130	20	0.15	0.03	55702.8	2.5147	1.8	0.2054	1.4	0.0888	1.1	0.7812	1276.3	12.7	1204.4	15.1	1399.5	20.9	86
Z39R	89	11	0.12	0.07	22698.3	1.6832	2.7	0.1593	2.2	0.0766	1.5	0.8319	1002.2	16.8	953.1	19.5	1111.2	29.1	86
Z41C	335	88	0.26	0.02	92089.4	3.1112	2.2	0.2487	2.1	0.0907	0.9	0.9239	1435.5	17.1	1431.9	26.6	1440.7	16.3	99
Z42C	232	41	0.18	0.02	87322.5	2.4401	2.0	0.2085	1.7	0.0849	1.1	0.8482	1254.5	14.5	1221.0	19.1	1312.4	20.7	93
Z43C	217	63	0.29	0.03	59266.2	2.7665	2.3	0.2273	2.0	0.0883	1.0	0.9001	1346.5	16.7	1320.1	24.3	1388.7	18.8	95
Z45C	66	11	0.17	0.26	6400.7	3.4738	3.0	0.2382	1.9	0.1058	2.3	0.6412	1521.3	23.7	1377.4	24.1	1727.6	42.1	80
Sample PGG-18 (granite-gneiss)																			
Z1C	728	175	0.24	0.02	88997.3	1.1333	2.3	0.0979	2.0	0.0840	1.1	0.8868	769.3	12.3	602.0	11.7	1291.9	20.5	47
Z1C	520	18	0.03	0.01	183455.9	3.4019	1.9	0.2638	1.7	0.0935	0.9	0.8794	1504.8	15.0	1509.2	22.8	1498.7	17.2	101
Z2C	349	13	0.04	0.02	73853.7	3.4210	2.4	0.2654	2.2	0.0935	1.0	0.9150	1509.2	18.5	1517.3	29.4	1497.9	18.0	101

Table 2 – (continued).

Spot	U ppm	Th ppm	Th/ U	$^{206}Pb_c$ (%)	$^{206}Pb/^{204}Pb$	$^{207}Pb/^{235}U$	error (%)	$^{206}Pb/^{238}U$	error (%)	$^{207}Pb/^{206}Pb$	error (%)	err. corr. (ρ)	$^{207}Pb/^{235}U$ age (Ma)	error (Ma)	$^{206}Pb/^{238}U$ age (Ma)	error (Ma)	$^{207}Pb/^{206}Pb$ age (Ma)	error (Ma)	conc. (%)
Z3C	113	11	0.09	0.07	22114.0	3.0606	2.4	0.2489	2.0	0.0892	1.2	0.8612	1422.9	17.9	1432.6	26.0	1408.4	22.7	102
Z4C	239	20	0.09	0.03	59681.6	3.3521	2.6	0.2603	2.4	0.0934	1.0	0.9250	1493.3	20.0	1491.2	31.7	1496.3	18.4	100
Z4R	312	114	0.37	0.02	70753.3	1.5343	3.5	0.1560	2.6	0.0713	2.3	0.7421	944.2	21.1	934.8	22.4	966.4	46.7	97
Z5C	304	48	0.16	0.03	57814.4	2.9678	2.7	0.2346	2.5	0.0918	1.0	0.9252	1399.4	20.5	1358.4	30.8	1462.5	19.5	93
Z5R	247	22	0.09	0.03	50282.2	1.7549	4.5	0.1632	4.3	0.0780	1.4	0.9479	1029.0	28.7	974.6	38.4	1146.4	28.2	85
Z6C	516	80	0.16	0.01	116395.6	3.0288	2.8	0.2443	2.4	0.0899	1.5	0.8468	1414.9	21.0	1408.9	29.7	1423.9	28.0	99
Z6C	1331	84	0.06	0.02	73132.4	1.6391	3.3	0.1379	2.5	0.0862	2.2	0.7480	985.3	20.7	832.8	19.3	1342.7	41.9	62
Z8C	818	37	0.04	0.01	252711.1	2.8240	3.1	0.2320	2.9	0.0883	1.1	0.9371	1361.9	23.1	1345.2	35.3	1388.2	20.7	97
Z9C	56	12	0.22	0.16	9967.2	3.0439	3.2	0.2340	2.8	0.0943	1.7	0.8557	1418.7	24.3	1355.4	33.6	1515.0	31.1	89
Z10C	96	13	0.13	0.08	21094.8	2.9466	2.5	0.2310	2.1	0.0925	1.4	0.8285	1394.0	18.9	1339.7	25.2	1478.0	26.5	91
Z11C	183	26	0.14	0.04	37379.4	2.4020	3.0	0.2049	2.8	0.0850	1.2	0.9214	1243.2	21.5	1201.4	30.6	1316.3	22.7	91
Z12C	288	42	0.15	0.03	59247.9	2.6358	3.2	0.2155	2.9	0.0887	1.2	0.9255	1310.7	23.1	1258.0	33.5	1398.0	22.9	90
Z12C	144	10	0.07	0.05	30473.5	3.0959	2.7	0.2371	2.4	0.0947	1.4	0.8576	1431.7	20.8	1371.5	29.0	1522.3	26.3	90
Z13C	144	26	0.18	0.05	35936.0	3.1094	3.1	0.2435	2.7	0.0926	1.6	0.8670	1435.0	23.8	1404.6	34.2	1480.4	29.3	95
Z13R	42	27	0.66	0.32	5548.0	1.7263	4.3	0.1714	3.6	0.0730	2.3	0.8456	1018.4	27.0	1020.0	33.9	1014.8	45.2	101
Z14C	762	70	0.09	0.02	79546.8	2.8587	3.7	0.2345	3.5	0.0884	1.2	0.9504	1371.1	27.5	1358.0	43.0	1391.6	22.0	98
Z15C	288	37	0.13	0.02	94658.9	2.9959	2.6	0.2406	2.4	0.0903	1.0	0.9198	1406.6	19.4	1389.6	29.4	1432.4	19.1	97
Z16C	924	181	0.20	0.01	180230.7	2.8927	3.1	0.2346	2.9	0.0894	1.0	0.9499	1380.0	23.0	1358.3	35.8	1413.7	18.3	96
Z16C	976	16	0.02	0.01	193583.7	3.4568	2.8	0.2633	2.7	0.0952	0.8	0.9618	1517.4	22.0	1506.8	36.4	1532.3	14.5	98
Z17C	482	8	0.02	0.02	93798.6	2.8212	2.7	0.2148	2.5	0.0952	0.8	0.9506	1361.2	19.7	1254.5	28.7	1532.9	15.4	82
Z17R	48	12	0.25	0.15	11595.5	2.4749	3.7	0.2045	3.1	0.0878	2.1	0.8247	1264.7	26.6	1199.2	33.5	1377.9	39.9	87
Z18C	165	19	0.12	0.05	31725.5	2.8938	2.5	0.2230	2.3	0.0941	1.0	0.9227	1380.3	19.0	1297.7	27.5	1510.5	18.4	86
Z18R	21	34	1.64	0.60	2870.2	1.5549	4.9	0.1595	3.9	0.0707	3.0	0.7954	952.4	30.0	954.0	34.7	948.9	59.7	101
Z19C	78	10	0.12	0.11	14882.3	2.8984	3.2	0.2294	2.9	0.0916	1.3	0.9106	1381.5	24.1	1331.5	35.3	1459.7	25.1	91
Z20C	177	2	0.01	0.05	34138.9	2.9876	3.5	0.2309	3.2	0.0938	1.2	0.9368	1404.5	26.0	1339.2	39.0	1504.9	22.7	89
Z21C	164	1	0.01	0.04	31148.0	2.9523	2.9	0.2277	2.6	0.0940	1.3	0.8978	1395.4	21.7	1322.4	31.0	1508.9	23.9	88
Z22C	231	23	0.10	0.04	37704.1	2.5927	4.8	0.2160	4.6	0.0870	1.3	0.9618	1298.6	34.3	1260.9	52.3	1361.4	24.9	93
Z23C	352	113	0.32	0.03	54081.1	1.0517	6.3	0.0949	6.1	0.0804	1.2	0.9819	729.7	32.1	584.6	34.3	1205.8	23.2	48
Z23C	412	8	0.02	0.01	653067.6	2.9713	3.6	0.2295	3.5	0.0939	0.9	0.9688	1400.3	27.3	1332.1	42.4	1505.7	17.0	88
Z24C	740	84	0.11	0.01	171898.8	1.7071	4.8	0.1509	4.6	0.0820	1.3	0.9644	1011.2	30.1	906.2	38.8	1246.3	24.6	73
Z24R	28	81	2.87	0.32	5342.7	1.5064	5.1	0.1528	4.0	0.0715	3.2	0.7832	933.0	30.8	916.7	34.3	971.7	63.6	94
Z25C	94	17	0.18	0.07	23625.7	2.7560	2.8	0.2185	2.4	0.0915	1.4	0.8622	1343.7	20.4	1273.8	27.6	1456.8	26.4	87
Z25R	38	13	0.36	0.18	6707.3	2.2089	4.7	0.1998	4.0	0.0802	2.4	0.8587	1183.9	32.4	1174.3	43.3	1201.3	46.8	98
Z26R	147	22	0.15	0.06	28816.7	2.7127	2.6	0.2233	2.2	0.0881	1.4	0.8479	1331.9	19.0	1299.4	25.8	1384.6	26.1	94
Z27C	96	16	0.17	0.10	16173.6	2.9613	3.7	0.2288	3.4	0.0939	1.4	0.9285	1397.7	27.6	1328.0	40.9	1505.9	25.6	88
Z28C	252	21	0.08	0.03	60592.5	2.0056	4.1	0.1622	3.9	0.0897	1.3	0.9508	1117.4	27.5	968.8	35.0	1419.3	24.1	68
Sample 020-02 (metamonzogabbro)																			
Z1C	411	132	0.32	0.02	65028.6	3.2267	2.4	0.2518	2.0	0.0929	1.3	0.8382	1463.6	18.1	1447.8	25.5	1486.6	24.1	97
Z2C	138	4	0.03	0.10	14979.4	1.6854	2.7	0.1602	2.1	0.0763	1.7	0.7807	1003.0	17.3	957.9	19.0	1102.9	33.8	87

Table 2 – (continued).

Spot	U ppm	Th ppm	Th/ U	^{206}Pb$_c$ (%)	^{206}Pb/ ^{204}Pb	^{207}Pb/ ^{235}U	error (%)	^{206}Pb/ ^{238}U	error (%)	^{207}Pb/ ^{206}Pb	error (%)	err. corr. (ρ)	^{207}Pb/ ^{235}U age (Ma)	error (Ma)	^{206}Pb/ ^{238}U age (Ma)	error (Ma)	^{207}Pb/ ^{206}Pb age (Ma)	error (Ma)	conc. (%)
Z4C	240	10	0.04	0.06	30973.9	2.4818	2.8	0.2175	2.5	0.0827	1.3	0.8827	1266.7	20.2	1268.9	28.7	1263.1	25.7	100
Z5C	547	148	0.27	0.01	139131.8	3.2128	2.5	0.2541	2.1	0.0917	1.3	0.8550	1460.3	19.0	1459.4	27.6	1461.5	24.2	100
Z6C	1001	298	0.30	0.01	156511.4	3.3519	2.3	0.2595	1.9	0.0937	1.2	0.8434	1493.2	17.8	1487.3	25.6	1501.6	23.1	99
Z8C	1347	490	0.36	0.01	270295.8	3.5139	1.7	0.2660	1.3	0.0958	1.0	0.7924	1530.3	13.4	1520.7	18.3	1543.8	19.4	99
Z9C	380	85	0.22	0.02	69799.7	3.4091	1.9	0.2609	1.6	0.0948	1.1	0.8239	1506.5	15.0	1494.3	21.1	1523.7	20.4	98
Z10C	84	11	0.13	0.07	22256.4	3.5237	2.7	0.2690	2.0	0.0950	1.7	0.7598	1532.6	20.9	1535.6	27.7	1528.4	32.4	100
Z11C	639	6	0.01	0.01	137652.0	2.1544	2.3	0.1996	2.0	0.0783	1.1	0.8657	1166.5	15.6	1173.1	21.1	1154.2	22.4	102
Z11R	428	68	0.16	0.03	57901.8	1.8033	3.4	0.1776	3.1	0.0736	1.4	0.9079	1046.7	22.0	1053.8	30.0	1031.8	28.6	102
Z12C	199	28	0.14	0.07	24931.7	1.9054	3.5	0.1707	3.1	0.0809	1.7	0.8737	1083.0	23.2	1016.2	28.8	1219.9	33.3	83
Z12C	334	59	0.18	0.03	53950.1	3.2125	2.5	0.2525	2.1	0.0923	1.2	0.8644	1460.2	18.9	1451.2	27.7	1473.3	23.4	99
Z14C	858	174	0.20	0.01	173829.6	2.4893	2.7	0.2147	2.4	0.0841	1.1	0.9054	1268.9	19.4	1253.8	27.8	1294.6	22.1	97
Z14R	1275	5	0.00	0.01	152570.2	2.3240	2.2	0.2096	1.9	0.0804	1.1	0.8636	1219.6	15.4	1226.5	21.1	1207.5	21.6	102
Z15R	952	253	0.27	0.01	158166.5	2.7045	1.7	0.2275	1.3	0.0862	1.1	0.7723	1329.7	12.5	1321.6	15.7	1342.7	20.7	98
Z16C	878	165	0.19	0.01	146098.3	3.5975	1.9	0.2753	1.6	0.0948	1.0	0.8320	1549.0	14.8	1567.5	21.7	1523.7	19.5	103
Z17C	407	98	0.24	0.02	79552.0	3.0105	1.9	0.2414	1.3	0.0904	1.3	0.7202	1410.3	14.1	1394.0	16.8	1435.0	24.5	97
Z18C	396	88	0.22	0.02	68689.2	3.4589	1.8	0.2685	1.4	0.0934	1.1	0.7843	1517.9	14.3	1533.0	19.6	1496.8	21.3	102
Z19C	1277	431	0.34	0.01	217795.8	3.2575	1.9	0.2562	1.7	0.0922	0.9	0.8721	1471.0	14.9	1470.4	22.2	1471.8	17.9	100
Z20C	460	103	0.22	0.02	86938.0	2.8871	2.3	0.2401	2.0	0.0872	1.2	0.8704	1378.5	17.5	1387.1	25.4	1365.3	22.0	102
Z21C	269	21	0.08	0.02	71052.9	3.3290	2.2	0.2593	1.8	0.0931	1.2	0.8356	1487.9	16.9	1486.3	24.1	1490.1	22.5	100
Z22C	280	47	0.17	0.04	45479.4	3.2347	2.4	0.2559	2.0	0.0917	1.2	0.8600	1465.5	18.2	1468.7	26.7	1460.9	22.8	101
Z23C	257	48	0.19	0.04	46645.6	2.3188	2.0	0.2018	1.5	0.0834	1.2	0.7819	1218.1	13.8	1184.8	16.6	1277.5	23.7	93
Z23R	1970	57	0.03	0.01	260316.1	2.2943	1.5	0.2068	1.0	0.0805	1.0	0.7139	1210.5	10.3	1211.6	11.6	1208.7	20.1	100
Z25C	566	136	0.24	0.02	94125.4	3.1116	2.1	0.2476	1.5	0.0911	1.4	0.7373	1435.6	15.8	1426.2	19.5	1449.6	26.4	98
Z26C	362	56	0.15	0.03	58606.3	2.8441	1.7	0.2368	1.2	0.0871	1.2	0.7196	1367.2	12.4	1370.1	14.8	1362.8	22.1	101
Z27C	1213	352	0.29	0.00	444910.3	2.4863	1.7	0.2033	1.2	0.0887	1.1	0.7416	1268.0	11.9	1193.3	13.4	1397.2	21.2	85
Z27R	596	86	0.14	0.02	108956.5	1.7522	2.3	0.1718	1.8	0.0740	1.3	0.8072	1028.0	14.6	1022.2	17.3	1040.2	26.8	98
Z28C	1012	324	0.32	0.01	162249.0	3.1915	2.0	0.2476	1.6	0.0935	1.2	0.7822	1455.1	15.3	1425.9	20.0	1498.0	23.4	95
Z29C	137	14	0.10	0.06	28769.8	3.4365	2.6	0.2650	1.9	0.0941	1.7	0.7377	1512.8	20.1	1515.2	25.7	1509.3	32.5	100
Sample 020-03 (metamonzogabbro)																			
Z1C	56	6	0.10	0.10	16991.6	2.7507	3.4	0.2205	3.0	0.0905	1.6	0.8833	1342.3	24.9	1284.7	34.7	1435.3	29.9	90
Z2C	395	132	0.33	0.02	83613.5	3.0808	2.9	0.2395	2.7	0.0933	1.0	0.9352	1427.9	22.3	1384.2	34.1	1493.7	19.6	93
Z2R	173	14	0.08	0.08	22129.8	2.0179	2.5	0.1867	2.2	0.0784	1.3	0.8676	1121.5	17.0	1103.4	22.1	1156.9	24.7	95
Z3C	171	43	0.25	0.07	23612.6	1.5457	2.7	0.1571	2.3	0.0713	1.4	0.8430	948.8	16.4	940.8	19.8	967.3	29.2	97
Z4C	377	34	0.09	0.01	126893.2	3.1116	2.3	0.2381	2.1	0.0948	1.0	0.9137	1435.6	17.9	1377.0	26.5	1523.5	17.8	90
Z4R	81	18	0.22	0.17	11836.4	1.7250	3.3	0.1655	2.7	0.0756	1.8	0.8274	1017.9	20.9	987.0	24.9	1084.9	36.6	91
Z5C	296	75	0.25	0.02	72407.6	1.8541	3.1	0.1727	2.9	0.0779	1.1	0.9361	1064.9	20.1	1027.1	27.3	1143.1	21.3	90
Z6C	238	47	0.20	0.03	51295.5	3.2973	3.1	0.2586	2.8	0.0925	1.3	0.9126	1480.4	23.7	1482.8	37.1	1476.9	23.7	100
Z7C	113	19	0.17	0.05	34043.5	3.2731	3.3	0.2564	2.9	0.0926	1.5	0.8841	1474.7	25.2	1471.3	38.1	1479.6	28.8	99
Z7R	295	42	0.14	0.03	61135.2	1.9650	2.8	0.1869	2.4	0.0762	1.4	0.8583	1103.6	18.5	1104.8	24.1	1101.2	28.2	100

Table 2 – (continued).

Spot	U ppm	Th ppm	Th/ U	$^{206}Pb_c$ (%)	$^{206}Pb/^{204}Pb$	$^{207}Pb/^{235}U$	error (%)	$^{206}Pb/^{238}U$	error (%)	$^{207}Pb/^{206}Pb$	error (%)	err. corr. (ρ)	$^{207}Pb/^{235}U$ age (Ma)	error (Ma)	$^{206}Pb/^{238}U$ age (Ma)	error (Ma)	$^{207}Pb/^{206}Pb$ age (Ma)	error (Ma)	conc. (%)
Z8C	390	76	0.19	0.01	87015.4	3.3341	2.6	0.2586	2.5	0.0935	1.0	0.9321	1489.1	20.4	1482.7	32.4	1498.2	17.9	99
Z9C	235	74	0.31	0.03	51180.6	3.1877	2.4	0.2457	2.1	0.0941	1.1	0.8892	1454.2	18.0	1416.3	26.6	1510.0	20.2	94
Z9R	114	8	0.07	0.06	27558.1	2.6167	3.6	0.2244	3.0	0.0846	1.9	0.8541	1305.3	25.8	1304.9	35.8	1306.1	35.5	100
Z10C	88	18	0.21	0.11	15864.9	1.8934	3.0	0.1762	2.4	0.0780	1.9	0.7889	1078.8	20.0	1045.9	23.1	1145.8	36.7	91
Z10R	95	25	0.26	0.04	196719.1	1.5255	2.9	0.1515	2.1	0.0730	1.9	0.7374	940.7	17.5	909.4	18.0	1014.8	38.9	90
Z11C	92	18	0.20	0.05	30683.2	3.2819	2.7	0.2464	2.2	0.0966	1.6	0.8090	1476.8	20.6	1420.1	27.6	1559.2	29.2	91
Z11C	42	5	0.12	0.20	8291.7	2.6998	3.6	0.2153	3.1	0.0909	1.9	0.8506	1328.4	26.5	1257.0	35.2	1445.4	35.8	87
Z12C	100	10	0.10	0.02	258963.5	3.0668	2.6	0.2372	2.3	0.0938	1.3	0.8712	1424.4	19.7	1372.0	27.9	1503.8	23.9	91
Z14C	582	164	0.28	0.01	150074.1	2.8719	2.6	0.2298	2.3	0.0906	1.0	0.9134	1374.6	19.1	1333.5	28.1	1439.0	19.7	93
Z14R	75	7	0.09	0.09	11720.0	2.0120	3.7	0.1846	2.9	0.0790	2.4	0.7720	1119.6	24.9	1092.1	28.7	1173.3	45.9	93
Z15C	812	8	0.01	0.01	184330.9	3.1330	2.9	0.2448	2.8	0.0928	1.0	0.9441	1440.8	22.3	1411.4	34.9	1484.6	18.2	95
Z16C	635	16	0.03	0.01	167570.7	3.3003	2.8	0.2545	2.6	0.0941	1.1	0.9283	1481.1	21.8	1461.6	34.2	1509.2	19.7	97
Z16C	86	9	0.11	0.05	40787.6	3.1183	3.0	0.2467	2.7	0.0917	1.3	0.9035	1437.2	22.6	1421.2	34.2	1460.9	24.1	97
Z17C	460	142	0.31	0.02	108224.2	3.0688	2.3	0.2353	2.0	0.0946	1.0	0.8931	1424.9	17.4	1362.0	25.0	1520.3	19.3	90
Z17R	253	73	0.29	0.04	48345.4	1.5290	2.3	0.1540	1.9	0.0720	1.2	0.8539	942.1	13.9	923.5	16.7	985.9	23.9	94
Z18C	265	35	0.13	0.03	63752.3	2.0023	2.5	0.1869	2.2	0.0777	1.1	0.8894	1116.3	16.9	1104.6	22.6	1139.1	22.6	97
Z18C	56	5	0.09	0.12	12463.8	3.1662	3.0	0.2446	2.5	0.0939	1.7	0.8299	1449.0	22.7	1410.5	31.2	1505.8	31.0	94
Z19C	179	13	0.07	0.05	31236.5	3.3655	2.7	0.2614	2.4	0.0934	1.1	0.9101	1496.4	20.8	1497.0	32.6	1495.5	20.9	100
Z20C	95	10	0.10	0.07	24164.6	2.1959	4.3	0.1960	3.9	0.0812	1.7	0.9172	1179.8	29.5	1154.0	41.4	1227.2	33.1	94
Z20R	109	30	0.27	0.09	19627.2	1.6508	3.6	0.1663	3.1	0.0720	1.7	0.8737	989.8	22.4	991.9	28.8	985.4	35.1	101
Z21C	162	21	0.13	0.03	53641.5	2.9037	2.6	0.2285	2.4	0.0922	1.1	0.9008	1382.9	19.6	1326.7	28.2	1470.6	21.4	90
Z23C	297	34	0.11	0.02	91270.1	3.3590	2.4	0.2631	2.3	0.0926	0.9	0.9304	1494.9	18.9	1505.7	30.4	1479.6	16.9	102
Z24C	493	153	0.31	0.02	95866.7	2.8094	3.0	0.2264	2.9	0.0900	0.9	0.9581	1358.0	22.1	1315.6	34.0	1425.5	16.2	92
Z25C	817	388	0.48	0.01	223235.1	3.1919	1.9	0.2467	1.8	0.0938	0.7	0.9254	1455.2	14.6	1421.6	22.5	1504.6	13.6	94
Z26C	709	273	0.39	0.01	160847.9	3.3667	2.5	0.2642	2.4	0.0924	0.8	0.9424	1496.7	19.4	1511.3	31.7	1476.0	15.8	102
Z26C	132	14	0.10	0.05	26088.3	3.0585	2.7	0.2465	2.4	0.0900	1.1	0.9122	1422.4	20.2	1420.6	31.0	1424.9	20.7	100
Z27R	529	13	0.02	0.01	166471.5	1.9857	2.5	0.1861	2.4	0.0774	0.9	0.9368	1110.7	16.9	1100.4	23.8	1130.9	17.5	97
Z28C	101	14	0.14	0.06	29469.3	3.1058	2.9	0.2458	2.6	0.0916	1.4	0.8830	1434.1	22.1	1416.7	32.6	1460.0	25.7	97
Z30C	294	25	0.09	0.03	52449.9	2.8647	2.1	0.2304	1.7	0.0902	1.2	0.8263	1372.7	15.7	1336.8	21.0	1429.0	22.5	94
Z30C	201	37	0.18	0.04	43820.6	2.4239	2.4	0.2097	2.0	0.0838	1.3	0.8384	1249.7	16.8	1227.4	22.1	1288.4	24.8	95

SAMPLE LOCATIONS:

028-01: 8° 43' 19.0905" N; 74° 05' 44.5400" W
030-02: 8° 47' 20.0881" N; 74° 05' 59.8303" W
017-05: 8° 34' 6.3274" N; 74° 05' 44.9763" W
022-01: 8° 39' 5.0064" N; 74° 05' 39.3947" W
PGG-18: 8° 40' 45.5861" N; 74° 05' 20.9163" W
020-02: 8° 40' 25.2415" N; 74° 05' 48.8510" W
020-03: 8° 40' 25.2415" N; 74° 05' 48.8510" W

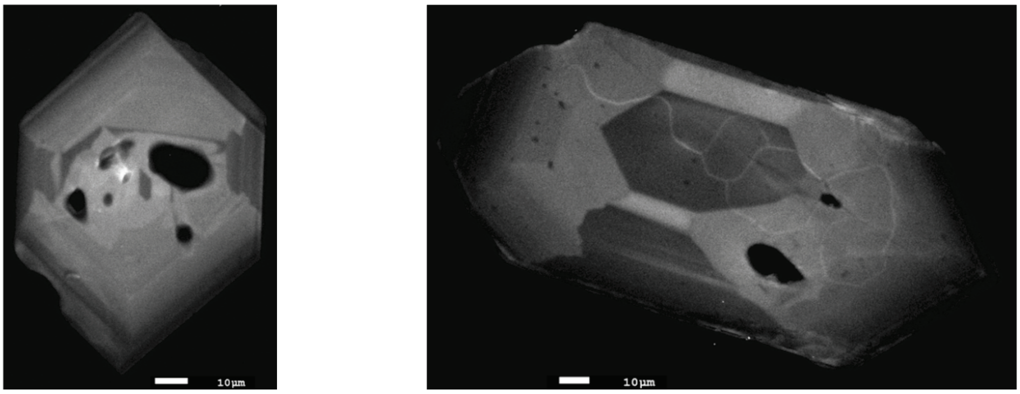

A **B**

Figure 13 – CL images of zircons from granodiorite. OZ, inclusions and complex growth zoning (clear areas at crystal apexes) are common features of zircons from this unit. **A**: zircon from sample 028-01. **B**: zircon from sample 030-01.

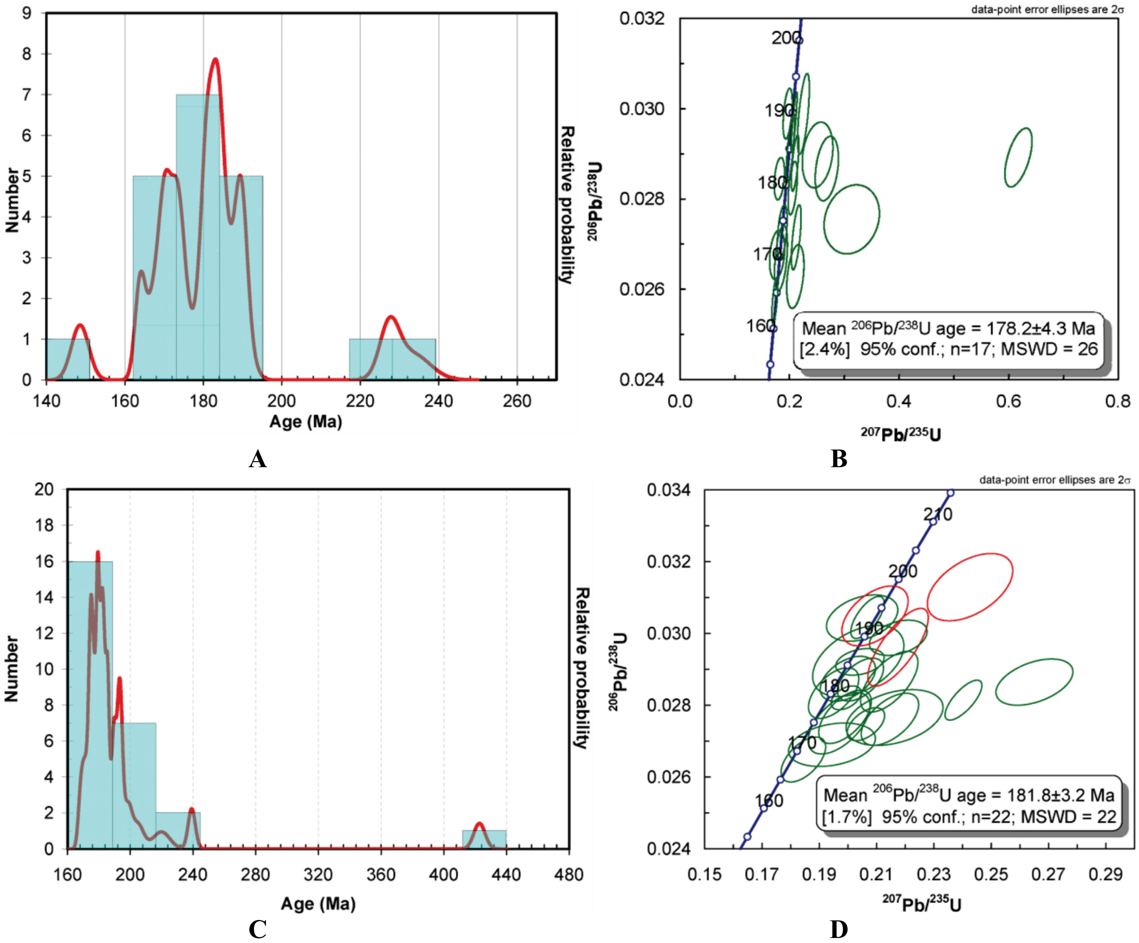

Figure 14 – Results of U-Pb analyses of granodiorite samples. **A**: Probability density plot showing the distribution of zircon ages in sample 028-01. **B**: Concordia diagram of data from sample 028-01. **C**: Probability density plot of zircon ages from sample 030-01. **D**: Concordia diagram of data from sample 030-01. Green ellipsoids: grain cores; Red ellipsoids: grain rims.

growth zoning presented by Corfu *et al*. (2003). The distribution of ^{206}Pb/^{238}U ages in the probability density plots of figures 14A and 14C shows that most of the grains cluster at the interval between 160 and 200 Ma, with some grains displaying ages of

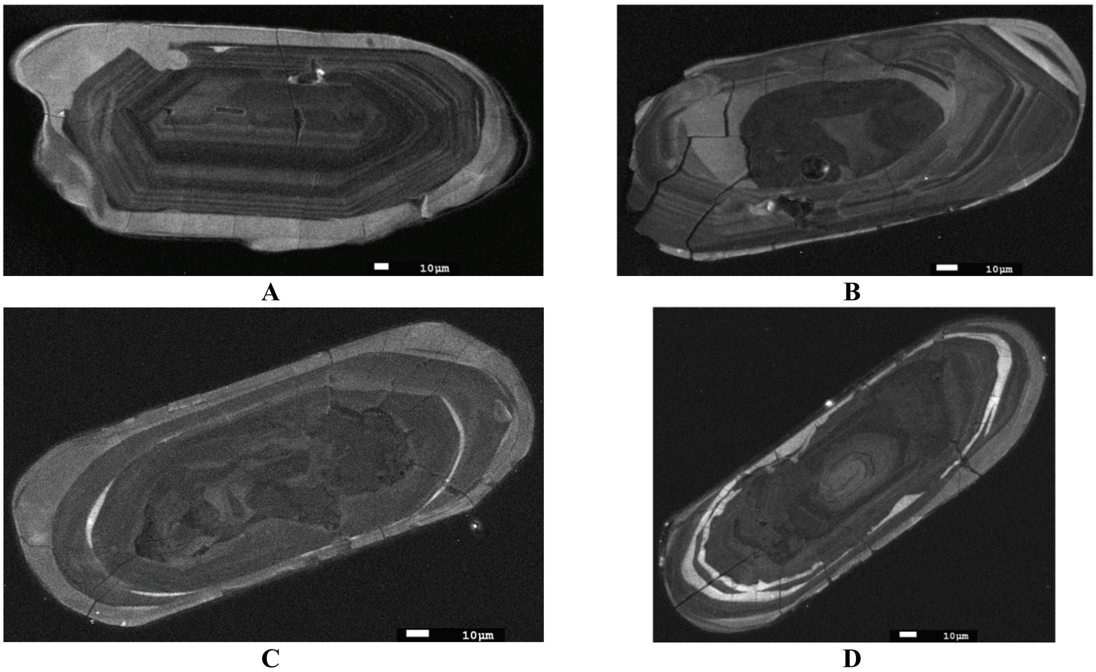

Figure 15 – CL images of zircons from granite-gneiss. **A**: grain displaying internal OZ and bright metamorphic rim with recrystallization front at the upper-left area. **B**: grain displaying dark, convolute-zoned inherited core. **C**: grain with thin metamorphic rim and convolute zoning at the core. **D**: grain displaying bright, thickened primary zones. Some convolute zoning is observed at the lower portion of the crystal.

~149, 200-240 and ~420 Ma. When plotted in concordia diagrams, grains from the main population display a tendency to fall near the concordia although a variation in ^{206}Pb/^{238}U ratios exists. An age between 174 and 185 Ma can be assigned to the granodiorite, which is indicative of the approximate time of crystallization of the magma. Grains yielding older ages, although texturally and morphologically similar to the rest of the grains (some of them, perhaps, displaying a fairly diminished CL), could represent zircons inherited from earlier magmatic pulses. This assumption makes sense when it is taken into account that granodiorites locally display mafic enclaves indicative of magma mingling (see section 4.2.2.5). The grain yielding an age of ~420 Ma could be a xenocryst inherited either from host rocks or from the source of the magma.

4.4.2.2. Granite-gneiss

Zircons from this unit are typically large (between 130 and >150 µm) and elongated (length:width ratios between 2:1 and 3:1), with rounded borders, dark-brown colors and a fragile character. Internally, CL images reveal cores displaying igneous OZ and bright, isotropic metamorphic rims which can be found in some grains and are too thin or virtually inexistent in others. It is common to observe that the igneous OZ has been locally disrupted to variable extents by reequilibration processes manifested in

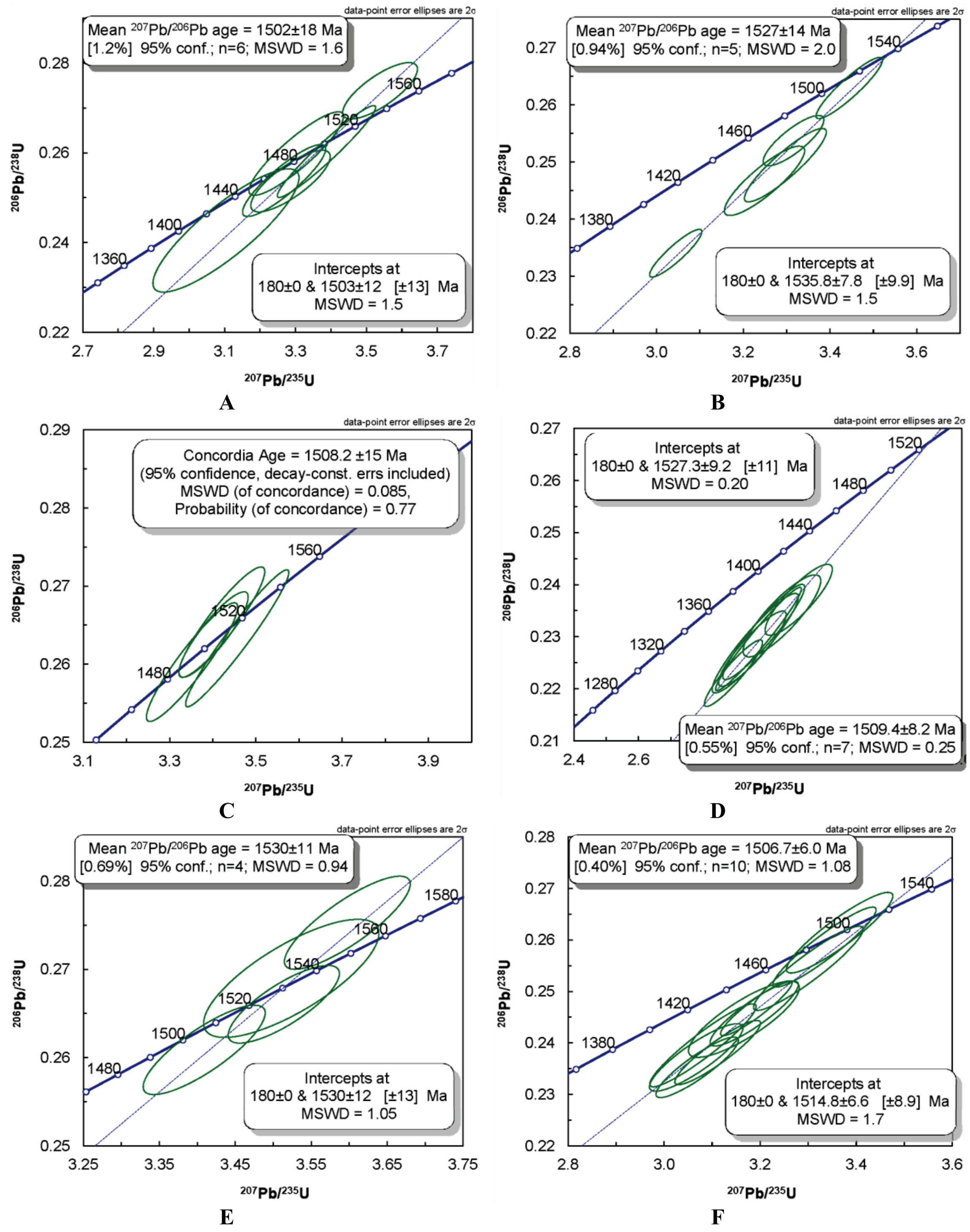

Figure 16 – Results of U-Pb analyses of metamorphic rocks. Samples 017-05 (**A**), 022-01 (**B**) and PGG-18 (**C** and **D**) belong to the granite-gneiss, while samples 020-02 (**E**) and 020-03 (**F**) are from the metamonzogabbro. Green ellipsoids represent analyses of grain cores.

recrystallization fronts, blurred and convolute zoning and thickened primary zones (figure 15), these structures being considered indicative of high grade metamorphism (Hoskin & Black, 2000; Corfu *et al*., 2003). Pb/U ratios show a remarkable dispersion, with ages ranging between ~1542 and 932 Ma and discordant patterns indicating

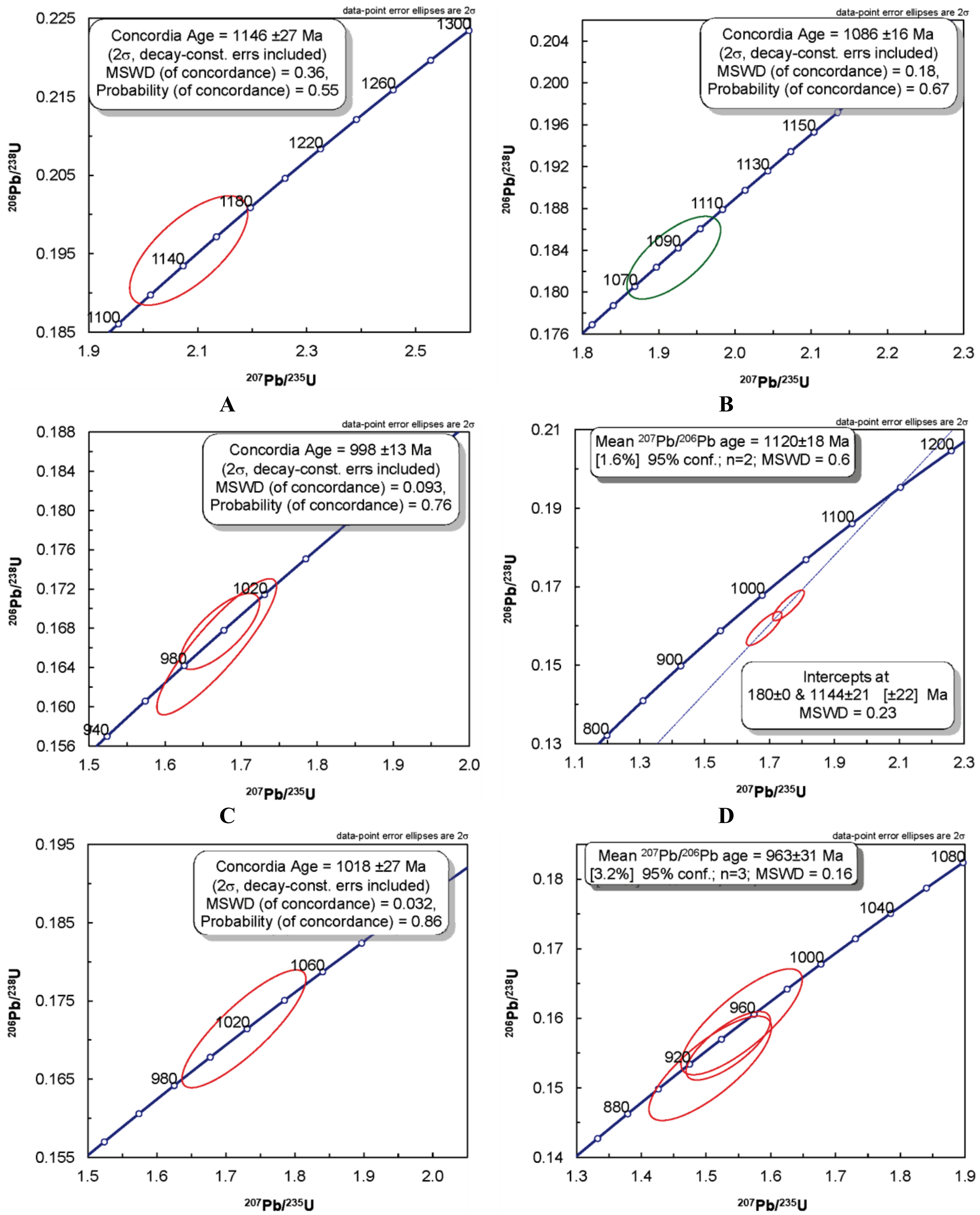

A **B**

C **D**

E **F**

Figure 17 – Results of U-Pb analyses of metamorphic rocks. Samples 017-05 (**A**, **B** and **C**), 022-01 (**D**) and PGG-18 (**E** and **F**) belong to the granite-gneiss. Green ellipsoids: grain cores; Red ellipsoids: grain rims.

conspicuous Pb losses within grains. Few ages between 1560 and ~1900 Ma were obtained, which are interpreted as coming from inherited grains and cores. For the estimation of ages from discordant data, Pb-loss models calculating upper and lower intercepts of discordia lines were applied along with mean ^{207}Pb/^{206}Pb ages to show that in general the two calculation methods yield similar age intervals. Moreover, the lower

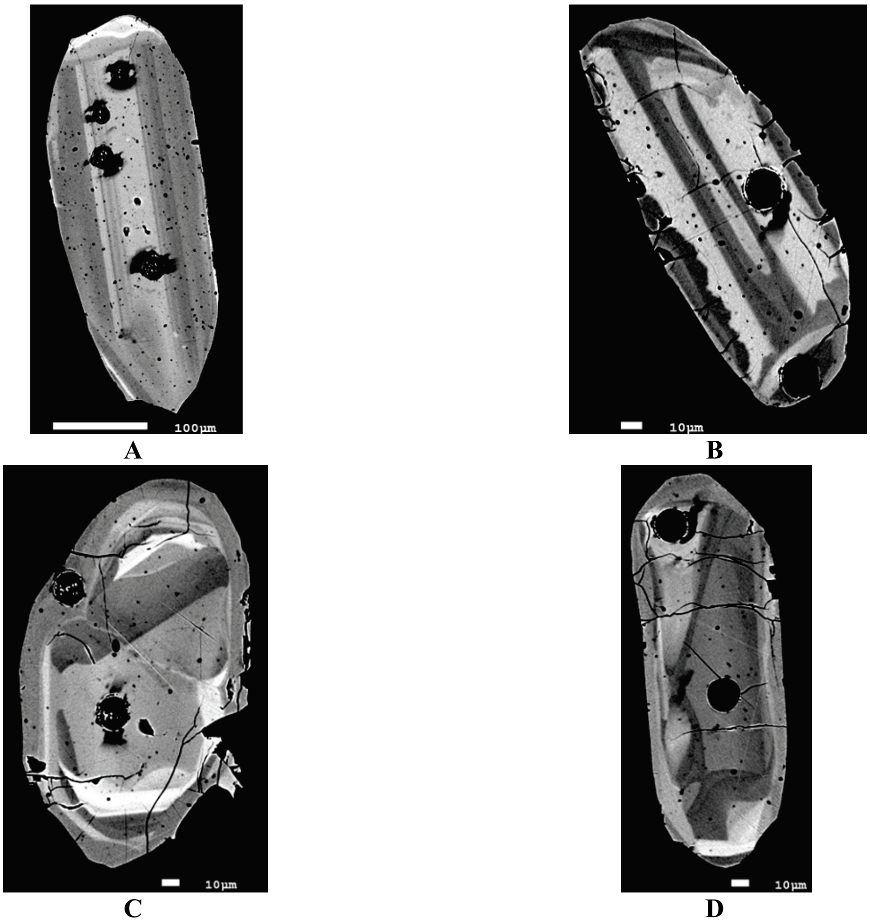

Figure 18 – Back-scattered electron (BSE) images of zircons from metamonzogabbro. **A**: grain displaying patchy zoning. **B**: grain showing patchy zoning and a recrystallization front at its lower-left border. **C**: grain with internal patchy zoning and metamorphic rim. **D**: grain with internal convolute structure. Notice that bright areas in BSE images are dark under CL and vice versa. Circular black spots correspond to ablated areas.

intercept was kept anchored at 180 Ma which is the mean estimated age of intrusion of the granodiorite (see above) and represents the last regional disrupting thermal event suffered by the metamorphic rocks. Using this method, a crystallization age for the igneous protolith is estimated between ~1544 and 1484 Ma (figures 16A - 16D). Some bright rims and one core yielded ages between ~1180 and 970 Ma (figures 17A - 17F), which are interpreted as the time of metamorphism. Intermediate ages between ~1490 and 1200 Ma are regarded as artifacts caused by Pb losses (see discussion section below).

4.4.2.3.Metamonzogabbro

Zircons of this unit are commonly 120 to >150 µm in size with length:width ratios between 2:1 and 1:1. They are translucent with a pinkish hue and display rounded borders which in some cases get to yield prismatic and pyramidal crystal faces. CL

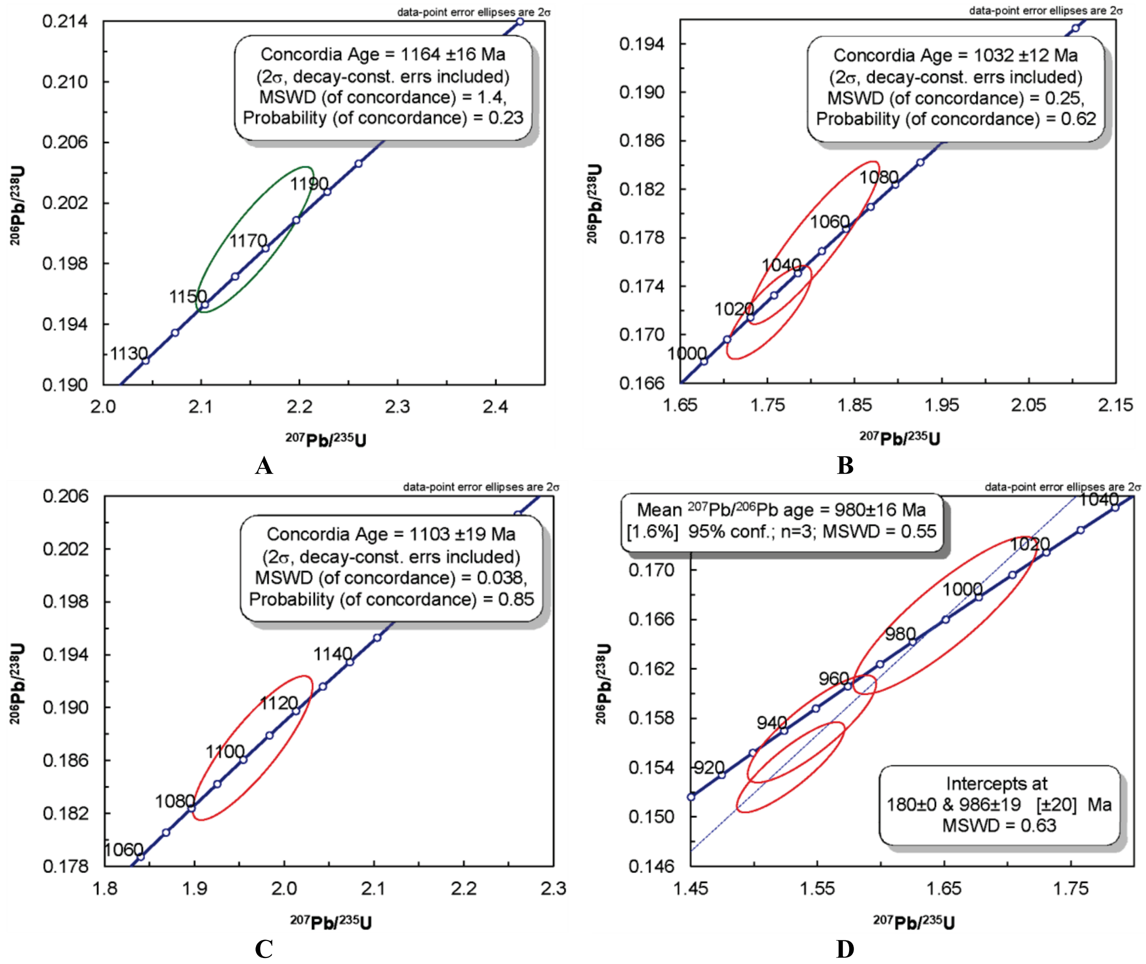

A

B

C

D

Figure 19 – Results of U-Pb analyses of metamorphic rocks. Samples 020-02 (**A** and **B**) and 020-03 (**C** and **D**) belong to the metamonzogabbro. Green ellipsoids: grain cores; Red ellipsoids: grain rims.

imaging reveals internal patchy zoning defining broad light and dark bands that are usually parallel but not concentric (figure 18). This type of texture is similar to that found in zircons from intermediate to mafic igneous rocks (Corfu *et al*., 2003). Metamorphic isotropic rims occasionally occur in these grains, although they might not be as bright as those found in zircons from the granite-gneiss (see above and appendix I). Disequilibrium textures are moderately abundant in the form of recrystallization fronts, convolute zoning and blurred primary structures (figure 18). As in the case of the granite-gneiss, Pb/U ratios display Pb-loss patterns and considerable dispersion yielding ages between ~1542 and 964 Ma. An age of protolith crystallization can be inferred at 1542-1501 Ma (figures 16E - 16F). Metamorphic rims and one core yielded ages between 1180 and 964 Ma which are similar to those obtained in the granite-gneiss, and are thus interpreted as representing the same metamorphic event that affected those rocks (figure 19). As in the case of the granite-gneiss, intermediate ages between >1450

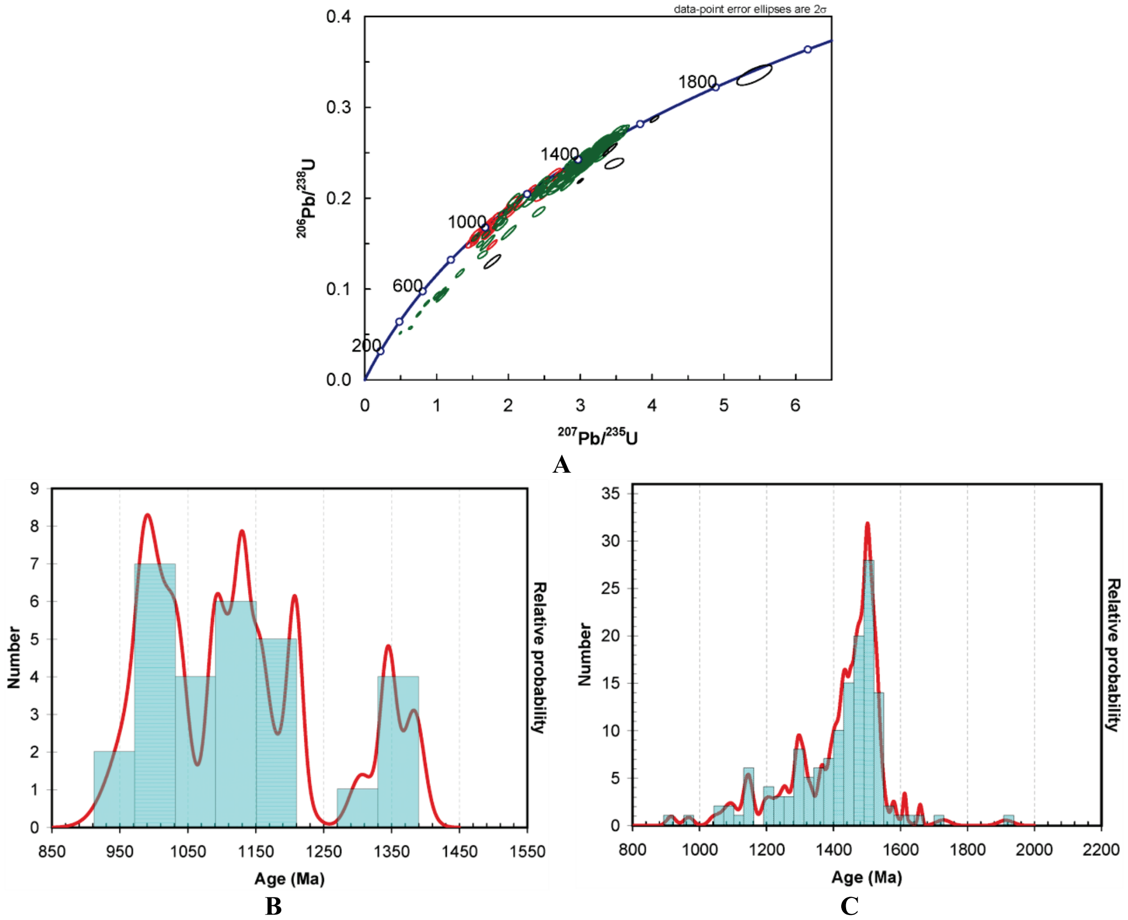

Figure 20 – Summary of U-Pb data from the granite-gneiss and the metamonzogabbro. **A**: Concordia diagram displaying Pb/U ratios of all samples. **B**: Probability density plot of the ages obtained in zircon metamorphic rims of all samples. **C**: Probability density plot of the ages obtained in zircon cores of all samples. Green ellipsoids: grain cores; Red ellipsoids: grain rims; Black ellipsoids: inherited grains.

and 1200 Ma are not regarded to represent real geological events but incomplete reequilibration due to Pb losses.

From the above data, it can be concluded that the oldest ages for the granite-gneiss and the metamonzogabbro (representing the time of crystallization of their protoliths) fall within the same range (~1540-1500 Ma), implying that these units are nearly coeval. This behavior can also be recognized from the concordia diagram when Pb/U ratios of all samples are plotted together (figure 20A) and from the probability density plot of zircon core ages of both rock types (figure 20C). It can also be observed a tendency for metamorphic rims to cluster at ages between 1190 and 1000 Ma (figure 20B).

4.4.3. Nd and Sr isotope geochemistry

Results of Sm-Nd and Rb-Sr isotope geochemistry are summarized in table 3. For the latter system only ^{87}Sr/^{86}Sr ratios were measured in the laboratory, while ^{87}Rb/^{86}Sr

Table 3 – Sm-Nd and Rb-Sr isotope data of the studied samples. Lithologies and locations are given in table 1. Numbers in parentheses next to $^{143}Nd/^{144}Nd$ and $^{87}Sr/^{86}Sr$ ratios correspond to 2σ errors in the last digits. Uncertainties in T_{DM} values were determined from variations produced by uncertainties in $^{143}Nd/^{144}Nd$ ratios.

Sample	**Sm (ppm)**	**Nd (ppm)**	**$^{143}Nd/^{144}Nd$**	**$^{147}Sm/^{144}Nd$**	**$\varepsilon_{Nd}(T)$**	**T_{DM} (Ga)**	**Rb* (ppm)**	**Sr* (ppm)**	**$^{87}Sr/^{86}Sr$**	**$^{87}Rb/^{86}Sr$****	**$^{87}Sr/^{86}Sr_i$*****	**T (Ma)**
021-01	13.529	72.888	0.512033 (±22)	0.1122	+4.7	1.509 (±0.033)	237.4	76.7	0.8588 (±3)	9.1127	0.6638	1520
021-02	16.018	83.933	0.512027 (±14)	0.1154	+3.9	1.567 (±0.022)	221.4	93	0.8361 (±3)	6.9937	0.6864	1520
021-03	12.731	61.901	0.512071 (±15)	0.1243	+3.0	1.648 (±0.025)	113.9	200.9	0.7437 (±2)	1.6507	0.7084	1520
005-01	74.243	363.492	0.512049 (±20)	0.1235	+2.8	1.670 (±0.034)	7.8	401.4	0.7049 (±2)	0.0564	0.7037	1520
020-02	4.735	23.265	0.512139 (±16)	0.123	+4.6	1.511 (±0.027)	48.4	657.5	0.7065 (±2)	0.2136	0.7020	1520
020-03	7.142	32.087	0.512137 (±20)	0.1345	+2.3	1.733 (±0.038)	16.4	646.6	0.7053 (±1)	0.0736	0.7037	1520
029-01	4.748	26.962	0.512176 (±10)	0.1065	-6.9	1.229 (±0.014)	93.3	282.1	0.7097 (±2)	0.9598	0.7073	180
030-02	4.944	24.458	0.512275 (±13)	0.1222	-5.4	1.274 (±0.021)	101.1	327.7	0.7094 (±2)	0.8953	0.7071	180

* Data taken from table 1.

** Calculated ratios.

*** Anomalous values obtained for the granite gneiss will not be considered for interpretations below.

Present-day $^{143}Nd/^{144}Nd_{CHUR}$ and $^{147}Sm/^{144}Nd_{CHUR}$ values used in calculations were 0.512638 and 0.1966, respectively (Jacobsen & Wasserburg, 1980; 1984).

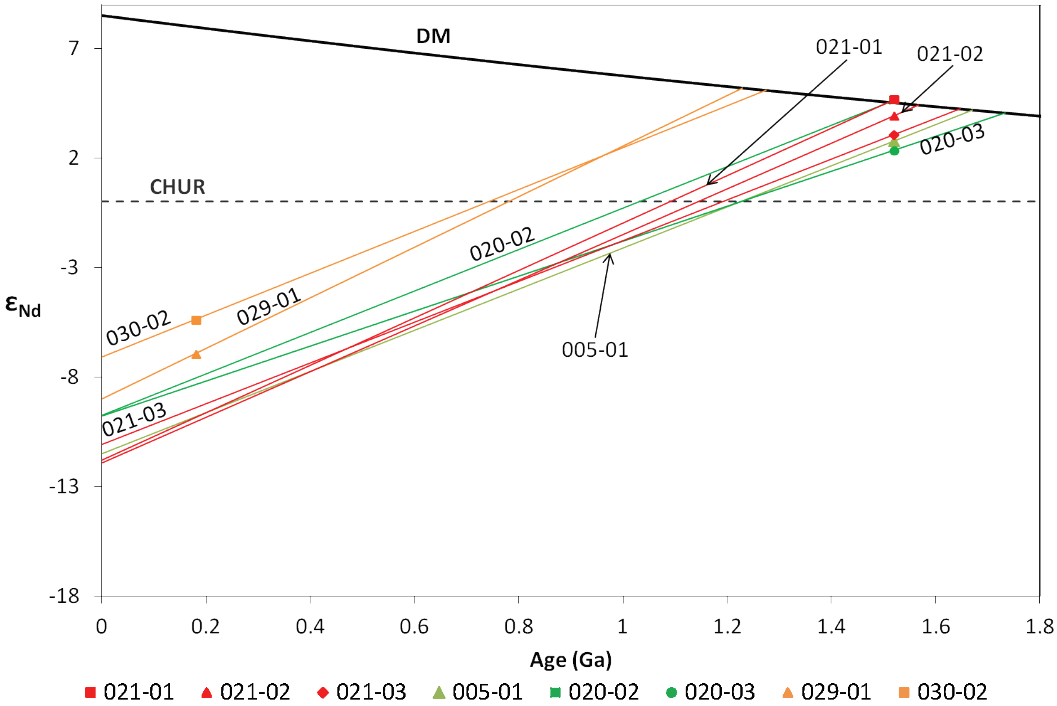

Figure 21 – Evolution ε_{Nd} vs. age diagram of the analyzed samples. Similar evolution trends and T_{DM} ages are observed for the granite-gneiss and the metamafic rocks, with both units being nearly juvenile in nature. Magmas that gave origin to the granodiorite were generated by partial fusion of a more evolved source. Symbol and color key as in figure 9.

ratios were calculated based on the Rb and Sr concentrations presented in section 4.4.1. Unfortunately, these calculations lead to anomalous $^{87}Sr/^{86}Sr_i$ ratios for the granite-gneiss which will not be considered in further interpretations. These anomalies could be due to Rb remobilizations induced by metamorphism or metasomatism of these rocks. From the geochronological data of the previous section, the preferred age for the granite-gneiss, the metamonzogabbro and the amphibolite was taken as 1520 Ma, while an age of 180 Ma was used for the granodiorite. The granite-gneiss yielded $\varepsilon_{Nd}(T)$ values between +3.0 and +4.7, which are indicative of an origin from a depleted mantle reservoir. A similar situation is observed for the metamonzogabbro and the amphibolite, which display $\varepsilon_{Nd}(T)$ values between +2.3 and +4.6, and $^{87}Sr/^{86}Sr_i$ ratios ranging from 0.7020 to 0.7037. T_{DM} ages for this group of rocks roughly fall within the same interval between 1509 and 1733 Ma. The similarity between the lower boundary of this interval and the presumed crystallization age indicate a nearly juvenile character for these mantle-derived rocks, although participation of sources differentiated earlier seems also possible as suggested by the older T_{DM} ages. The latter is supported by the presence of inherited zircons yielding $^{207}Pb/^{206}Pb$ ages between 1600 and 1900 Ma within the granite-gneiss (see above). Altogether, this bimodal set of rocks defines a homogeneous path in the ε_{Nd} vs. age diagram of figure 21.

The granodiorite yielded $\varepsilon_{Nd}(T)$ values of -5.4 and -6.9 and T_{DM} ages of 1229 and 1274 Ma which suggest that this unit was derived from materials with crustal affinities representing a younger, more isotopically evolved source than the metamorphic rocks they intrude (figure 21). The constraint on the crustal nature of the source from which the granodiorites originated is further supported by $^{87}Sr/^{86}Sr_i$ ratios of 0.7071 and 0.7073 for the two analyzed samples.

4.5. DISCUSSION

The granite-gneiss displays high amounts of incompatible trace elements and Ga/Al ratios which allow classifying its protolith as A-type granite according to geochemical criteria by Pearce *et al*. (1984) and Whalen *et al*. (1987). The moderately ferroan nature of these rocks also supports this conclusion, since this is a common feature to that group of granites (Frost *et al*., 2001). Moreover, the analyzed rocks can be assigned to the A_2 subgroup characterized by Y/Nb ratios greater than 1.2, which is related to granites with sources chemically similar to island arc or continental margin basalts (Eby, 1990; 1992). The constraint on a mantle source for the magmas that later became the protolith of the granite-gneiss is further supported by positive values of $\varepsilon_{Nd}(T)$ between +3.0 and +4.7. In addition, it is interesting to notice that within the broad realm of A-type rocks, the granite-gneiss is classified into the post-orogenic/post-collisional category when, for example, considerations about major element contents are taken into account by means of the discriminant functions of Agrawal (1995), and also when the trace element-based tectonic discrimination diagrams of Pearce *et al*. (1984) are used, showing that samples tend to cluster in the WPG field, very close to the boundaries with the other VAG, ORG and Syn-COLG groups, where the post-collisional granites are commonly plotted (Pearce, 1996). Normally, post-collisional granites display heterogeneous chemical compositions that give away interactions between the mantle and a thickened continental crust leading to mixed signatures (Pearce, 1996; Bonin, 2007). The fact that the obtained $\varepsilon_{Nd}(T)$ values still retain a mantle identity would indicate that the crust where the protolith of the granite-gneiss was emplaced did not have such a significant thickness, which is consistent with their multi-element patterns, similar to those of within-plate granites emplaced in attenuated continental lithosphere presented by Pearce *et al*. (1984). Features indicating that a subduction zone-like mantle associated to a previous orogenic phase contributed to sourcing the precursor magmas of the granite-gneiss are the subdued although still noticeable negative anomalies of Nb and Ta. These characteristics, along with MgO/TiO_2 ratios varying between values typical of granites from anorogenic and subduction zone settings (Bilal & Giret, 1999), indicate a transitional character for the source and conditions of generation of the precursor magmas of the granite-gneiss, midway between orogenic/collisional and anorogenic environments. This has been observed by Bonin *et al*. (1998) and Bonin (2007), who describe post-orogenic suites at their initial stages as being the result of processes still influenced by crustal materials subducted below the orogenic subcontinental lithospheric mantle, with the dominantly metaluminous calc-alkaline suites showing a shift from normal to high to very high-K associations, and crystallizing under nearly water-saturated conditions leading to subsolvus mineralogies and textures. This is why post-orogenic suites commonly plot within the A_2 field and display an alkali-calcic character (Bonin *et al*., 1998; Bonin, 2007), such as the granite-gneiss studied here.

On the other hand, the metamafic rocks display a major element chemistry suggesting a transitional character, with the analyzed samples being classified as monzogabbros according to the scheme of De La Roche *et al*. (1980). Their enrichment in LREE precludes an origin at a MORB setting and suggests instead an OIB-like source for the precursor magmas. Similarly, the multi-element diagram patterns of the metamafic rocks resemble that of the mean OIB of Sun & McDonough (1989). Some departures from this mean pattern are observed on the analyzed rocks; according to Sun & McDonough (1989), influence of arc-related or sedimentary materials on the source of the magmas could be responsible for the depletions in Nb, Ta, Sr, P, Eu and Ti, as well as for the enrichment in Ba, while the lower contents of Rb and K could account for residual phlogopite holding back these elements at the mantle. Melting at high pressures would cause the observed depletions in Zr and Hf as well as, again, in Sr, P and Ti. Mantle rocks at depths greater than ~30 km are unlikely to be composed of abundant plagioclase (Wilson, 1989), so that high-pressure melting could also explain the subdued to almost null negative europium anomaly observed in the REE patterns of the metamafic rocks. In addition, high water amounts evidenced by relatively abundant hornblende and biotite (the latter observed in the lower-grade lithologies) also point to subduction zone mantle as participant in the generation of the magmas. Altogether, the source of the metamafic rocks seems to be complex in nature involving more than one kind of material; this is also reflected by their variable Nd T_{DM} between 1.51 and 1.73 Ga.

The U-Pb ages in zircons obtained from the granite-gneiss and the metamafic rocks range between ~1540 and 930 Ma, with noticeable Pb losses and intermediary ages ranging from 1200 to >1400 Ma. As shown in figure 20B, most of the ages determined in the metamorphic rims of zircons from both units fall within the range between ~1180 and 930 Ma, which is interpreted as due to a high-grade Grenvillian metamorphic event related to the assembly of Rodinia at the end of the Mesoproterozoic (*e.g.*, Li *et al.*, 2008; Fuck *et al.*, 2008). This is not a new finding for the region comprising the northern portion of the Central Cordillera of Colombia, as previous works had already yielded similar results at this and other areas of the Colombian Andes (Restrepo-Pace *et al.*, 1997; Ordóñez-Carmona *et al.*, 1999, 2002b; Cordani *et al.*, 2005; Cardona *et al.*, 2010a; Ibáñez-Mejía *et al.*, 2011). On the other hand, the oldest ages obtained from zircon cores (except those from inherited grains) range between ~1500 and 1540 Ma, and are interpreted as the time of crystallization of the protoliths of both the granite-gneiss and the metamafic group, which are thus essentially coeval. Several ages between 1200 and >1400 Ma can be estimated using Pb-loss models and $^{207}Pb/^{206}Pb$ means. However, from a geological point of view, no rocks representing events of those ages have been reported so far in this part of the Central Cordillera, so these results would represent artifacts induced by multi-stage Pb losses caused initially by the Grenvillian metamorphism and later by the thermal disturbance associated to the intrusion of the Norosí Batholith at ~180 Ma. Furthermore, if a thermal event had indeed taken place close to ~1300 Ma, then it should be equally represented in both the granitic and mafic rocks, which is not the case for the granite-gneiss. Concordant ages of zircon cores and rims falling within this interval are thus interpreted as “protolith memory” effects caused by incomplete reequilibration of Pb/U ratios within zircon. This has been shown to be a common feature in zircons of rocks from high-grade terranes (Hoskin & Black, 2000).

The Norosí Batholith granodiorite has mineralogical and chemical features consistent with an I-type nature. Negative $\varepsilon_{Nd}(T)$ values and initial $^{87}Sr/^{86}Sr$ ratios greater than 0.7045, however, suggest the participation of crustal, more evolved materials in their genesis. Some authors have pointed out the hybrid character of several granitic rocks in the world, with the mixing between mafic mantle-derived melts and felsic crustal-derived magmas being the usually preferred model to explain the dual identity of those rocks, although other mechanisms valid in specific instances have also been proposed (Castro *et al*., 1991; Healy *et al*., 2004; Yang *et al*., 2006; Clemens *et al*., 2011). The presence of common mafic enclaves supports a magma mixture model for the origin of the granodioritic rocks in the SLR. Furthermore, from the results shown in table 3, it can be calculated that the ε_{Nd} values for the granite-gneiss and the metamafic rocks at ~180 Ma (the presumed age of generation of the magmas from which the granodiorite crystallized) varies between -8 and -10, thus being plausible end members that when melted and mixed with mantle-derived magmas (ε_{Nd} of *ca.* +8 at 180 Ma according to the depleted mantle model of De Paolo, 1981) might yield hybrid melts with the ε_{Nd} values between -5 and -7 displayed by the granodiorite (table 3). This implies that the Nd T_{DM} of *ca.* 1250 Ma calculated for that unit is an artifact resulting from mixing magmas derived from sources with T_{DM} of ~1500 Ma (granite-gneiss and metamafic rocks) and ~180 Ma (mafic magmas generated during Andean igneous activity).

$\varepsilon_{Nd}(T)$ values between +2.3 and +4.6 for the metamafic rocks are similar to those of the granite-gneiss indicating a mantle source common to both rock types. In addition, their Nd T_{DM} values are similar and define a homogeneous domain in figure 21, with protolith ages being close to this range. The latter suggests that those magmas are nearly juvenile in nature and constitute a bimodal association which, according to the characteristics described above, would have been emplaced in a post-collisional regime at ~1.52 Ga.

Bimodal A-type associations are a rather common feature of post-collisional settings which are frequently linked to transcurrent shear tectonic contexts (Bonin, 2007). With regard to this, several examples exist in the literature describing A-type granites and associated rocks that were likely emplaced in compressive-transpressive regimes as, for example, the Estrela Granite Complex of Carajás in Brazil (Barros, *et al*., 2001; 2009), the granitic rocks west of the East European Craton (Skridlaite *et al*., 2003) and the Stenshuvud and Karlshamn granites of southern Sweden (Čečys, 2004). At such settings, the granitic magmas are prone to develop anisotropic fabrics consistent with syntectonic deformation. Some granites even display chemical characteristics midway between I- and A-types (Čečys, 2004). In this sense, the anorogenic nature of those rocks is questioned as they reflect a relation more compatible to orogenic contexts. It is suggested that the banded structure defined by alternating felsic and mafic layers observed in the granite-gneiss of the SLR could have been originated in a similar fashion to explain their apparent truncation by the nearly coeval and virtually isotropic metamafic rocks (figure 3B). According to Naslund & McBirney (1996), deformation of partially crystallized magmas can generate a layering resulting from the segregation of liquids, yielding sharply defined dark and light layers that can in extreme cases be monomineralic, although magmatic flow is also capable of generating this kind of structures. Actually, no solid statement can be made about the nature and origin of the banded structure of the granite-gneiss as detailed structural and kinematic analyses were not conducted. This issue is left to be resolved during future studies involving more field observations. A Nd T_{DM} of 0.6 Ga for a deformed metagabbro dyke found near Pueblito Mejía would suggest that the truncation of the banding of the granite-gneiss is caused by younger mafic intrusions (INGEOMINAS-UIS, 2006). The latter data, however, are considered unreliable since no rocks of that age have been found at this sector of the Colombian Andes and no metamorphism younger than the Grenvillian event has been documented within the area by previous studies.

The Rio Negro Province (RNP) of the Amazonian Craton, comprising northwestern Brazil, southeastern Colombia and southern Venezuela, has a basement composed of calc-alkalic monzogranitic to tonalitic gneisses yielding ages between 1.86 and 1.78 Ga (Tassinari & Macambira, 1999; Santos *et al.*, 2000). This basement is intruded, among other units, by granitic rocks of the Rio Uaupés Suite, including titanite-biotite monzogranite, biotite granodiorite, leuco-monzogranite and leuco-syenogranite (Dall'Agnol & Macambira, 1992). These granites have yielded a Rb-Sr whole-rock age of ~1459 Ma (Dall'Agnol & Macambira, 1992), although Santos *et al.* (2000) reported older U-Pb ages in zircon close to 1520 Ma, as well as $\varepsilon_{Nd}(T)$ values between -5.0 and -1.22 with Nd T_{DM} ranging from 1.99 to 2.12 Ga. Based on an initial $^{87}Sr/^{86}Sr$ ratio of 0.7063 obtained for this suite, Dall'Agnol & Macambira (1992) proposed a probable origin in a collisional setting for the Rio Uaupés Granites. Geochemically, however, these granites display within-plate and A-type characteristics, falling within the A_2 group of Eby (1992). Further geochemical data presented by Dall'Agnol (1992) showed that the rocks of this suite display features similar to those of both orogenic and anorogenic granites, without clearly fitting within any of these two classes. Thus, Dall'Agnol (1992) recognized that the Rio Uaupés granites would not represent typical collisional granites and leaves an open question about a possible relation to a post-collisional/anorogenic setting. Given the above characteristics, it might be stated in principle a correlation between the granite-gneiss of the SLR and the Rio Uaupés Suite, thus establishing a linkage to the RNP of the Amazonian Craton. Some important differences should, however, be pointed out, such as the apparently crustal origin of the Rio Uaupés Suite, as well as their consequently older Nd model ages and absence of associated mafic rocks. Moreover, the Uaupés River Suite is associated to the coeval Rio Içana Suite, composed of peralumious S-type granites (Dall'Agnol, 1992; Santos *et al.*, 2000). On the other hand, Dall'Agnol (1992) does not discard a mantle source with substantial later crustal contribution for the origin of the Rio Uaupés granites, and inherited zircons with ages between ~1900 and 1600 Ma found within the granite-gneiss support a genetic relationship to the RNP of the Amazonian Craton. A similar correlation had been stated by Cardona *et al.* (2010a) on geochronological grounds for paraderived units from the Chibcha Terrane in Colombia and other similar lithospheric blocks in Ecuador, Perú and Venezuela, which were interpreted as generated from sediments coming from the Amazonian Craton and deposited in basins along an active margin of the latter. Moreover, paleomagnetic data from Bayona *et al.* (2006; 2010) suggest that the Colombian massifs were brought from latitudes further south similar to the present day positions of northern Perú and Ecuador, thus favouring the correlation with the RNP stated here for the Mesoproterozoic rocks of the SLR. The determination of ages between ~1180 and 930 Ma in metamorphic rims of zircons of the granite-gneiss and the metamafic rocks advocate the participation of the SLR in a Grenvillian event along with the other massifs of the Chibcha Terrane in the Colombian Andes and other blocks in Ecuador, Perú, Venezuela, Mexico and Middle America, following recent models in which this group of fragments would have been located at or near the northwestern border of Amazonia interacting with Baltica during the end of the Mesoproterozoic and Early Neoproterozoic (Keppie & Dostal, 2007; Bogdanova *et al.*, 2008; Li *et al.* 2008; Johansson, 2009; Keppie & Ortega-Gutiérrez, 2010; Cardona *et al.*, 2010a; Ibáñez-Mejía *et al.*, 2011).

It is worthwhile to notice that this work describes comprehensively for the first time Early Mesoproterozoic (Calymmian) orthoderived rocks in the Chibcha Terrane, as materials of this age (*i.e.*, zircons) had only be found as inherited components in paraderived metamorphic rocks reworked during Grenvillian events (e.g., Restrepo-Pace *et al*., 1997; Cordani *et al*., 2005; Ordóñez-Carmona *et al*., 1999; 2002b; Cardona *et al*., 2010a; Ibáñez-Mejía *et al*., 2011). Ordóñez-Carmona *et al*. (2009) had already reported an U-Pb age in zircon of 1501 Ma for the granite-gneiss, but its meaning and geotectonic context was poorly documented. The San Lucas Gneiss and metamafic rocks as part of the more broadly extended post-collisional to anorogenic domain of the RNP of the Amazonian Craton would represent, in fact, the source of zircons with ages close to 1.5-1.54 Ga found within the Precambrian units of the Colombian Andes. This means that the rocks of the SLR constitute the true basement of those Precambrian terranes in this region, with the paraderived rocks reported by earlier works representing supracrustal covers.

4.6. CONCLUSIONS

The analyses carried out during this study allow concluding the following:

- The basement of the northern portion of the SLR is constituted by a bimodal association of monzogranitic and monzogabbroic rocks that were metamorphosed under granulite facies and retrograded subsequently to amphibolite facies. Thus, the classical conception that regarded these units as a metasedimentary sequence similar to those observed in the eastern flank of the Central Cordillera, the Sierra Nevada de Santa Marta and Santander Massifs and the Guajira Peninsula is challenged.
- U-Pb geochronology of zircon cores indicates a crystallization age between 1.54 and 1.50 Ga for the protoliths of the granite-gneiss and the metamafic rocks, while metamorphic rims yielded ages between 1180 and 930 Ma. These data, along with positive $\varepsilon_{Nd}(T)$ values and T_{DM} between 1.5 and 1.7 Ga indicate a mantle-derived origin and a virtually juvenile character for those coeval units.
- The magma from which the granodiorite of the Norosí Batholith crystallized seems to be the result of mixing between mafic mantle-derived magmas and felsic crustal melts generated between 200 and 180 Ma ago.
- Both groups of metamorphosed felsic and mafic rocks display chemical features suggesting that the mantle source that gave origin to their precursor magmas had characteristics transitional between enriched (indicative of a within-plate setting) and both depleted and hydrated (more compatible with an arc setting), which suggests that these magmas formed as a bimodal association in a post-collisional context. Moreover, their occurrence in a transpressive environment (as exemplified by other suites from

Northeastern Europe and Brazil) might account for a rather syntectonic character reflected in the banded structure of the granite-gneiss which seems to be crosscut by the metamafic rocks. Nevertheless, further structural and petrologic studies should verify the validity of the latter statement.

- The orthoderived rocks of the northern part of the SLR constitute the first reported occurrence of Early Mesoproterozoic (Calymmian) in the Colombian Andes, as similar (and even older) ages had only been found by previous studies in detrital zircons of younger Late Mesoproterozoic-Early Neoproterozoic paraderived metamorphic rocks.
- The post-collisional granitic rocks described in this study can be correlated with the A-type Rio Uaupés Suite in the RNP of the Amazonian Craton, for which an intrusion age has been constrained at ~1520 Ma. This places the SLR within the same context of other massifs in the Colombian Andes as well as similar lithospheric blocks in Ecuador, Perú, Venezuela, Mexico and Middle America, all of them regarded as being at or near the northwestern border of the Amazonian Craton during the Late Mesoproterozoic. The SLR, however, would represent a part of the basement of the Amazonia paleocontinent, while the other blocks mainly correspond to sedimentary infillings of marginal basins or peripheral arcs and/or microcontinents. According to recent models, this group of blocks might have been brought from southern latitudes after being involved in the collision between Amazonia and Baltica during the Grenvillian/Sveconorwegian Orogeny from ~1140 to 970 Ma.

4.7. ACKNOWLEDGEMENTS

This work was possible thanks to financial support from the Coordenação de Aperfeiçoamento de Pessoal de Nível Superior (CAPES) and the Conselho Nacional de Desenvolvimento Científico e Tecnológico (CNPq) from Brazil. We also thank the Gemma Group of the Universidad Nacional de Colombia –Sede Medellín– for its financial support during the field work. Valuable comments on geochronological and isotope data treatment and regional correlations from Professors Massimo Matteini and Moacir Macambira are specially acknowledged, as well as enlightening observations on petrology of mafic rocks from Prof. César Fonseca Ferreira Filho and Senior Geologist Reinaldo Santana Correia de Brito from the Brazilian Geological Survey. Assistance from the technical staff of the Geochronology and Petrography laboratories of the University of Brasília is also thankfully acknowledged.

CAPÍTULO 5: CONCLUSÕES

As análises realizadas durante este estudo permitem concluir o seguinte:

- O embasamento da porção norte da SSL é constituído por uma associação bimodal de rochas monzograníticas e monzogabróicas que foram metamorfizadas em fácies granulito e retrogradadas posteriormente a fácies anfibolito. Assim, a concepção clássica que considera estas unidades como uma sequência metasedimentar similar àquelas observadas na margem leste da Cordilheira Central, nos Maciços da Serra Nevada de Santa Marta e Santander e na Península da Guajira é contestada.

- A geocronologia de U-Pb em núcleos de zircão indica idades de cristalização entre 1.54 e 1.50 Ga para os protólitos do granito-gnaisse e as rochas metamáficas, enquanto que as bordas metamórficas apresentaram idades entre 1180 e 930 Ma. Estes dados, junto com valores positivos de $\varepsilon_{Nd}(T)$ e T_{DM} entre 1.5 e 1.7 Ga indicam uma origem a partir do manto e um caráter virtualmente juvenil para essas unidades coetâneas.

- O magma a partir do qual cristalizou o granodiorito do Batólito de Norosí parece ser o resultado de mistura entre magmas máficos manto-derivados e fundidos félsicos crustais gerados há 200-180 Ma.

- Os dois grupos de rochas félsicas e máficas metamorfizadas apresentam feições químicas indicando que a fonte mantélica que deu origem aos seus magmas precursores tinha características transicionais entre enriquecidas (indicativo de um ambiente intra-placa) e empobrecidas e hidratadas (mais compatível com um ambiente de arco), sugerindo que esses magmas foram gerados como uma associação bimodal num contexto pós-colisional. Mais ainda, a sua ocorrência num ambiente transpressivo (como exemplificado por outras suítes do nordeste da Europa e do Brasil) poderia dar conta de um caráter sintectônico refletido na estrutura bandada do granito-gnaisse que parece ser cortada pelas rochas metamáficas. Porém, estudos estruturais e petrológicos mais detalhados deveriam verificar a validade desta última afirmação.

- As rochas ortoderivadas da parte norte da SSL constituem a primeira ocorrência reportada de Mesoproterozóico Inferior (Calymmiano) nos Andes Colombianos, visto que idades similares (e até mais antigas) só tinham sido obtidas por trabalhos anteriores em zircões detríticos de rochas metamórficas paraderivadas mais jovens do Mesoproterozóico Superior-Neoproterozóico Inferior.

- As rochas graníticas pós-colisionais descritas neste estudo podem ser correlacionadas com a Suíte Granítica tipo A do Rio Uaupés na PRN do Cráton Amazônico, para a qual foi sugerida uma idade de intrusão de ~1520 Ma. Isto coloca a SSL no mesmo contexto de outros maciços dos Andes Colombianos e de blocos litosféricos similares no Equador, Perú, Venezuela, México e América Central, todos eles considerados como localizados em ou muito próximos da borda noroeste do Cráton Amazônico durante o Mesoproterozóico Tardio. A SSL, no entanto, representaria uma parte do embasamento do paleocontinente Amazônia, enquanto que os outros blocos correspondem principalmente a enchimentos sedimentares de bacias marginais ou arcos periféricos e/ou microcontinentes. Segundo modelos recentes, estes blocos puderam ser trazidos desde latitudes mais meridionais após serem envolvidos na colisão entre Amazônia e Báltica durante a Orogenia Grenvilliana/Sveconorueguesa entre ~1140 e 970 Ma.

REFERÊNCIAS BIBLIOGRÁFICAS

Acosta, J., Velandia, F., Osório, J., Lonergan, L., Mora, H. 2007. Strike-slip deformation within the Colombian Andes. Em: Ries, A.C., Butler, R.W.H., Graham, R.H. (Eds.). Deformation of the Continental Crust: The Legacy of Mike Coward. Geological Society of London, Special Publications, (272): 303-319.

Agrawal, S. 1995. Discrimination between late-orogenic, post-orogenic, and anorogenic granites by major element compositions. The Journal of Geology, (103): 529-537.

Alemán, A., Ramos, V.A. 2000. Northern Andes. Em: Cordani, U.G., Milani, E.J., Thomaz-Filho, A., Campos, D.A. (Eds.). Tectonic evolution of South America. 31st International Geological Congress, Rio de Janeiro. p. 453-480.

Álvarez, J. 1981. Determinación de la edad Rb-Sr en rocas del Macizo de Garzón, Cordillera Oriental de Colombia. Geología Norandina, (4): 31-38.

Álvarez, W. 1967. Geology of the Simarua and Carpintero areas, Guajira Peninsula, Colombia. PhD. Thesis, Princeton University. 168 p.

Amelin, Y., Rotenberg, E. 2004. Sm-Nd systematics of chondrites. Earth and Planetary Science Letters, (223): 267–282.

Arculus, R.J. 2003. Use and abuse of the terms calcalkaline and calcalkalic. Journal of Petrology, 44(5): 929-935.

Barrero, D. 1979. Geology of the central Western Cordillera west of Buga and Roldanillo, Colombia. INGEOMINAS, Publ. geol. esp., (4): 1-75.

Barros, C.E.M., Barbey, P., Boullier, A.M. 2001. Role of magma pressure, tectonic stress and crystallization progress in the emplacement of syntectonic granites. The A-type Estrela Granite Complex (Carajás Mineral Province, Brazil). Tectonophysics, (343): 93–109.

Barros, C.E.M., Sardinha, A.S., Barbosa, J.D.P., Macambira, M.J.B., Barbey, P., Boullier, A.M. 2009. Structure, petrology, geochemistry and zircon U-Pb and Pb-Pb geochronology of the synkinematic Archean (2.7 Ga) A-type granites from the Carajás metallogenic province, northern Brazil. The Canadian Mineralogist, (47): 1423-1440.

Bayona, G., Cardona, A., Jaramillo, C., Mora, A., Montes, C., Valencia, V., Ayala, C., Montenegro, O., Ibáñez-Mejía, M. 2012. Early Paleogene magmatism in the northern Andes: Insights on the effects of Oceanic Plateau–continent convergence. Earth and Planetary Science Letters (331-332): 97–111.

Bayona, G., Jiménez, G., Silva, C., Cardona, A., Montes, C., Roncancio, J., Cordani, U.G. 2010. Paleomagnetic data and K–Ar ages from Mesozoic units of the Santa Marta massif: A preliminary interpretation for block rotation and translations. Journal of South American Earth Sciences, (29): 817–831.

Bayona, G., Rapalini, A.E., Costanzo-Álvarez, V. 2006. Paleomagnetism in Mesozoic rocks of the northern Andes and its implications in Mesozoic tectonics of northwestern South America. Earth Planets and Space, (58): 1255–1272.

Best, M.G. 2003. Igneous and metamorphic petrology. 2nd edition. Blackwell Publishing. 729 p.

Bettencourt, J.S., Payolla, B.L., Leite Junior, W.B., Tosdal, R.M., Spiro, B. 1999a. Mesoproterozoic rapakivi granites of Rondônia Tin Province, southwestern border of Amazonian Craton, Brazil: Reconnaissance Nd, Sr, O, Pb isotopic geochemistry and regional implications. Em: Barbarin, B. (Ed.). Fourth Hutton Symposium: Clermont Ferrand, França. Abstracts, Documents du BRGM 290. 132 p.

Bettencourt, J.S., Tosdal, R.M., Leite, W.B., Jr., Payolla, B.L. 1999b. Mesoproterozoic rapakivi granites of the Rondônia Tin Province, southwestern border of the Amazonian Craton, Brazil— I. Reconnaissance U–Pb geochronology and regional implications. Precambrian Research, (95): 41–67.

Bilal, E., Giret, A. 1999. The aluminum saturation index and the MgO/TiO_2 ratio: two parameters influenced by PH_2O and their use to discriminate magma series. Revista Brasileira de Geociências, 29(1): 55-58.

Bingen, B., Nordgulen, O., Viola, G. 2008. A four-phase model for the Sveconorwegian orogeny, SW Scandinavia. Norwegian Journal of Geology, (88): 43-72.

Bogdanova, S.V., Bingen, B., Gorbatschev, R., Kheraskova, T.N., Kozlov, V.I., Puchkov, V.N., Volozh, Y.A. 2008. The East European Craton (Baltica) before and during the assembly of Rodinia. Precambrian Research, (160): 23–45.

Bogotá, J., Aluja, J. 1981. Geología de la Serranía de San Lucas. Geología Norandina, (4): 49-55.

Bonin, B. 2007. A-type granites and related rocks: evolution of a concept, problems and prospects. Lithos, (97): 1-29.

Bonin, B., Azzouni-Sekkal, A., Bussy, F., Ferrag, S. 1998. Alkali-calcic and alkaline post-orogenic (PO) granite magmatism: petrologic constraints and geodynamic settings. Lithos, (45): 45-70.

Botero, G. 1940. Geología sobre el Ordoviciano de Antioquia. Rev. Minería, Medellín, (17): 8249–8256.

Botero, G. 1975. Edades radiométricas de algunos plutones colombianos. Rev. Minería, Medellín, (27): 8886-8842.

Bühn, B., Pimentel, M.M., Matteini, M., Dantas, E.L. 2009. High spatial resolution analysis of Pb and U isotopes for geochronology by laser ablation multi-collector inductively coupled plasma mass spectrometry (LA-MC-ICP-MS). Anais da Academia Brasileira de Ciências, 81(1): 99-114.

Bustamante, A., Juliani, C. 2011. Unraveling an antique subduction process from metamorphic basement around Medellín city, Central Cordillera of Colombian Andes. Journal of South American Earth Sciences, (32): 210-221.

Cardona, A., Chew., D., Valencia, V.A., Bayona, G., A. Mišković, A., Ibáñez-Mejía, M. 2010a. Grenvillian remnants in the Northern Andes: Rodinian and Phanerozoic paleogeographic perspectives. Journal of South American Earth Sciences, (29): 92-104.

Cardona, A. Cordani, U.G., MacDonald, W.D. 2006. Tectonic correlations of pre-Mesozoic crust from the northern termination of the Colombian Andes, Caribbean region. Journal of South American Earth Sciences, (21): 337–354.

Cardona, A., García-Casco, A., Ruiz, J., Valencia, V., Bustamante, C., Garzón, A., Saldarriaga, M., Weber, M. 2008. Late Cretaceous Caribbean–South America interactions: insights from the metamorphic record of the NW Sierra Nevada de Santa Marta, Colombia. 18th Caribbean Geological Conference, Santo Domingo, República Dominicana, 24–29 March. (Abstracts and Program). p. 12.

Cardona, A. Valencia, V., Bustamante, C., García-Casco, A. Ojeda, G., Ruiz, J., Saldarriaga, M., Weber, M. 2010b. Tectonomagmatic setting and provenance of the Santa Marta Schists, northern Colombia: Insights on the growth and approach of Cretaceous Caribbean oceanic terranes to the South American continent. Journal of South American Earth Sciences, (29): 784–804.

Castro, A., Moreno-Ventas, I., de la Rosa, J.D. 1991. H-type (hybrid) granitoids: a proposed revision of the granite-type classification and nomenclature. Earth-Science Reviews, (31): 237-253.

Čečys, A. 2004. Tectonic implications of ca. 1.45 Ga granitoid magmatism at the southwestern margin of the East European Craton. Doctoral thesis. Lund University, Sweden. 25 p. + 4 articles.

Cediel, F., Restrepo, I., Marín-Cerón, M.I., Duque-Caro, H., Cuartas, C., Mora, C., Montenegro, G., García, E., Tovar, D., Muñoz, G. 2010. Geology and Hydrocarbon Potential, Atrato and San Juan Basins, Chocó (Panamá) Arc. Tumaco Basin (Pacific Realm), Colombia. Fondo Editorial Universidad EAFIT, Medellín, Colombia. 172 pp.

Cediel, F., Shaw, R.P., Cáceres, C. 2003. Tectonic assembly of the Northern Andean Block. Em: Bartolini, C., Buffler, R.T., Blickwede, J. (Eds.). The Circum-Gulf of Mexico and the Caribbean: Hydrocarbon habitats, basin formation, and plate tectonics. AAPG Memoir (79): 815– 848.

Clemens, J.D., Stevens, G., Farina, F. 2011. The enigmatic sources of I-type granites: the peritectic connexion. Lithos, (126): 174-181.

Condie, K.C. (Ed.). 1992. Proterozoic crustal evolution. Developments in Precambrian Geology, 10. Elsevier Science Publishers B.V. 537 p.

Condie, K.C. 2005. Earth as an evolving planetary system. 2nd edition. Elsevier Ltd. 574 p.

Coney, P.J., Jones, D.L., Monger, J.W.H. 1980. Cordilleran suspect terranes. Nature, (288): 329-333.

Cordani, U.G., Cardona, A., Jiménez, D.M., Liu, D., Nutman, A.P. 2005. Geochronology of Proterozoic basement inliers in the Colombian Andes: tectonic history of remnants of a fragmented Grenville belt. Em: Vaughan, A.P.M., Leat, P.T., Pankhurst, R.J. (Eds.). Terrane processes at the margins of Gondwana. Geological Society of London, Special Publications, (246): 329-346.

Corfu, F., Hanchar, J.M., Hoskin, P.W.O., Kinny, P. 2003. Atlas of zircon textures. Em: Hanchar, J.M., Hoskin, P.W.O. (Eds.). Zircon. Reviews in Mineralogy and Geochemistry, (53): 469-500.

Cornell, D.H., Thomas, R.J., Bowring, S.A., Armstrong, R.A., Grantham, G.H. 1996. Protolith interpretation in metamorphic terranes: a back-arc environment with Besshi-type base metal potential for the Quha Formation, Natal Province, South Africa. Precambrian Research, (77): 243-271.

Correa, A.M., Martens, U., Restrepo, J.J., Ordóñez-Carmona, O., Pimentel, M.M. 2005. Subdivisión de las metamorfitas básicas de los alrededores de Medellín-Cordillera Central de Colombia. Rev. Acad. Colomb. Cienc., 29(112): 325-344.

Correa, A.M., Pimentel, M.M., Restrepo, J.J., Nilson, A., Ordóñez, O., Martens, U., Laux, J.E., Junges, S. 2006. U-Pb zircon ages and Nd-Sr isotopes of the Altavista Stock and the San Diego Gabbro: new insights on Cretaceous arc magmatism in the Colombian Andes. 4th South American Symposium on Isotope Geology, Montevideo-Uruguay. 3 p.

Corredor, F. 2003. Seismic strain rates and distributed continental deformation in the northern Andes and three-dimensional seismotectonics of northwestern South America. Tectonophysics, (372): 147-166.

Cortés, M., Angelier, J. 2005. Current states of stress in the northern Andes as indicated by focal mechanisms of earthquakes. Tectonophysics, (403): 29-58.

Cullers, R.L., Graf, J.L. 1984a. Rare earth elements in igneous rocks of the continental crust: intermediate and silicic rocks - ore petrogenesis. Em: Henderson, P. (Ed.). Rare earth element geochemistry. Developments in geochemistry, (2). Elsevier Science Pub. B.V. 510 p.

Cullers, R.L., Graf, J.L. 1984b. Rare earth elements in igneous rocks of the continental crust: predominantly basic and ultrabasic rocks. Em: Henderson, P. (Ed.). Rare earth element geochemistry. Developments in geochemistry, (2). Elsevier Science Pub. B.V. 510 p.

Dall'Agnol, R. 1992. Titanita-biotita granitos do baixo rio uaupés, Província Rio Negro, Amazonas. Parte II: geoquímica e petrogênese. Revista Brasileira de Geociências, 22(1): 15-28.

Dall'Agnol, R., Costi, H.T., da S. Leite, A.A., de Magalhães, M.S., Teixeira, N.P. 1999. Rapakivi granites from Brazil and adjacent areas. Precambrian Research, (95): 9–39.

Dall'Agnol, R., Macambira, M.J.B. 1992. Titanita-biotita granitos do baixo rio Uaupés, Província Rio Negro, Amazonas. Parte I: geologia, petrografia e geocronologia. Revista Brasileira de Geociências, 22(1): 3-14.

Debon, F., Le Fort, P. 1982. A chemical-mineralogical classification of common plutonic rocks and associations. Transactions of the Royal Society of Edinburgh, Earth Sciences, (73): 135-149.

De La Roche, H., Leterrier, J., Grandclaude, P., Marchal, M. 1980. A classification of volcanic and plutonic rocks using R_1R_2-diagram and major-element analyses-its relationships with current nomenclature. Chemical Geology, (29): 183-210.

DePaolo, D.J. 1981. A neodymium and strontium isotopic study of the Mesozoic calc-alkaline granitic batholiths of the Sierra Nevada and Peninsular Ranges, California. Journal of Geophysical Research, 86(B11): 10470-10488.

DePaolo, D.J. 1988. Neodymium isotope geochemistry: an introduction. Springer-Verlag. 187 p.

Dickin, A.P. 2005. Radiogenic isotope geology. 2nd edition. Cambridge University Press. 492 p.

Dörr, W., Grösser, J.R., Rodríguez, G.I., Kramm, U. 1995. Zircon U-Pb age of the Paramo Rico tonalite-granodiorite, Santander Massif (Cordillera Oriental, Colombia) and its geotectonic significance. Journal of South American Earth Sciences, 8(2): 187-194.

Eby, G.N. 1990. The A-type granitoids: a review of their occurrence and chemical characteristics and speculations on their petrogenesis. Lithos, (26): 115-134.

Eby, G.N. 1992. Chemical subdivision of the A-type granitoids: petrogenetic and tectonic implications. Geology, (20): 641-644.

Echeverría, L.M. 1980. Tertiary or Mesozoic komatiites from Gorgona island, Colombia: field relations and geochemistry. Contributions to Mineralogy and Petrology, (73): 253– 266.

El Bouseily, A.M., El Sokkary, A.A. 1975. The relation between Rb, Ba and Sr in granitic rocks. Chemical Geology, (16): 207-219.

Evensen, N.M., Hamilton, P.J., O'Nions, R.K. 1978. Rare-earth abundances in chondritic meteorites. Geochimica et Cosmochimica Acta, (42): 1199-1212.

Feininger, T., Barrero, D., Rico, H., Castro, N., Hall, R.B. 1973. Geology and mineral deposits of an area in the departments of Antioquia and Caldas (Subzone IIB), Colombia. USGS, Project Report (IR) CO-24. 223 p.

Forero, A. 1970. Estratigrafía del precretácico en el flanco occidental de la Serranía de Perijá. Geología Colombiana, (7): 7–18.

Frost, B.R., Barnes, C.G., Collins, W.J., Arculus, R.J., Ellis, D.J., Frost, C.D. 2001. A geochemical classification for granitic rocks. Journal of Petrology, 42(11): 2033-2048.

Frost, B.R., Frost, C.D. 2008. A geochemical classification for feldspathic igneous rocks. Journal of Petrology, 49(11): 1955-1969.

Fuck, R.A., Brito-Neves, B.B., Schobbenhaus, C. 2008. Rodinia descendants in South America. Precambrian Research, (160): 108-126.

Gansser, A. 1950. Geological and petrological notes on Gorgona island in relation to north-west S America. Schweizerische Mineralogische und Petrographische Mitteilungen, (30): 219– 237.

Gansser, A. 1955. Ein beitrag zur geologie und petrographie der Sierra Nevada de Santa Marta (Kolumbien, Südamerika). Schweizer Mineralogische und Petrographische Mitteilungen, 35(2): 209-279.

Gansser, A. 1973. Facts and theories on the Andes. Journal of the Geological Society of London, (129): 93-131.

Galvis, J., De La Espriella, R. 1992. Vulcanismo Terciario al sur de la isla de Mompox (parte nororiental de la Serranía de San Lucas). Rev. Acad. Colomb. Cienc. 18(70): 359-368.

Garrels, R.M., Mackenzie, F.T. 1971. Evolution of sedimentary rocks. W.W. Norton & Company Inc., New York. 397 p.

Gaudette. H.E., Mendoza, V., Hurley, P.M., Fairbairn, H.W. 1978. Geology and age of the Parguaza rapakivi granite, Venezuela. GSA Bulletin, (89): 1335-1340.

Gioia, S.M.C.L., Pimentel, M.M. 2000. The Sm-Nd Isotopic Method in the Geochronology Laboratory of the University of Brasília. Anais da Academia Brasileira de Ciências, 72(2): 219-245.

Göbel, V., Stibane, F. 1979. Edad K-Ar en hornblendas de plutones tonalíticos, Cordillera Occidental Colombia. U. Nal. Publ. Esp. Geol., (19): 1 – 2.

Goldsmith, R., Marvin, R.F., Mehnert, H.H. 1971. Radiometric ages in the Santander Massif, Eastern Cordillera, Colombian Andes. USGS-INGEOMINAS, Prof. Paper 750-D. p. D44-D49.

González, H. 2001. Mapa geológico del Departamento de Antioquia: geología, recursos minerales y amenazas potenciales. Memoria explicativa. INGEOMINAS. 240 p.

Grösser, J.R., Prössl, K.F. 1991. First evidence of the Silurian in Colombia: palynostratigraphic data from the Quetame Massif, Cordillera Oriental. Journal of South American Earth Sciences, 4(3): 231-238.

Hanchar, J.M., Miller, C.F. 1993. Zircon zonation patterns as revealed by cathodoluminescence and backscattered electron images: Implications for interpretation of complex crustal histories. Chemical Geology, (110): 1-13.

Harrison, J.V. 1929. The Magdalena Valley, Colombia, South America. 15th International Geological Congress, Vol. 2, Pretoria, South Africa. p. 399-409.

Healy, B., Collins, W.J., Richards, S.W. 2004. A hybrid origin for Lachlan S-type granites: the Murrumbidgee Batholith example. Lithos, (78): 197-216.

Hoskin, P.W.O., Black, L.P. 2000. Metamorphic zircon formation by solid-state recrystallization of protolith igneous zircon. Journal of Metamorphic Geology, (18): 423-439.

Huguett, A., Galvis, J., Ruge, P. 1979. Capítulo 2: geología. Em: La Amazonia colombiana y sus recursos. Proyecto radargramétrico del Amazonas, República de Colombia. p. 29-92.

Ibáñez-Mejía, M., Ruiz, J., Valencia, V.A., Cardona, A., Gehrels, G.E., Mora, A.R. 2011. The Putumayo Orogen of Amazonia and its implications for Rodinia reconstructions: New U–Pb geochronological insights into the Proterozoic tectonic evolution of northwestern South America. Precambrian Research, (191): 58– 77.

INGEOMINAS. 1977. Mapa fotogeológico de la Serranía de San Lucas. Escala 1:500.000.

INGEOMINAS. 1983. Mapa de terrenos geológicos de Colombia. Memoria. 139 p.

INGEOMINAS. 2005. Investigación integral del andén Pacífico Colombiano. Tomo I: Geología. 165 p.

INGEOMINAS. 2007. Mapa Geológico de Colombia. Escala 1:2'800.000. Segunda Edición.

INGEOMINAS-British Geological Survey. 1984. Geología de las planchas: 243-261-262-278-279-280-299 y 300, Departamento del Valle. República de Colombia. 85 p.

INGEOMINAS-Universidad Industrial de Santander. 2006. Cartografía geológica de 9.600 km2 de la Serranía de San Lucas: planchas 55 (El Banco), 64 (Barranco de Loba), 85 (Simití) y 96 (Bocas del Rosario): aporte al conocimiento de su evolución geológica. Memoria explicativa. Plancha 55 El Banco, sur del Departamento de Bolívar y Cesar. Bogotá, 176 p.

Irvine, T.N., Baragar, W.R.A. 1971. A guide to the chemical classification of the common volcanic rocks. Canadian Journal of Earth Sciences, (8): 523-548.

Jackson, S.E., Pearson, N.J., Griffin, W.L., Belousova, E.A. 2004. The application of laser ablation inductively coupled plasma mass spectrometry to in situ U-Pb zircon geochronology. Chemical Geology, (211): 47–69.

Jacobsen, S.B., Wasserburg, G.J. 1980. Sm-Nd isotopic evolution of chondrites. Earth and Planetary Science Letters, (50): 139-155.

Jacobsen, S.B., Wasserburg, G.J. 1984. Sm-Nd isotopic evolution of chondrites and achondrites, II. Earth and Planetary Science Letters, (67): 137-150.

Jaramillo, L., Escovar, R., Vesga, C.J. 1980. Edades K-Ar de rocas con alteración hidrotermal asociadas al sistema de pórfido de cobre y molibdeno de Mocoa, Intendencia del Putumayo, Colombia. Geología Norandina, (1): 11-18.

Jensen, L.S. 1976. A new cation plot for classifying subalkalic volcanic rocks. Ontario Division of Mines, Miscelaneous Paper, 66. 22 p.

Jiménez-Mejía, D.M., Juliani, C., Cordani, U.G. 2006. P–T–t conditions of high-grade metamorphic rocks of the Garzón Massif, Andean basement, SE Colombia. Journal of South American Earth Sciences, (21): 322–336.

Johansson, A. 2009. Baltica, Amazonia and the SAMBA connection—1000 million years of neighborhood during the Proterozoic?. Precambrian Research, (175): 221–234.

Jones, D.L., Howell, D.G., Coney, P.J., Monger, J.W.H. 1983. Recognition, character, and analysis of tectonostratigraphic terranes in western North America. Em: Hashimoto, M., Uyeda, S. (Eds.). Advances in Earth and Planetary Sciences. Terra Sci. Publ, Tokyo. p. 21-35.

Keppie, J.D., Dostal, J. 2007. Rift-related basalts in the 1.2-1.3 Ga granulites of the northern Oaxacan Complex, southern Mexico: evidence for a rifted arc on the northwestern margin of Amazonia. Proceedings of the Geologist Association, (118): 63–74.

Keppie, J.D., Ortega-Gutierrez, F. 2010. 1.3–0.9 Ga Oaxaquia (Mexico): remnant of an arc/backarc on the northern margin of Amazonia. Journal of South American Earth Sciences, 29(1): 21–27.

Kerr, A.C. 2005. La Isla de Gorgona, Colombia: A petrological enigma?. Lithos, (84): 77– 101.

Kerr, A.C., Marriner, G.F., Arndt, N.T., Tarney, J., Nívia, A., Saunders, A.D., Duncan, R.A. 1996. The petrogenesis of Gorgona komatiites, picrites and basalts: new field, petrographic and geochemical constraints. Lithos, (37): 245-260.

Kerr, A.C., Marriner, G.F., Tarney, J., Nívia, A., Saunders, A.D., Thirlwall, M.F., Sinton, W. 1997. Cretaceous Basaltic Terranes in Western Colombia: Elemental, Chronological and Sr–Nd Isotopic Constraints on Petrogenesis. Journal of Petrology, 38(6): 677-702.

Kroonenberg, S.B. 1982a. A Grenvillian granulite belt in the Colombian Andes and its relation to the Guiana Shield. Geologie en Mijnbouw, (61): 325-333.

Kroonenberg, S.B. 1982b. Litología, Metamorfismo y origen de las granulitas del Macizo de Garzón, Cordillera Oriental (Colombia). Geología Norandina, (6): 39-46.

Kuno, H. 1966. Lateral variation of basalt magma type across continental margins and island arcs. Bulletin of Volcanology, (29): 195-222.

Leal-Mejía, H., Shaw, R.P., Padilla, R., Valencia, V. 2010. Magmatism vs. mineralization in the Segovia-Remedios and Central Antioquia Au Districts, Colombia. Poster: SEG2010 Conference.

Le Maitre, R.W. (Ed.), Streckeisen, A., Zanettin, B., Le Bas, M.J., Bonin, B., Bateman, P., Bellieni, G., Dudek, A., Efremova, A., Keller, J., Lameyre, J., Sabine, P.A., Schmid, R., Sørensen, H., Woolley, A.R. 2002. Igneous rocks: a classification and glossary of terms. Recommendations of the IUGS Subcomission on the systematics of igneous rocks. Cambridge, University Press. 236 p.

Li, Z.X., Bogdanova, S.V., Collins, A.S., Davidson, A., De Waele, B., Ernst, R.E., Fitzsimons, I.C.W., Fuck, R.A., Gladkochub, D.P., Jacobs, J., Karlstrom, K.E., Lu, S., Natapov, L.M., Pease, V., Pisarevsky, S.A., Thrane, K., Vernikovsky, V. 2008. Assembly, configuration, and break-up history of Rodinia: a synthesis. Precambrian Research, (160): 179–210.

Lockwood, J.P. 1965. Geology of the Serranía de Jarara area, Guajira Peninsula, Colombia. PhD. Thesis, Princeton University. 237 p.

Londoño, C., Montoya, J.C., Ordóñez-Carmona, O., Restrepo, J.J. 2009. Características de las mineralizaciones vetiformes en el distrito minero Bagre-Nechí, Antioquia. Boletín ciencias de la tierra, (26): 29-38.

Ludwig, K.R. 2009. Isoplot. A Geochronological Toolkit for Microsoft Excel. Ver. 3.71.09.05.23nx. Berkeley Geochronology Center.

Lugmair, G.W., Marti, K. 1978. Lunar initial ^{143}Nd/^{144}Nd: Differential evolution of the lunar crust and mantle. Earth Planetary Science Letters, (39): 349-357.

MacDonald, W.D. 1965. Geology of the Serranía de Macuira area, Guajira Peninsula, Colombia. PhD. Thesis, Princeton University. 167 p.

MacDonald, W.D., Doolan, B.L., Cordani, U.G. 1971. Cretaceous-Early Tertiary Metamorphic K-Ar Age Values from the South Caribbean. GSA Bulletin, (82): 1381-1388.

MacKenzie, W.S., Donaldson, C.H., Guilford, C.G. 1982. Atlas of igneous rocks and their textures. Wiley. 148 p.

Maniar, P.D., Piccoli, P.M. 1989. Tectonic discrimination of granitoids. GSA Bulletin, (101): 635-643.

McCourt, W.J., Aspden, J.A., Brook, M. 1984. New geological and geochronological data from the Colombian Andes: continental growth by multiple accretion. J. geol. Soc. London, (141): 831-845.

Mesz, L. 2008. Caracterização tectono-magmática do norte da Cordilheira Central da Colômbia, Batólito de Norosí, Região de San Lucas. Monografía de trabalho de formatura (TF/2008/32). Universidade de São Paulo, Brasil. 62 p.

Mojica, J., Villaroel, C., Macia, C. 1988. Nuevos afloramientos fosilíferos del Ordovícico Medio (Fm. El Hígado) al oeste de Tarqui, valle superior del Magdalena (Huila, Colombia). Geología Colombiana, (16): 95–97.

Montes, C., Guzmán, G., Bayona, G., Cardona, A., Valencia, V., Jaramillo, C. 2010. Clockwise rotation of the Santa Marta massif and simultaneous Paleogene to Neogene deformation of the Plato-San Jorge and Cesar-Ranchería basins. Journal of South American Earth Sciences, (29): 832–848.

Moreno-Sánchez, M., Pardo-Trujillo, A. 2002. Historia geológica del occidente colombiano. Geo. Eco. Trop. 26(2): 91-113.

Naslund, H.R., McBirney, A.R. 1996. Mechanisms of formation of igneous layering. Em: Cawthorn, R.G. (Ed.). Layered intrusions. Developments in Petrology. Elsevier Science B.V. (15): 1-43.

Nebel, O., Scherer, E.E., Mezger, K. Evaluation of the ^{87}Rb decay constant by age comparison against the U–Pb system. Earth and Planetary Science Letters, (301): 1–8.

Nesse, W.D. 1991. Introduction to optical mineralogy. 2nd edition. Oxford University Press. 335 p.

Nívia, A., Marriner, G.F., Kerr, A.C., Tarney, J. 2006. The Quebradagrande Complex: A Lower Cretaceous ensialic marginal basin in the Central Cordillera of the Colombian Andes. Journal of South American Earth Sciences, (21): 423–436.

Ordóñez-Carmona, O., Frantz, J.C., Chemale, F., Londoño, C. 2009. Serranía de San Lucas: mineralizaciones auríferas, intrusiones de 1500 Ma, metamorfismo

Grenville y magmatismo Jurásico. XII Congreso Colombiano de Geología. Paipa-Colombia. Memorias. 1 p.

Ordóñez-Carmona, O., Pimentel, M.M. 2002a. Rb-Sr and Sm-Nd isotopic study of the Puquí Complex, Colombian Andes. Journal of South American Earth Sciences, (15): 173-182.

Ordóñez-Carmona, O., Pimentel, M.M., De Moraes, R. 2002b. Granulitas de Los Mangos, un fragmento Grenvilliano en la parte oriental de la Sierra Nevada de Santa Marta. Rev. Acad. Colomb. Cienc., 26(99): 169-179.

Ordóñez-Carmona, O., Pimentel, M.M., De Moraes, R., Restrepo, J.J. 1999. Rocas Grenvillianas en la región de Puerto Berrío - Antioquia. Rev. Acad. Colomb. Cienc., 23(87): 225-232.

Ordóñez-Carmona, O., Pimentel, M.M., Laux, J.H. 2008a. Edades U-Pb del Batolito Antioqueño. Boletín Ciencias de la Tierra, (22): 129-130.

Ordóñez-Carmona, O., Restrepo, J.J., Cuadros, F.A., Minota, J.A., Londoño, C., Álvarez, M.J. 2008b. Rocas metamórficas de alto grado en la Serranía de San Lucas. Boletín ciencias de la tierra, (22): 131-132.

Ordóñez-Carmona, O., Restrepo, J.J., De Brito, R.S.C., Martens, U., Rodrigues, J.B. 2011. The Late Paleocene age of the Santa Bárbara Batholith (Valle, Colombia) and its implications on the evolution of the Arquía Complex. XIV Congresso Latinoamericano de Geologia, Medellín-Colombia. p. 109.

Ordóñez-Carmona, O., Restrepo, J.J., Pimentel, M.M. 2006. Geochronological and isotopical review of pre-Devonian crustal basement of the Colombian Andes. Journal of South American Earth Sciences, (21): 372-382.

Ordóñez-Carmona, O., Valencia, M., Abad, A.M. 2008c. Ambiente estructural de los depósitos auríferos de la Serranía de San Lucas (Bolívar, Colombia). Boletín ciencias de la tierra, (22): 127-128.

Passchier, C.W., Myers, J.S., Kröner, A. 1990. Field geology of high-grade gneiss terrains. Springer-Verlag. 150 p.

Payolla, B.L., Bettencourt, J.S., Kozuch, M., Leite, W.B., Fetter, A.H., Van Schmus, W.R. 2002. Geological evolution of the basement rocks in the east-central part of the Rondônia Tin Province, SW Amazonian Craton, Brazil: U-Pb and Sm-Nd isotopic constraints. Precambrian Research, (119): 141-169.

Pearce, J.A. 1982. Trace element characteristics of lavas from destructive plate boundaries. Em: Thorpe, R.S. Andesites. John Wiley & Sons. p. 525-548.

Pearce, J.A. 1996. Sources and settings of granitic rocks. Episodes, 19(4): 120-125.

Pearce, J.A., Harris, N.B.W., Tindle, A.G. 1984. Trace element discrimination diagrams for the tectonic interpretation of granitic rocks. Journal of Petrology, 25(4): 956-983.

Peccerillo, R., Taylor, S.R. 1976. Geochemistry of Eocene calc-alkaline volcanic rocks from the Kastamonu area, Northern Turkey. Contributions to Mineralogy and Petrology, (58): 63-81.

Philpotts, A.R. 1989. Petrography of igneous and metamorphic rocks. Pearson Education Inc. 179 p.

Pinson Jr., W.H., Hurley, P.M., Mencher, E., Fairbairn, H.W. 1962. K-Ar and Rb-Sr ages of biotites from Colombia, South America. Short Note. GSA Bulletin, (73): 907-910.

Priem, H.N.A., Andriessen, P.A.M., Boelrijk, N.A.I.M., De Boorder, H., Hebeda, E.H., Huguett, A., Verdurmen, E.A.T., Verschure, R.H. 1982. Geochronology of the Precambrian in the Amazonas region of southeastern Colombia (Western Guiana Shield). Geologie en Mijnbouw, (61): 229-242.

Priem, H.N.A., Kroonenberg, S.B., Boelrijk, N.A.I.M., Hebeda, E.H. 1989. Rb-Sr and K-Ar evidence for the presence of a 1.6 Ga basement underlying the 1.2 Ga Garzón-Santa Marta Granulite Belt in the Colombian Andes. Precambrian Research, (42): 315-324.

Ramos, V.A. 2009. Anatomy and global context of the Andes: Main geologic features and the Andean orogenic cycle. Em: Kay, S.M., Ramos, V.A., Dickinson, W.R. (Eds.). Backbone of the Americas: Shallow Subduction, Plateau Uplift, and Ridge and Terrane Collision. Geological Society of America Memoir (204): 31–65.

Ramos, V.A. 2010. The Grenville-age basement of the Andes. Journal of South American Earth Sciences, (29): 77-91.

Renzoni, G. 1962. Apuntes acerca de la litología y tectónica de la zona este y sureste de Bogota. Boletín Geológico de Ingeominas, 10(1–3): 59–79.

Renzoni, G. 1968. Geologia del Macizo de Quetame. Geología Colombiana, (5): 75–127.

Restrepo, J.J. 2008a. Obducción y metamorfismo de ofiolitas Triásicas en el flanco occidental del Terreno Tahamí, Cordillera Central de Colombia. Boletín ciencias de la tierra, (22): 49-100.

Restrepo, J.J., Dunlap, W.J., Martens, U., Ordóñez-Carmona, O., Correa, A.M. 2008b. Ar-Ar ages of amphibolites from the Central Cordillera of Colombia and their implications for tectonostratigraphic terrane evolution in the northwestern Andes. 6th South American Symposium on Isotope Geology, Bariloche-Argentina. 8 p.

Restrepo, J.J., Ordóñez-Carmona, O., Armstrong, R., Pimentel, M.M. 2011. Triassic metamorphism in the northern part of the Tahamí Terrane of the Central cordillera of Colombia. Journal of South American Earth Sciences, (32): 497-507.

Restrepo, J.J., Toussaint, J.F. 1988. Terranes and continental accretion in the Colombian Andes. Episodes, Vol. 11, No. 3: 189-193.

Restrepo, J.J., Toussaint, J.F., González, H., Cordani, U.G., Kawashita, K., Linares, E., Parica, C. 1991. Precisiones geocronológicas sobre el occidente colombiano. Simposio sobre magmatismo andino y su marco tectónico, Manizales-Colombia. Memorias, Tomo I. 1-22.

Restrepo-Pace, P.A., Ruiz, J., Gehrels, G., Cosca, M. 1997. Geochronology and Nd isotopic data of Grenville-age rocks in the Colombian Andes: new constraints for Late Proterozoic-Early Paleozoic paleocontinental reconstructions of the Americas. Earth and Planetary Science Letters, (150): 427-441.

Rizzotto, G.J., Scandolara, J.E., Quadros, L.E.S.M. 1996. Aspectos gerais da associação mangerito-charnockito-granito (MCG) da porção oriental do Estado de Rondônia. 39no Cong. Bras. Geol. Salvador. Resumos expandidos, SBG, (1): 35-37.

Rollinson, H. 1993. Using geochemical data: evaluation, presentation, interpretation. Longman Scientific & Technical. 352 p.

Santos, J.O.S., Hartmann, L.A., Gaudette, H.E., Groves, D.I., Mcnaughton, N.J., Fletcher, I.R. 2000. A new understanding of the provinces of the Amazon Craton based on integration of field mapping and U-Pb and Sm-Nd geochronology. Gondwana Research, 3(4): 453-488.

Sawyer, E.W. 2008. Atlas of migmatites. The Canadian Mineralogist Special Publication, 9. 135 p.

Schermer, E.R., Howell, D.G., Jones, D.L. 1984. The origin of allochthonous terranes: perspectives on the growth and shaping of continents. Ann. Rev. Earth Planet. Sci., (12): 107-131.

Serrano, L., Ferrari, L., López, M., Petrone, C.M., Jaramillo, C. 2011. An integrative geologic, geochronologic and geochemical study of Gorgona Island, Colombia: Implications for the formation of the Caribbean Large Igneous Province. Earth and Planetary Science Letters (309): 324–336.

Sillitoe, R.H., Jaramillo, L., Damon, P.E., Shafiqullah, M., Escovar, R. 1982. Setting, Characteristics and Age of the Andean Porphyry Copper Belt in Colombia. Economic geology, (77): 1837-1850.

Sinton, C.W., Duncan, R.A., Storey, M., Lewis, J., Estrada, J.J. 1998. An oceanic flood basalt province within the Caribbean plate. Earth and Planetary Science Letters, (155): 221–235.

Skridlaite, G., Wiszniewska, J., Duchesne, J.C. 2003. Ferro-potassic A-type granites and related rocks in NE Poland and S Lithuania: west of the East European Craton. Precambrian Research, (124): 305–326.

Spry, A. 1969. Metamorphic textures. Pergamon Press Ltd. 350 p.

Steiger, R.H., Jäger, E. 1977. Subcomission on geochronology: convention on the use of decay constants in geo- and cosmochronology. Earth and Planetary Science Letters, (36): 359-362.

Stibane, F.R. 1969. Zur geologie von Kolumbien, Sud Amerika das Quetame und Garzón massiv. Geotecktonische Forschungen, 30(1–2): 1–85.

Sun, S.S., McDonough, W.F. 1989. Chemical and isotopic systematics of oceanic basalts: implications for mantle composition and processes. Em: Saunders, A.D., Norry, M.J. (Eds.). Magmatism in the ocean basins. Geological Society Special Publication, (42): 313-345.

Tassinari, C.C.G., Macambira, M.J.B. 1999. Geochronological provinces of the Amazonian Craton. Episodes, 22(3): 174-182.

Tassinari, C.C.G., Siga, O., Jr., Teixeira, W. 1984. Épocas metalogenéticas relacionadas a granitogênese do Craton Amazônico. 33th Cong. Bras. Geol., Rio de Janeiro. Anais, SBG, (6): 2963-2977.

Toussaint, J.F., Restrepo, J.J. 1994. The Colombian Andes during Cretaceous times. Em: Salfity, J.A. (Ed.). Cretaceous Tectonics of the Andes. Vieweg & Sohn, Wiesbaden. p. 61–100.

Toussaint, J.F., Restrepo, J.J. 1996. Mesozoic and Cenozoic accretionary events in the Colombian Andes. 3rd International Symposium of the Andean Geodynamics. Saint Malo, França. p 513-515.

Trumpy, D. 1943. Pre-Cretaceous of Colombia. GSA Bulletin, (54): 1281–1304.

Tschanz, C.M., Marvin, R.F., Cruz, J., Mehnert, H.H., Cebula, G.T. 1974. Geologic evolution of the Sierra Nevada de Santa Marta, northeastern Colombia. GSA Bulletin, (85): 273-284.

Ujueta, G. 2004. Falla La Gloria, una importante falla normal en la parte más septentrional de la Serranía de San Lucas y el Valle Medio del Magdalena y geología del área. Geología Colombiana, (29): 88-105.

Vesga, C.J., Barrero, D. 1978. Edades K-Ar en rocas ígneas y metamórficas de la Cordillera Central de Colombia y su implicación geológica. II Congreso Colombiano de Geología, Bogotá. Resúmenes. 19 p.

Villagómez, D., Spikings, R., Magna, T., Kammer, A., Winkler, W., Beltrán, A. 2011. Geochronology, geochemistry and tectonic evolution of the Western and Central cordilleras of Colombia. Lithos, (125): 875–896.

Vinasco, C.J., Cordani, U,G., González, H., Weber, M., Peláez, C. 2006. Geochronological, isotopic, and geochemical data from Permo-Triassic granitic gneisses and granitoids of the Colombian Central Andes. Journal of South American Earth Sciences, (21): 355–371.

Wager, L.R., Brown, G.M. 1967. Layered igneous rocks. W. H. Freeman & Company. 588 p.

Ward, D.E., Goldsmith, R., Cruz, J., Restrepo, H. 1973. Geología de los cuadrángulos H-12 Bucaramanga y H-13 Pamplona, Departamento de Santander. INGEOMINAS. Boletín Geológico, 21(1-3). 132 p.

Weber, M.B.I., Cardona, A., Paniagua, F., Cordani, U., Sepúlveda, L., Wilson, R. 2009. The Cabo de la Vela Mafic Ultramafic Complex, Northeastern Colombian Caribbean region: a record of multistage evolution of a Late Cretaceous intra-oceanic arc. Em: James, K.H., Lorente, M.A., Pindell, J.L. (Eds.). The Origin and Evolution of the Caribbean Plate. Geological Society of London, Special Publications, (328): 549–568.

Weber, M.B.I., Cardona, A., Valencia, V., García-Casco, A., Tobón, M., Zapata, S. 2010. U/Pb detrital zircon provenance from late cretaceous metamorphic units of the Guajira Peninsula, Colombia: Tectonic implications on the collision between the Caribbean arc and the South American margin. Journal of South American Earth Sciences (29): 805–816.

Whalen, J.B., Currie, K.L., Chappell, B.W. 1987. A-type granites: geochemical characteristics, discrimination and petrogenesis. Contributions to mineralogy and petrology, (95): 407-419.

Wilson, M. 1989. Igneous petrogenesis. Springer. 466 p.

Winter, J.D. 2001. An introduction to igneous and metamorphic petrology. Prentice-Hall Inc. 697 p.

Yang, J.H., Wu, F.Y., Chung, S.L., Wilde, S.A., Chu, M.F. 2006. A hybrid origin for the Qianshan A-type granite, northeast China: geochemical and Sr–Nd–Hf isotopic evidence. Lithos, (89): 89-106.

Yardley, B.W.D., MacKenzie, W.S., Guilford, C. 1990. Atlas of metamorphic rocks and their textures. Prentice-Hall Inc. 128 p.

Zarifi, Z., Havskov, J., Hanyga, A. 2007. An insight into the Bucaramanga nest. Tectonophysics, (443): 93-105.

ANEXO I

Fotografias de CL e BSE de zircão

CL

028-01 (granodiorito). Os valores indicados correspondem a idades $^{206}Pb/^{238}U$ nos pontos analisados.

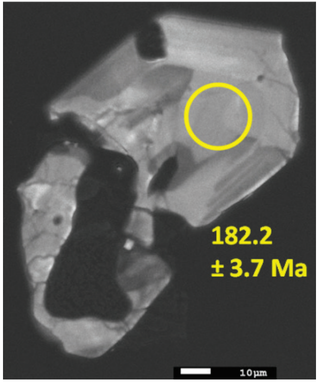

Z14

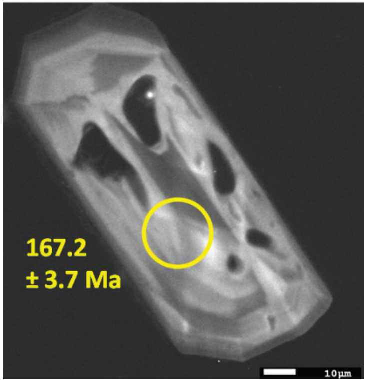

Z16

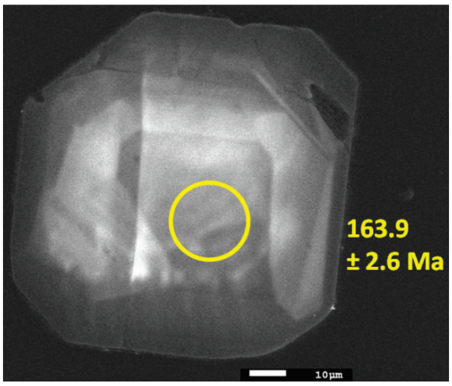

Z19

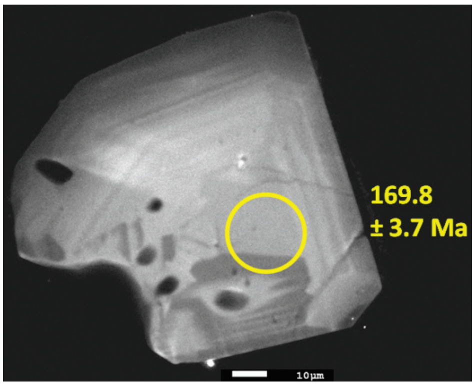

Z21

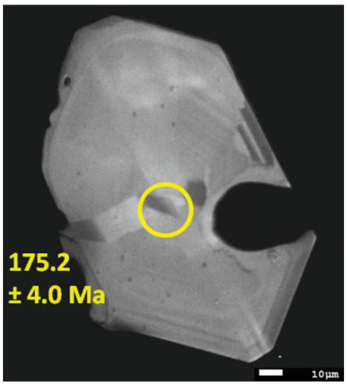

Z26

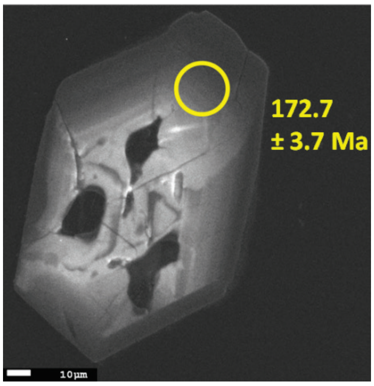

Z27

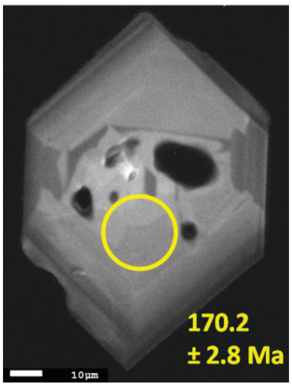

Z28

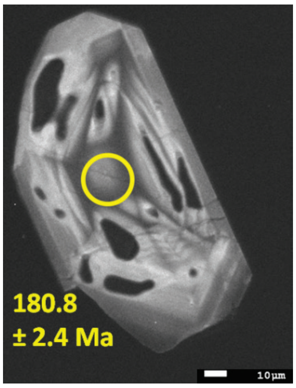

Z30

CL

028-01 (granodiorito). Os valores indicados correspondem a idades $^{206}Pb/^{238}U$ nos pontos analisados.

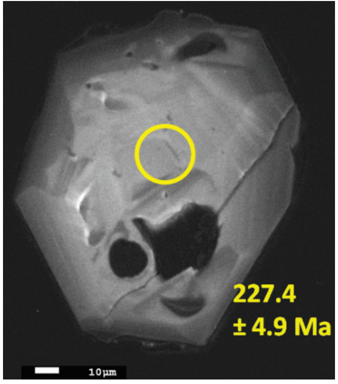

Z31

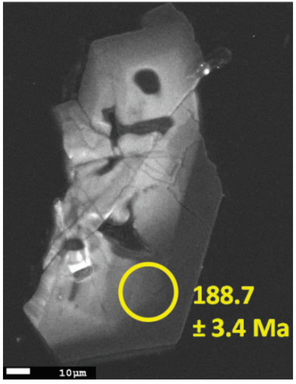

Z32

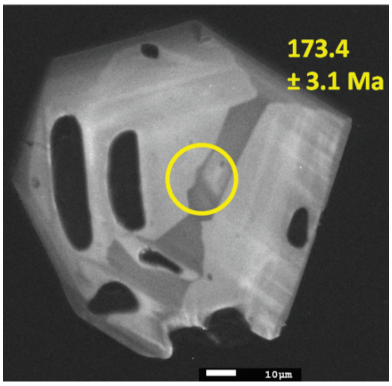

Z33

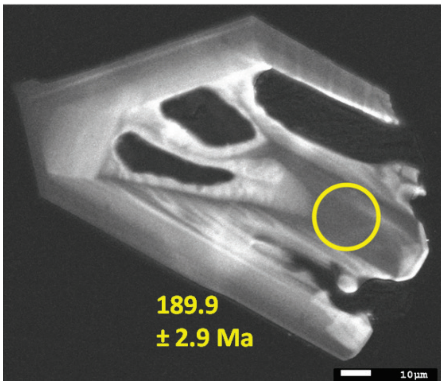

Z35

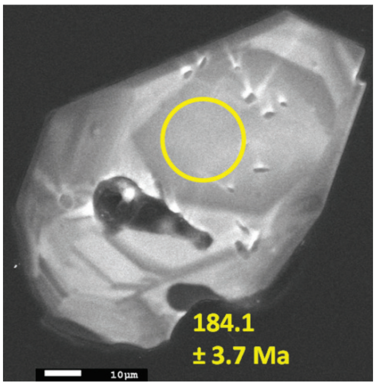

Z36

Z39

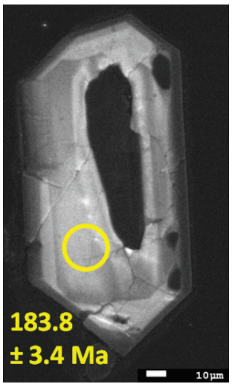

Z41

Z43

CL

028-01 (granodiorito). Os valores indicados correspondem a idades ^{206}Pb/^{238}U nos pontos analisados.

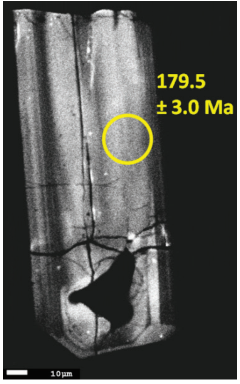

Z47

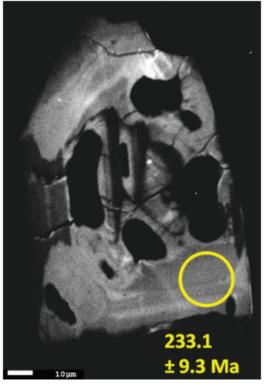

Z50

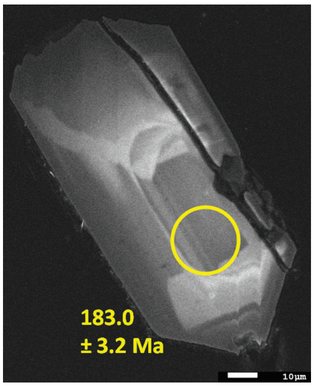

Z52

Z53

CL

030-01 (granodiorito). Os valores indicados correspondem a idades ^{206}Pb/^{238}U nos pontos analisados.

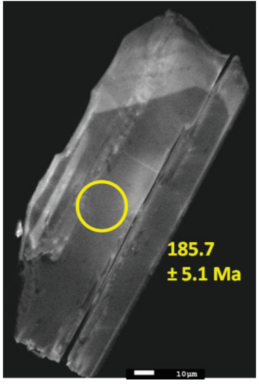

Z6

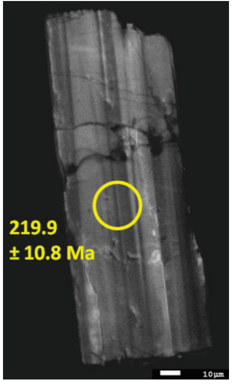

Z7

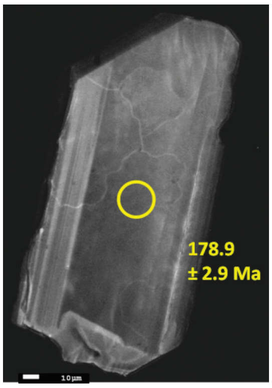

Z9

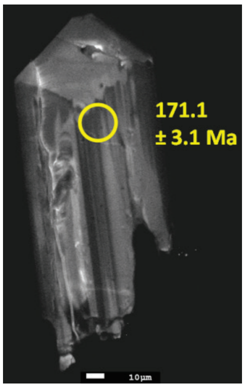

Z10

CL

030-01 (granodiorito). Os valores indicados correspondem a idades $^{206}Pb/^{238}U$ nos pontos analisados.

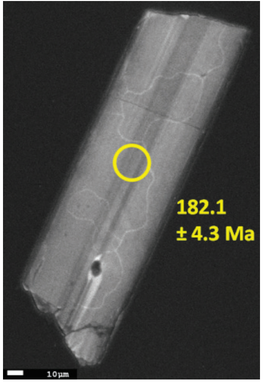

Z11

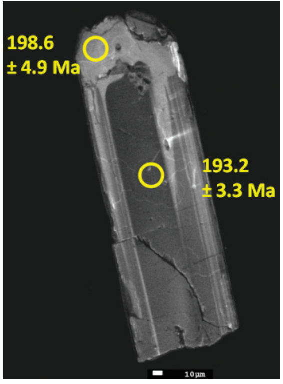

Z12

Z13

Z15

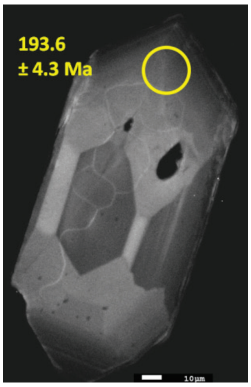

Z16

Z17

Z18

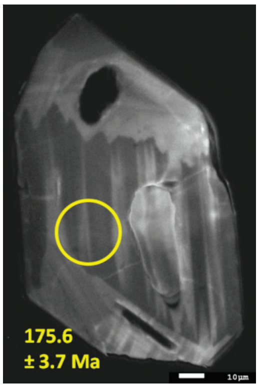

Z19

CL

030-01 (granodiorito). Os valores indicados correspondem a idades $^{206}Pb/^{238}U$ nos pontos analisados.

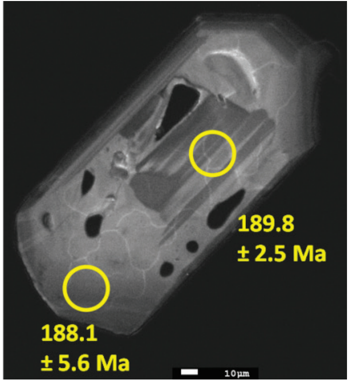

Z21

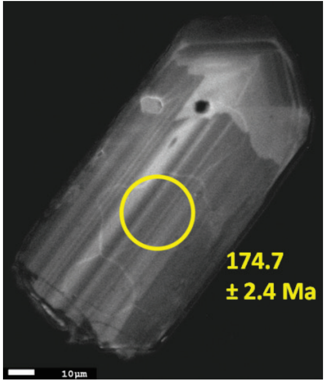

Z22

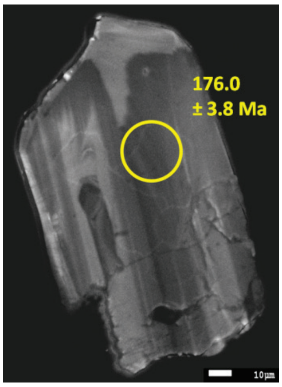

Z25

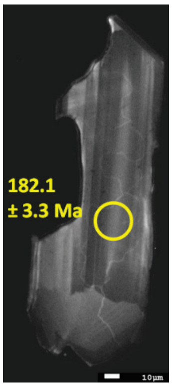

Z26

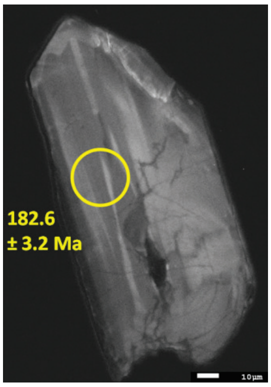

Z27

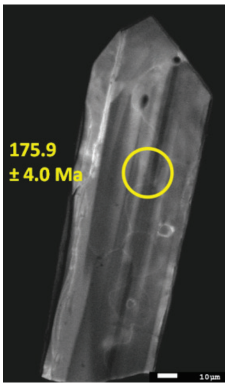

Z28

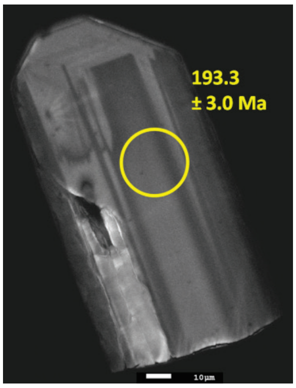

Z29

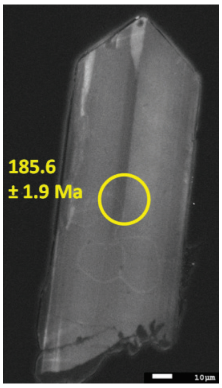

Z30

CL

030-01 (granodiorito). Os valores indicados correspondem a idades $^{206}Pb/^{238}U$ nos pontos analisados.

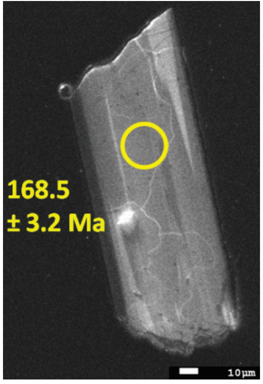

Z31

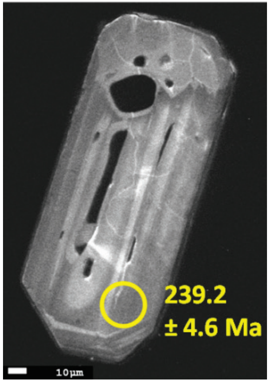

Z32

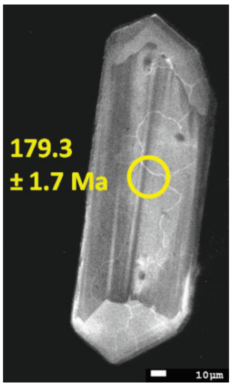

Z33

CL

017-05 (granito gnaisse). Os valores indicados correspondem a idades $^{207}Pb/^{206}Pb$ nos pontos analisados.

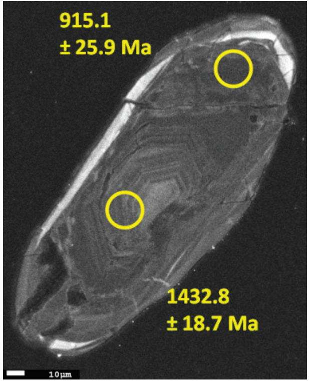

Z2

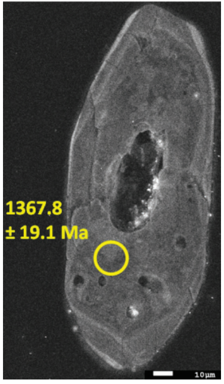

Z3

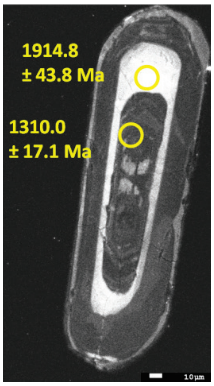

Z4

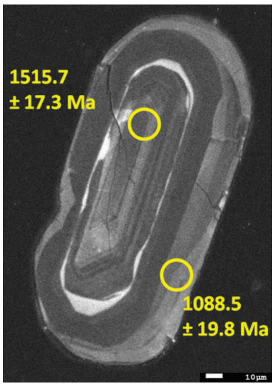

Z5

CL

017-05 (granito gnaisse). Os valores indicados correspondem a idades $^{207}Pb/^{206}Pb$ nos pontos analisados.

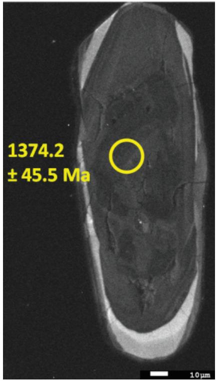

Z6

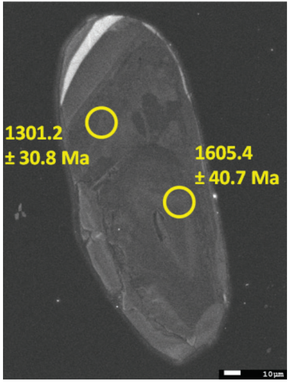

Z7

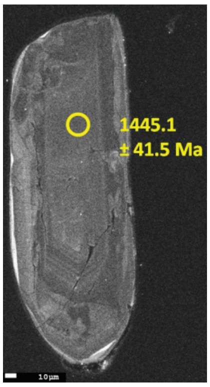

Z9

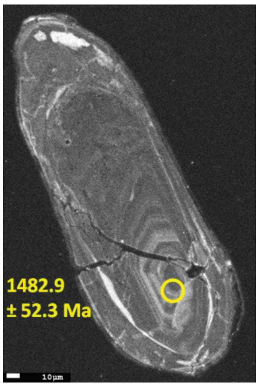

Z10

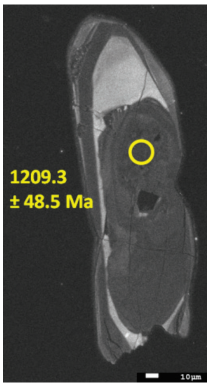

Z12

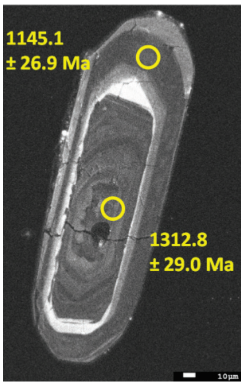

Z13

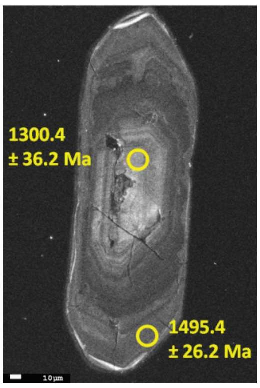

Z14

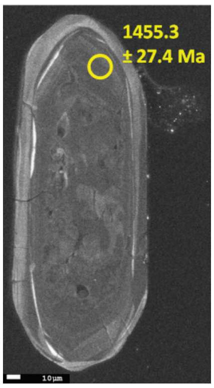

Z15

CL

017-05 (granito gnaisse). Os valores indicados correspondem a idades $^{207}Pb/^{206}Pb$ nos pontos analisados.

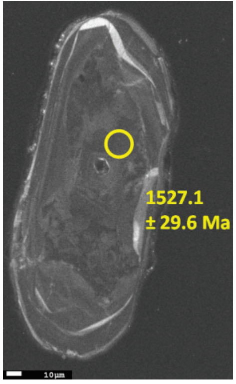

Z16

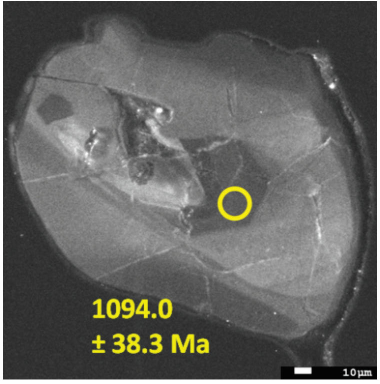

Z17

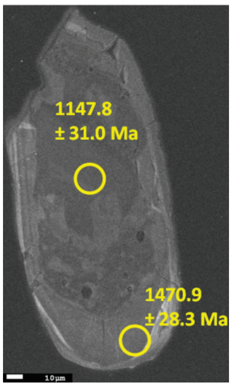

Z18

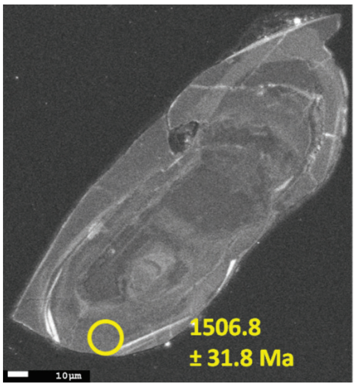

Z19

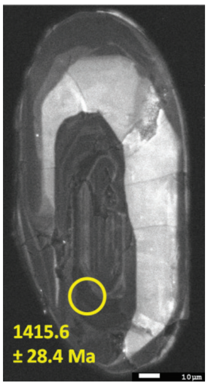

Z20

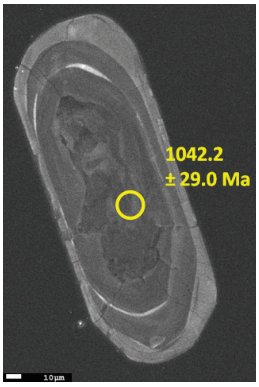

Z21

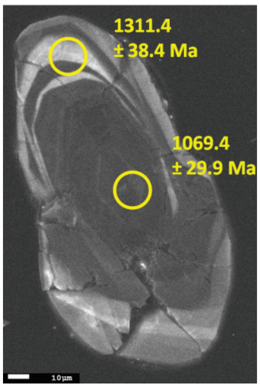

Z22

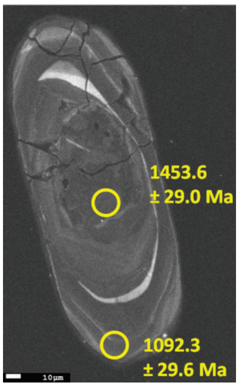

Z24

CL

017-05 (granito gnaisse). Os valores indicados correspondem a idades $^{207}Pb/^{206}Pb$ nos pontos analisados.

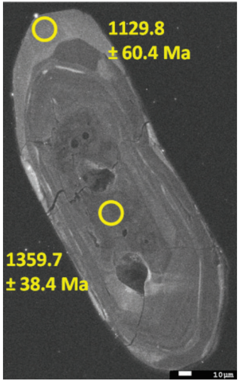

Z25

Z26

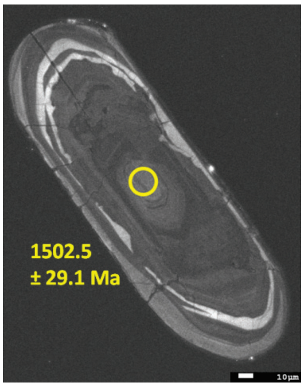

Z27

Z28

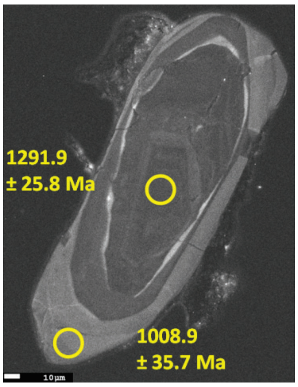

Z29

CL

022-01 (granito gnaisse). Os valores indicados correspondem a idades $^{207}Pb/^{206}Pb$ nos pontos analisados.

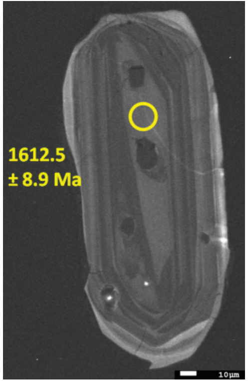

Z1

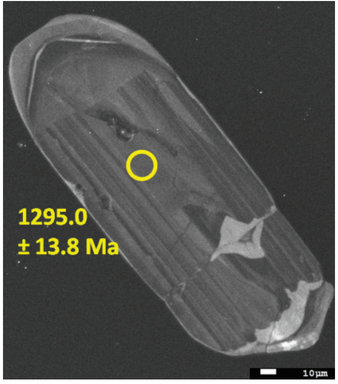

Z2

CL

022-01 (granito gnaisse). Os valores indicados correspondem a idades $^{207}Pb/^{206}Pb$ nos pontos analisados.

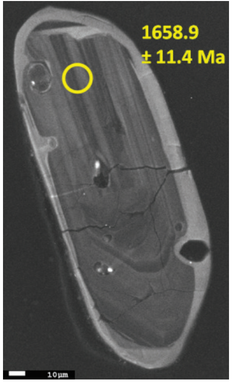

Z3

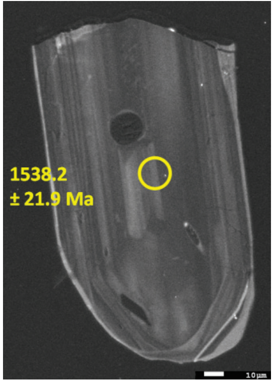

Z7

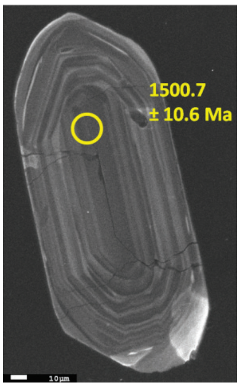

Z9

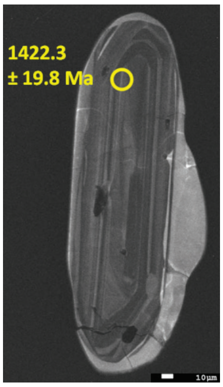

Z10

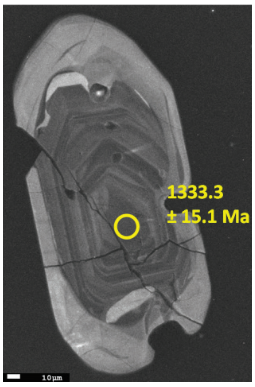

Z12

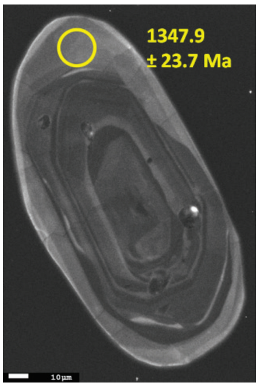

Z18

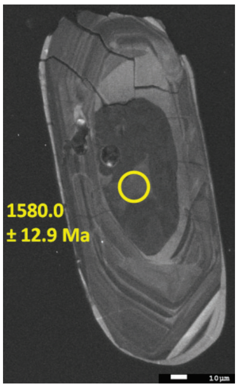

Z24

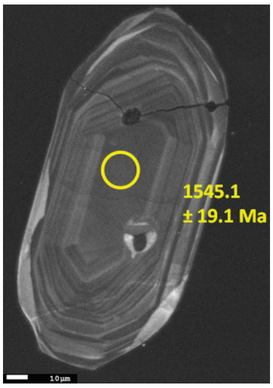

Z26

CL

022-01 (granito gnaisse). Os valores indicados correspondem a idades ^{207}Pb/^{206}Pb nos pontos analisados.

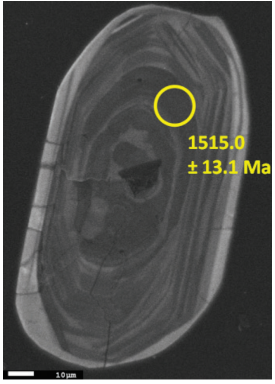

Z28

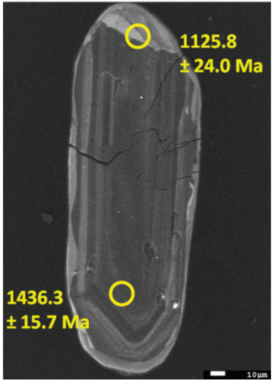

Z29

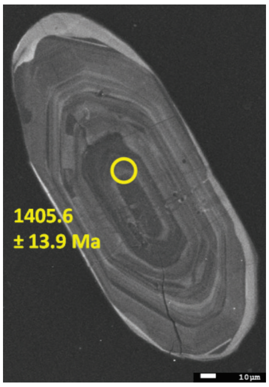

Z30

Z32

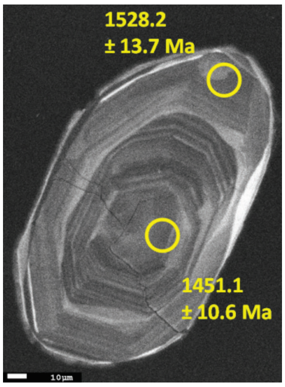

Z33

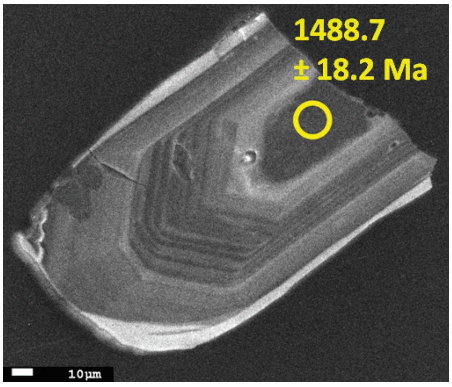

Z34

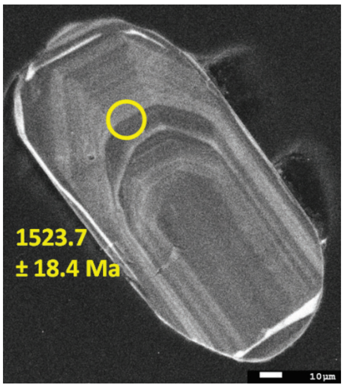

Z35

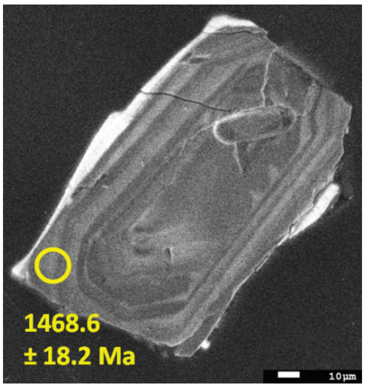

Z36

CL

022-01 (granito gnaisse). Os valores indicados correspondem a idades $^{207}Pb/^{206}Pb$ nos pontos analisados.

Z37

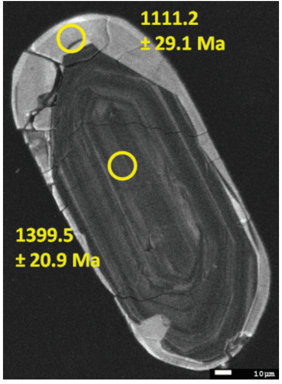

Z39

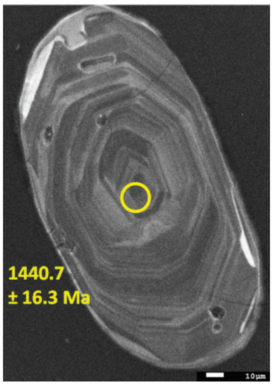

Z41

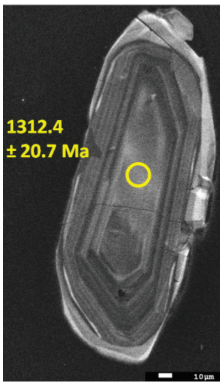

Z42

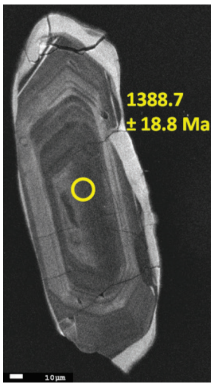

Z43

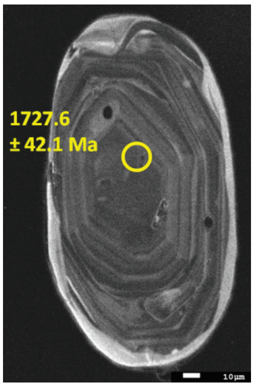

Z45

CL

PGG-18 (granitognaisse). Os valores indicados correspondem a idades $^{207}Pb/^{206}Pb$ nos pontos analisados.

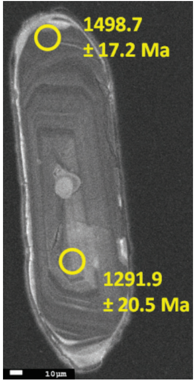

Z1

Z2

CL

PGG-18 (granitognaisse). Os valores indicados correspondem a idades $^{207}Pb/^{206}Pb$ nos pontos analisados.

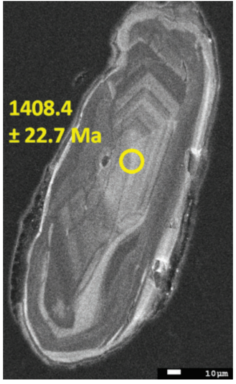

Z3

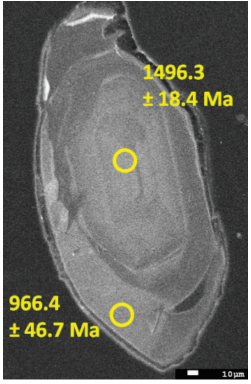

Z4

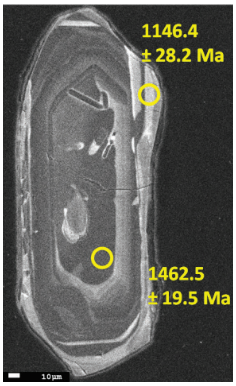

Z5

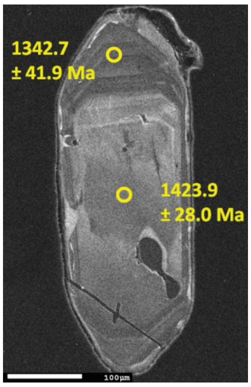

Z6

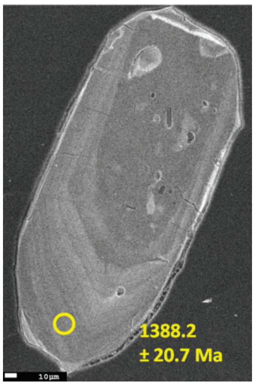

Z8

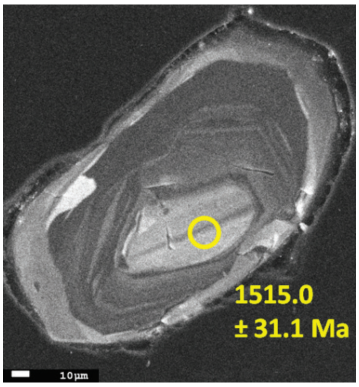

Z9

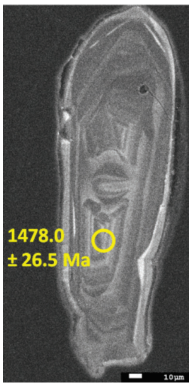

Z10

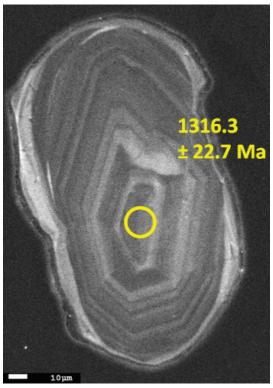

Z11

CL

PGG-18 (granitognaisse). Os valores indicados correspondem a idades $^{207}Pb/^{206}Pb$ nos pontos analisados.

Z12

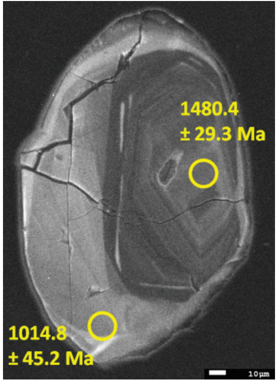

Z13

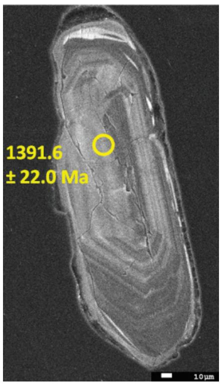

Z14

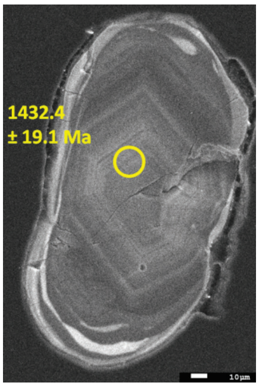

Z15

Z16

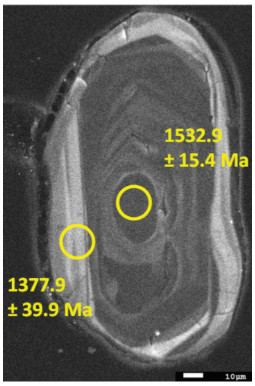

Z17

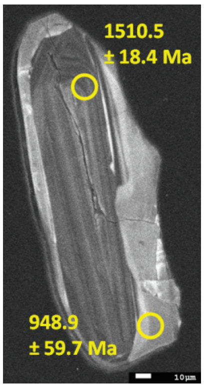

Z18

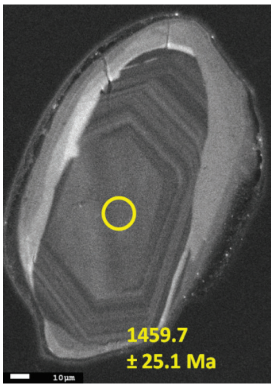

Z19

CL

PGG-18 (granitognaisse). Os valores indicados correspondem a idades $^{207}Pb/^{206}Pb$ nos pontos analisados.

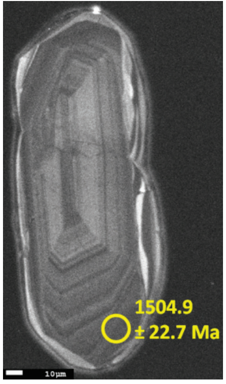

Z20

Z21

Z22

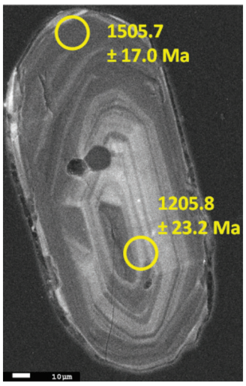

Z23

Z24

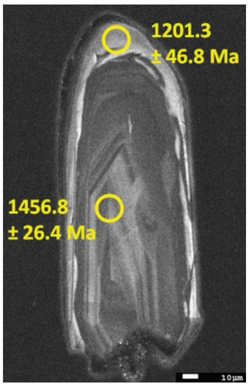

Z25

Z26

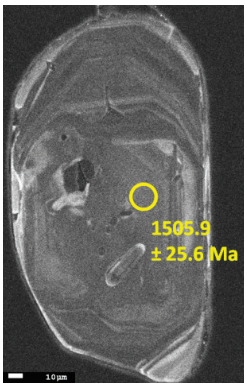

Z27

CL

PGG-18 (granitognaisse). Os valores indicados correspondem a idades $^{207}Pb/^{206}Pb$ nos pontos analisados.

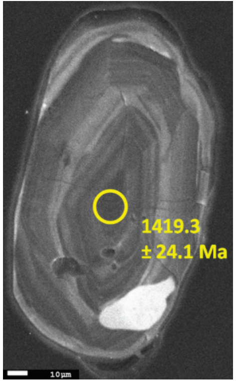

Z28

BSE

020-02 (metamonzogabro). Os valores indicados correspondem a idades $^{207}Pb/^{206}Pb$ nos pontos analisados.

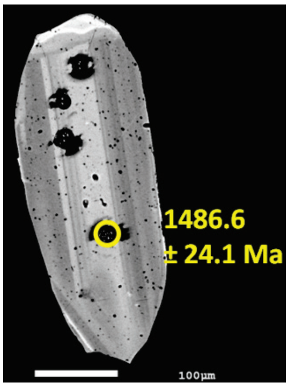

Z1

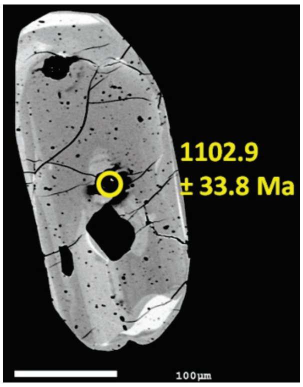

Z2

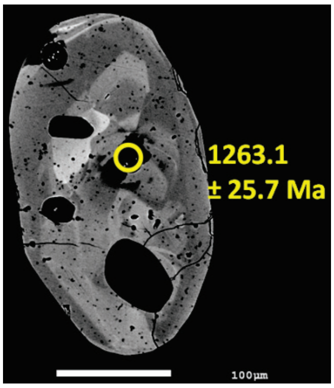

Z4

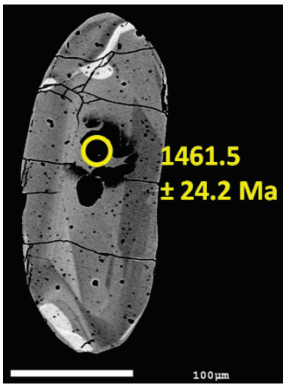

Z5

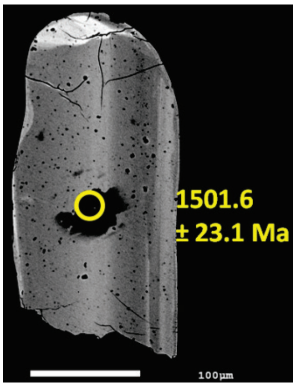

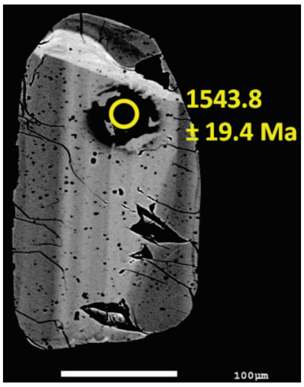

Z6 **Z8**

BSE

020-02 (metamonzogabro). Os valores indicados correspondem a idades $^{207}Pb/^{206}Pb$ nos pontos analisados.

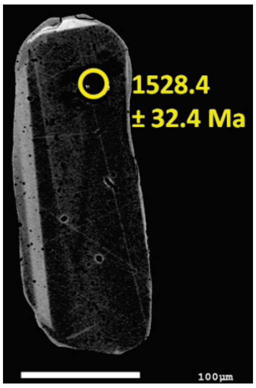

Z9 **Z10**

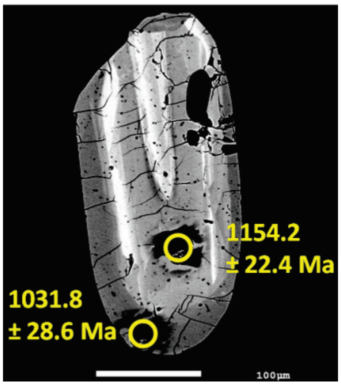

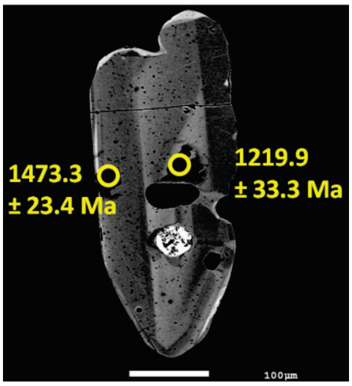

Z11 **Z12**

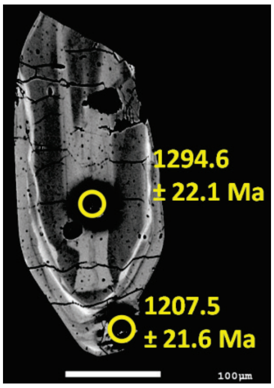

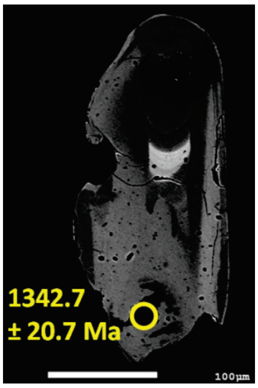

Z14 **Z15**

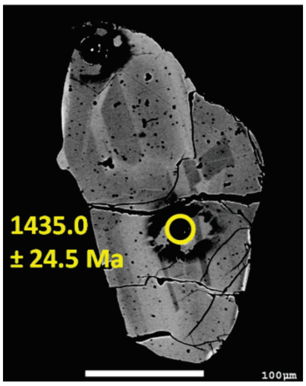

Z16 **Z17**

BSE

020-02 (metamonzogabro). Os valores indicados correspondem a idades $^{207}Pb/^{206}Pb$ nos pontos analisados.

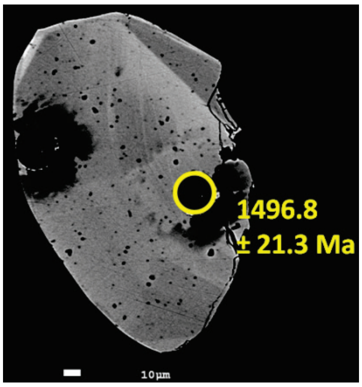

Z18

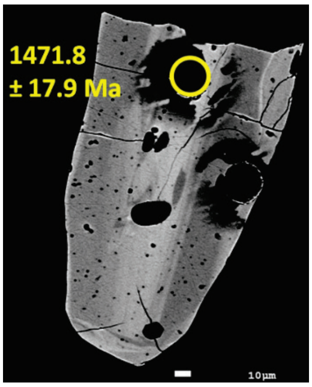

Z19

Z20

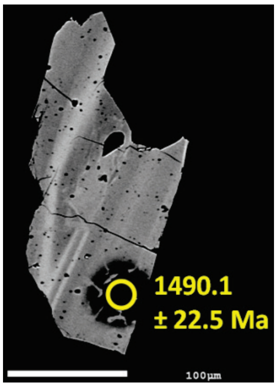

Z21

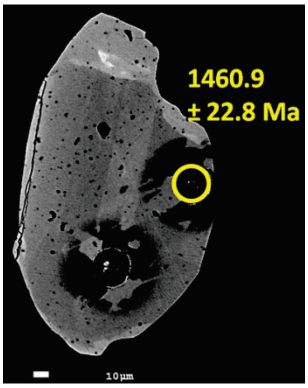

Z22

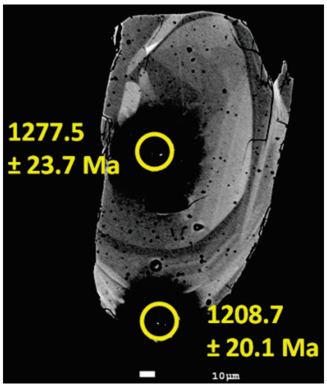

Z23

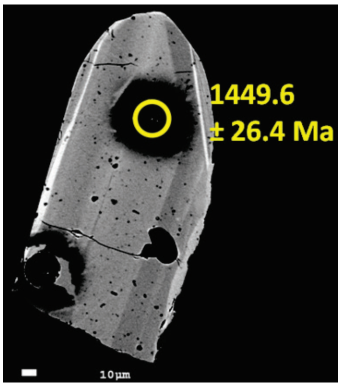

Z25

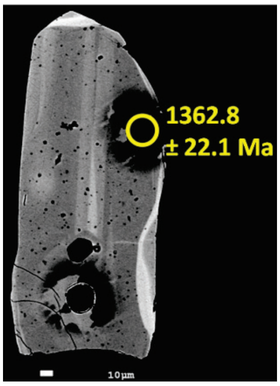

Z26

BSE

020-02 (metamonzogabro). Os valores indicados correspondem a idades $^{207}Pb/^{206}Pb$ nos pontos analisados.

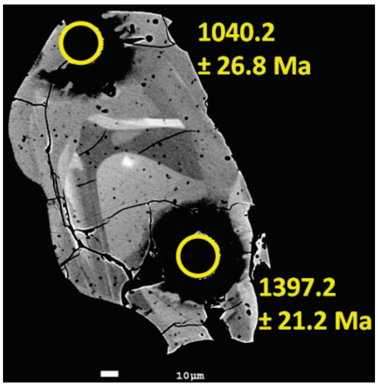

Z27

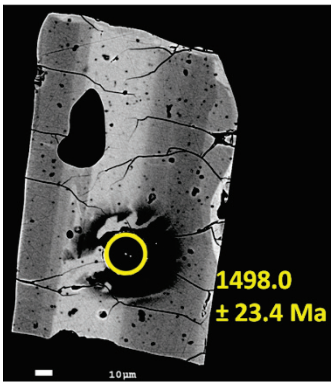

Z28

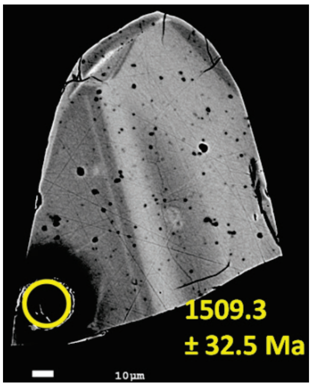

Z29

BSE

020-03 (metamonzogabro). Os valores indicados correspondem a idades $^{207}Pb/^{206}Pb$ nos pontos analisados.

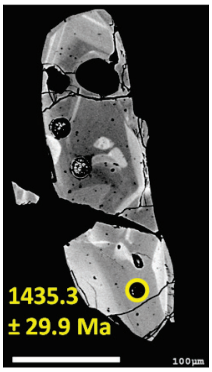

Z1

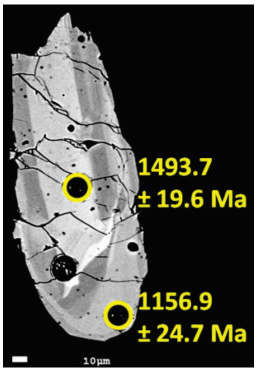

Z2

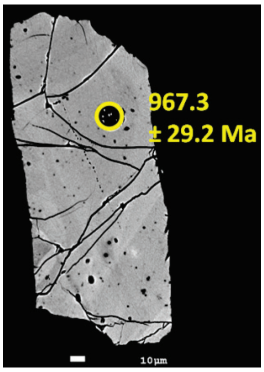

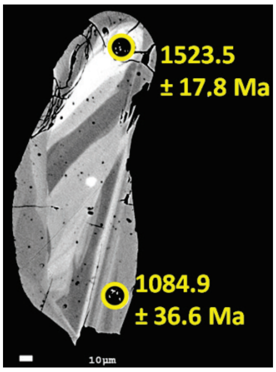

Z3 **Z4**

BSE

020-03 (metamonzogabro). Os valores indicados correspondem a idades $^{207}Pb/^{206}Pb$ nos pontos analisados.

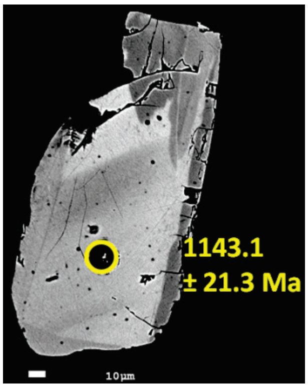

Z5 **Z6**

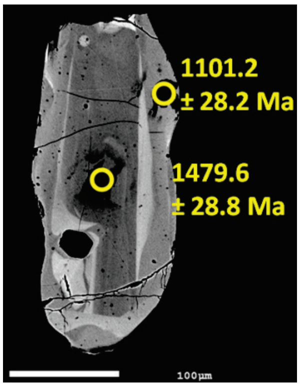

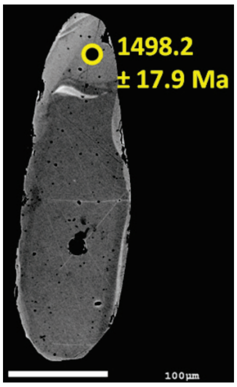

Z7 **Z8**

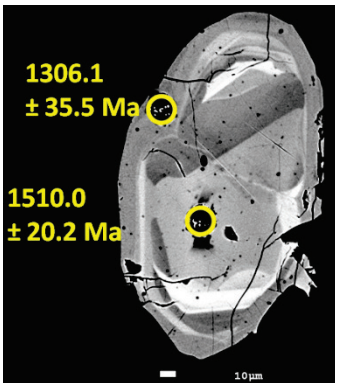

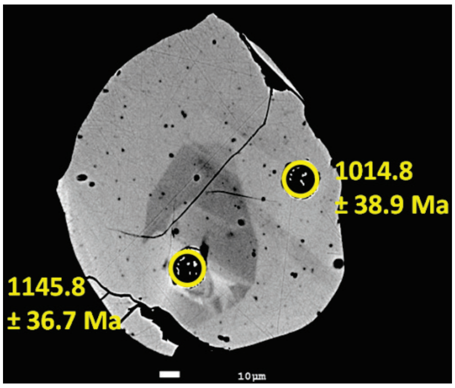

Z9 **Z10**

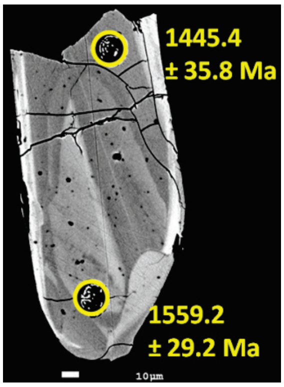

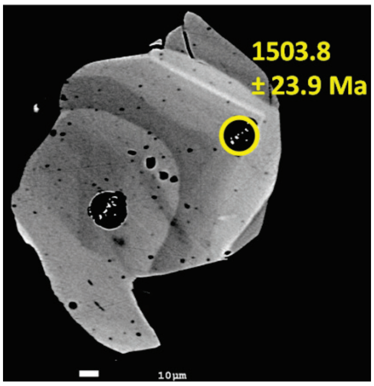

Z11 **Z12**

BSE

020-03 (metamonzogabro). Os valores indicados correspondem a idades $^{207}Pb/^{206}Pb$ nos pontos analisados.

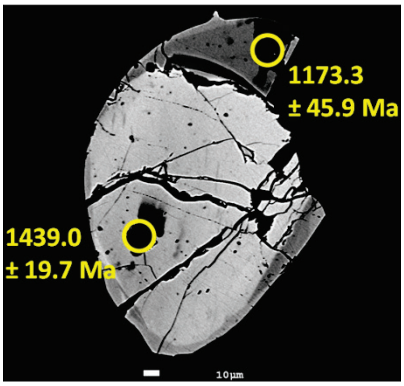

Z14

Z15

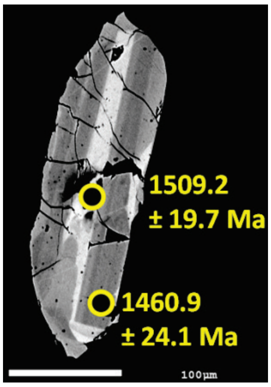

Z16

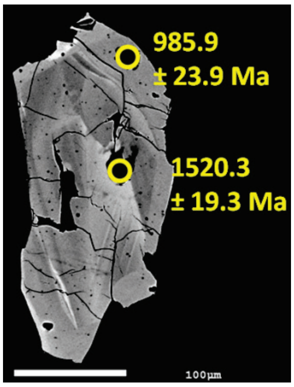

Z17

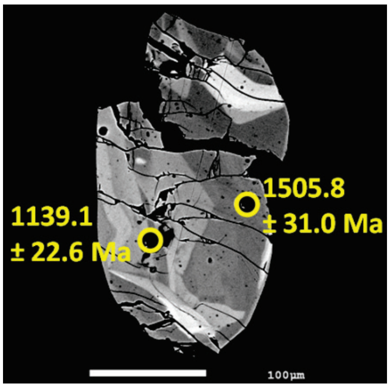

Z18

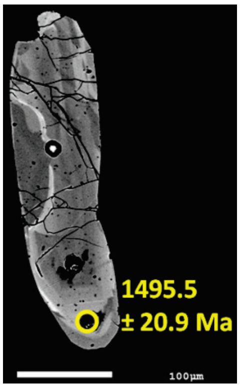

Z19

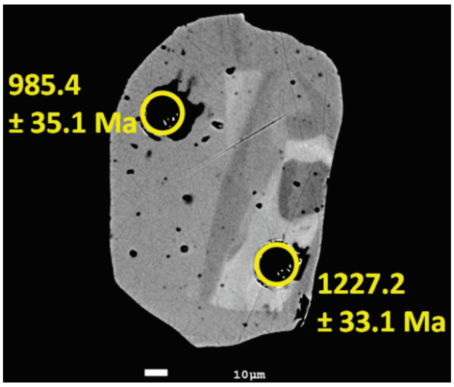

Z20

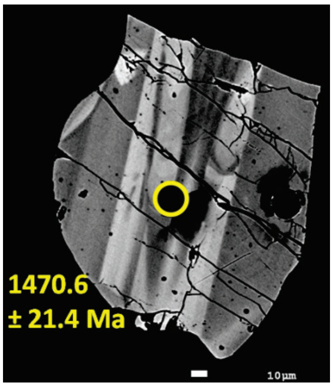

Z21

BSE

020-03 (metamonzogabro). Os valores indicados correspondem a idades $^{207}Pb/^{206}Pb$ nos pontos analisados.

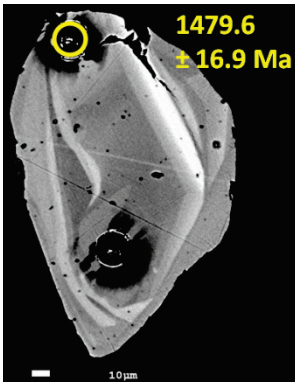

Z23

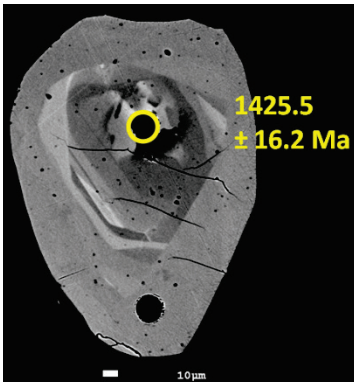

Z24

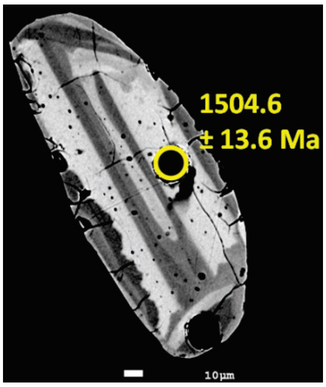

Z25

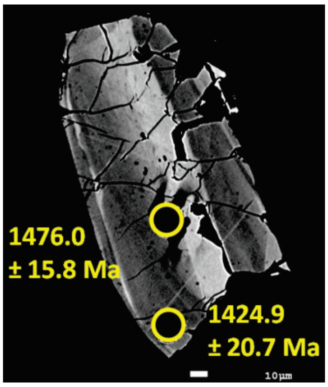

Z26

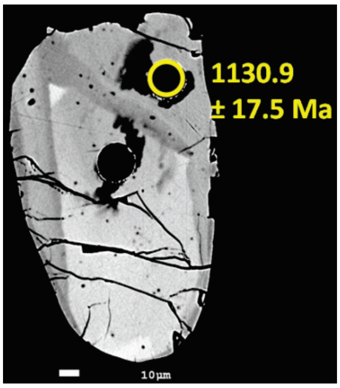

Z27

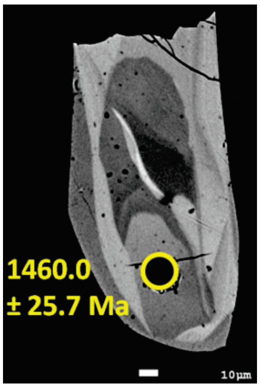

Z28

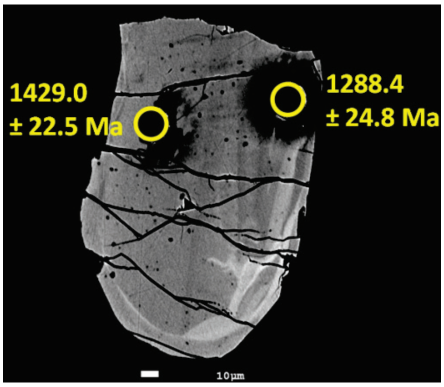

Z30